

## ABSTRACT

Title of dissertation: **CHARACTERIZATION OF MECHANICAL PROPERTIES AND DEFECTS OF SOLID-OXIDE FUEL CELL MATERIALS**

Patrick Owen Stanley  
Doctor of Philosophy, 2018

Dissertation directed by: Professor Eric D. Wachsman  
Materials Science and Engineering

Solid-oxide fuel cells (SOFC) have the potential to help the energy economy transition to a more efficient generation method. A challenge in SOFCs is that the composite ceramic cell must maintain a gas-tight seal between the anode and cathode while minimizing the thickness to improve performance. This seal must withstand heating and changes in oxygen content, which affect the physical and mechanical properties of the materials. To understand these effects, it is needed to investigate the effects of environment, microstructure, and macrostructure interplay on the cell's strength, modulus, and fracture toughness.

The mechanical properties of SOFC materials are difficult to study at operating conditions. Most research to date have investigated the material properties at ambient conditions after cycling a cell or at elevated temperatures in air. As part of this work, an enclosed three point bend apparatus has been built which can be heated to the same temperature and environment as an operating SOFC, measuring their properties *in situ*.

With this technique, among others, a variety of materials and systems have been characterized, including established materials, nickel-oxide and gadolinium doped ceria, to new materials such as a strontium iron cobalt molybdenum oxide. It has been determined how the choice of pore former effects the strength up to elevated temperatures, how fracture toughness and strength can increase with temperature due to relaxation of intrinsic stresses, the most likely time for failure of an SOFC is under reduction due to uniform growth of microstructure flaws and how cell orientation does not impact mechanical properties.

This new knowledge into the changing mechanical properties of the different materials and structures tested will allow for the design and optimization of SOFC devices to maximize reliability and performance. In addition, the apparatus built to measure in-situ properties can also be applied to other temperatures and gaseous environments for different applications. This work helps bring SOFCs from a theoretical lab-based technology to a reliable means of efficient energy generation for use by society.

# CHARACTERIZATION OF MECHANICAL PROPERTIES AND DEFECTS OF SOLID-OXIDE FUEL CELL MATERIALS

by

Patrick Owen Stanley

Dissertation submitted to the Faculty of the Graduate School of the  
University of Maryland, College Park in partial fulfillment  
of the requirements for the degree of  
Doctor of Philosophy  
2018

Advisory Committee:

Professor Eric D. Wachsman: *Advisor, Chair*

Professor Abhijit Dasgupta: *Dean's Representative*

Professor Isabel K. Lloyd

Professor Lourdes Salamanca-Riba

Professor Sreeramamurthy Ankem

© Copyright by  
Patrick Owen Stanley  
2018

## Dedication

I dedicate this to my wife, Bethany, who has encouraged and supported me throughout the process, and to my two wonderful daughters, Lucy and Madeleine. You brighten my life in ways I cannot begin to explain.

## Acknowledgments

I would like to start off by thanking my graduate advisor, Dr. Eric Wachsman, for his support during my graduate career. He allowed me the freedom to direct the details of my research and the support to help me reach my goals. He was also supportive of me when my family began to grow through marriage and children, allowing me to continue to develop my personal life while pursuing my degree.

More thanks than I can express is due to my wonderful wife, Bethany and now our daughters, Lucy and Madeleine. When Bethany and I first met, I was still deciding between gradate programs, and now, after many life changes, she continues to challenge and support me in my endeavors. Lucy and Madeleine have provided me with impetus to continue pushing through the challenges and to strike a balance between my personal and professional pursuits.

Of course I owe acknowledgement to my parents, Jim and Marilyn Stanley, who raised me to be inquisitive and persistent. Thank you for helping me to become the person that I am.

The Materials Science and Engineering Department here at UMD has been filled with marvelous and helpful people. Dr. Kathleen Hart was one of the first people I met in the department, seeming to help organize everything, always being there when needed. She has been sorely missed this past year and I hope she is making the most of her retirement. Kay Morris and Jenna Bishop in the business office help the department run smoothly, if it be answering benefits and procurement questions, or doting on my children when they visited. Then of the many professors

I have been able to interact with, I would like to especially thank Dr. Isabel Lloyd who has graciously given me her advice, help make introductions, and passed along opportunities to me when they come her way.

Somehow a small group of my friends of undergraduate have accumulated in the area. It has been a blessing to have them near by, always willing to help out when need be or to just spend time with each other. Dave and Katie Shahin are a large part of what brought me to the University and it has been a blast to go through the program with Dave. Andrew Dunkman has helped me in so many ways, from apartment hunting a thousand miles away to programming questions, for which I express my thanks. And finally, Angela Rudolph has been very supportive of me and my family getting through graduate school.

I owe a good amount of thanks to the various people in lab who helped show me the way to get started with my experiments, allowed me to bounce ideas off them, or helped with the work. Chris Pellegrinelli and Greg Hitz, you were two people who I was always comfortable with going to and asking what seemed like the most basic questions on how to do things, helping me get started in lab. Mohammad Hussain and Yi-Lin Huang shared their experience and knowledge of material science as I worked through the fundamentals. Thanks to Tom Hays for being my partner as we started mechanical testing in lab. Ian Robinson, Evans Gritton and Jon O'Neill provided much needed help with SEM, XRD, and modeling, saving me from fumbling through it myself.

I would like to acknowledge my friends and classmates at the University who formed part of my support network, sharing knowledge and encouragement. Mimi

Hiebert, Doug Henderson, Michael Van Order, Beth Tennyson, Travis Dietz, Adam Pranda, Marina Pranda, and Max Lerman, thank you for the time spent together in and out of class as we worked through our problems together laughing and having fun along the way.

Early when starting to look into mechanical properties, I was introduced to Mr. George Quinn at the National Institute of Standards and Technology. Mr. Quinn was kind enough to take much of his time to look though my preliminary work and give me feedback on testing methodology and fractography. It was a great privilege to meet the man who literally wrote the standards which I was attempting to follow and to have his guidance as I started to navigate my way though his world.

Thank you to Dr. Sean Bishop, who helped guide me as I made my ambitious goals and helped me plan out the steps needed to accomplish them.

Many facilities across campus assisted in the collection and analysis of data for this work. My thanks go to the Advanced Imaging & Microscopy Laboratory (AIMLab), the X-Ray Crystallographic Center, the Surface Analysis Center, Dr. Robert Bonenberger at the Modern Engineering Materials Instructional Laboratory,

Thank you to Redox Power Systems, the Department of Energy's National Energy Technology Laboratory and the Maryland Industrial Partnerships Program for supporting this work.

## Table of Contents

Dedication	ii
Acknowledgements	iii
List of Tables	ix
List of Figures	x
List of Abbreviations and Symbols	xiii
1 Introduction	1
1.1 Motivation for Solid-Oxide Fuel Cell Research . . . . .	1
1.2 Solid-Oxide Fuel Cell Operation . . . . .	2
1.3 Solid-Oxide Fuel Cell Materials . . . . .	7
1.4 Mechanical Properties . . . . .	9
2 Experimental Procedures	13
2.1 Sample Preparation . . . . .	13
2.1.1 $\text{SrFe}_{0.2}\text{Co}_{0.4}\text{Mo}_{0.4}\text{O}_{3-\delta}$ Powder . . . . .	13
2.1.2 Bars . . . . .	13
2.1.3 Test Coupons . . . . .	15
2.2 X-Ray Diffraction . . . . .	16
2.3 Archimedes Density Measurements . . . . .	17
2.4 Thermogravimetric Analysis . . . . .	17
2.4.1 Temperature Programed Desorption . . . . .	19
2.5 Conductivity . . . . .	19
2.6 Mechanical Testing . . . . .	20
2.6.1 Development of Mechanical Test Apparatus . . . . .	22
2.6.2 Atmospheric Treatment . . . . .	24
2.6.3 Fracture Strength . . . . .	25
2.6.4 Fracture Toughness . . . . .	25
2.7 Scanning Electron Microscopy . . . . .	26

3	High Temperature Mechanical Behavior of Porous Ceria and Ceria-Based SOFCs	27
3.1	Introduction . . . . .	27
3.2	Experimental . . . . .	29
3.2.1	Sample Preparation . . . . .	29
3.2.2	Thermogravimetric Analysis . . . . .	30
3.2.3	Development of Mechanical Test Apparatus . . . . .	31
3.2.4	Bend Testing . . . . .	34
3.2.5	Atmospheric Treatment . . . . .	35
3.3	Results . . . . .	36
3.3.1	Porosity and Pore Former Choice . . . . .	36
3.3.2	Flexural Stress Orientation . . . . .	40
3.3.3	Reduction and Strength . . . . .	43
3.4	Conclusions . . . . .	48
4	Defect chemistry and oxygen non-stoichiometry of $\text{SrFe}_{0.2}\text{Co}_{0.4}\text{Mo}_{0.4}\text{O}_{3-\delta}$	52
4.1	Introduction . . . . .	52
4.2	Experimental . . . . .	54
4.2.1	Sample Preparation . . . . .	54
4.2.2	X-ray Diffraction . . . . .	55
4.2.3	Conductivity . . . . .	55
4.2.4	Thermogravimetric Analysis (TGA) . . . . .	55
4.2.5	Temperature Programed Desorption . . . . .	57
4.3	Results and Discussion . . . . .	57
4.4	Conclusions . . . . .	70
5	Flexural strength and flaw distributions of $\text{SrFe}_{0.2}\text{Co}_{0.4}\text{Mo}_{0.4}\text{O}_3$ based ceramic-supports for solid-oxide fuel cells at operating conditions	72
5.1	Introduction . . . . .	72
5.2	Experimental . . . . .	74
5.2.1	Sample Preparation . . . . .	74
5.2.2	Conductivity . . . . .	76
5.2.3	Thermogravimetric Analysis (TGA) . . . . .	76
5.2.4	Mechanical Measurements . . . . .	76
5.2.4.1	Flexural Strength . . . . .	77
5.2.4.2	Chevron Notch Fracture Toughness . . . . .	77
5.3	Results and Discussion . . . . .	78
5.3.1	Redox Cycling Stability . . . . .	78
5.3.2	Fracture Toughness . . . . .	82
5.3.3	Half-cell Strength of Anode-Supported SOFCs at Operating Conditions . . . . .	84
5.3.4	Strength of Anode Support Layer After Redox Cycling . . . . .	86
5.4	Conclusions . . . . .	90
6	Conclusions	94

<b>A</b>	<b>Statistics</b>	95
A.1	Student's t-test . . . . .	95
A.2	Weibull Statistics . . . . .	95
<b>B</b>	<b>TGA Manual</b>	96
B.1	Theory of Operation . . . . .	96
B.2	Mass Measurement . . . . .	96
B.3	Gas Delivery . . . . .	96
B.4	pO <sub>2</sub> Measurement . . . . .	96
B.5	Controls . . . . .	96
B.6	Interfacing with other devices . . . . .	97
<b>C</b>	<b>Code</b>	98
C.1	Arduino PID Relay Furnace Controller with Serial Connectivity . . .	98
C.1.1	Hardware and other libraries . . . . .	98
C.1.2	Variables . . . . .	98
C.1.3	Serial communications . . . . .	99
<b>Bibliography</b>		105

## List of Tables

3.1	Chi-squared values for fixed $\eta$ and variable $\eta$ fits of porous GDC strength data (Figure 3.3 . . . . .	37
3.2	Summary of fit parameters for reduction of NiO-GDC/GDC half-cell coupons under 3% H <sub>2</sub> , 3% H <sub>2</sub> O, 94% N <sub>2</sub> at different temperatures. . . . .	44
4.1	Refinement results of SFCM before and after exposure to reducing and oxidizing environments . . . . .	59
4.2	Equations for defect equilibrium under reducing conditions . . . . .	68
5.1	Summary of strengths for SFCM-GDC/GDC half-cells at different environments . . . . .	86
5.2	Summary of Weibull fitting parameters (characteristic strength and Weibull modulus) for SFCM-GDC/GDC half-cells at different environments . . . . .	87
5.3	Summary of Cycled SFCM-GDC ASL Mechanical Properties . . . . .	90
5.4	Summary of Weibull Fit Parameters (characteristic strength and Weibull modulus) for Cycled SFCM-GDC ASL . . . . .	91

## List of Figures

1.1	Diagram showing flow of materials in the operation of an solid-oxide fuel cell (SOFC). . . . .	3
1.2	Diagram showing the triple phase boundary and the importance as being the site where incorporation and reactions occur. . . . .	6
1.3	Optical profilometer measurements of a a 10 cm by 10 cm Ni-GDC/GDC half-cell where the z-axis has been magnified 6X to highlight curvature. . . . .	12
2.1	Assembled Alumina 3-Point Bend Fixture . . . . .	22
2.2	Design drawing and photo of mechanical testing atmospheric chamber	23
3.1	Assembled Alumina 3-Point Bend Fixture . . . . .	32
3.2	Design drawing and photo of mechanical testing atmospheric chamber	33
3.3	Flexural strength-porosity dependence for porous GDC10 at 650 °C and 25 °C using spherical PMMA or graphite flake pore former: a) Measured strengths fitted using fixed geometric constant; b) Measured strengths fitted using different geometric constants . . . . .	37
3.4	SEM micrographs of porous GDC bars made using: a) PMMA pore former; b) graphite flake pore former . . . . .	39
3.5	Temperature dependent strength of Ni-GDC anode supports and half-cells in both air (filled data points), and reducing atmosphere (3% H <sub>2</sub> , balance Ar, hollow data points), tested in both "electrolyte-up" and "electrolyte-down" orientations resulting in the electrolyte layer experiencing tension and compression, respectively . . . . .	41
3.6	Flexural test measurements of coupons sample sets: a) Strength at 25 °C b) Strength at 650 °C c) Modulus at 25 °C d) Modulus at 650 °C	42
3.7	SEM micrographs of unreduced and reduced half-cell fracture surface: tested in air at 25 °C (top) and tested in reducing atmosphere at 650 °C (bottom), showing good adhesion between anode and electrolyte	43
3.8	Thermogravimetric analysis curves for Ni-GDC/GDC half-cells showing mass loss over time at temperatures ranging from 550 °C to 750 °C in 3% H <sub>2</sub> 3% H <sub>2</sub> O balance N <sub>2</sub> , 50 sccm flow. . . . .	45

3.9	Thermogravimetric analysis of Ni-GDC/GDC half-cell showing no mass gain after reduction and exposure to room temperature and simulated air: a) Mass loss of interrupted reduction with exposure to ambient condition; b) Temperature of sample during cycle c) Oxygen partial pressure measured at the sample during cycle . . . . .	47
3.10	Flexural properties, a) strength and b) modulus, of Ni-GDC/GDC half-cell coupons after reduction via two different methods, compared to unreduced cells. Strength and modulus show decrease upon reduction but no significant difference between methods. . . . .	49
4.1	a) Powder XRD patterns of SFCM samples taken after synthesis, reduction, and oxidation compared to pure phase SFCM diffraction pattern. b) Crystal structure of ordered double perovskite SFCM. . . . .	58
4.2	Total conductivity as $p_{O_2}$ changes under a) reducing and b) oxidizing conditions at 600 °C. . . . .	61
4.3	Temperature programmed desorption of oxygen in SFCM with mass loss from TGA (top) and oxygen desorption from MS (bottom) as it is heated to 800 °C in $N_2$ . . . . .	63
4.4	Non-stoichiometry (top) and corresponding oxygen vacancy concentration (bottom) of SFCM under oxidizing conditions (right) and reducing conditions (left) at 600 °C. . . . .	65
4.5	Non-stoichiometry of SFCM as $p_{O_2}$ changes at 400 °C, 500 °C, and 600 °C. . . . .	67
4.6	Oxygen vacancy and electronic defects in SFCM based on conductivity and TGA non-stoichiometry. . . . .	69
5.1	a) DC conductivity of SFCM and SFCM-GDC after cycling at 650 °C between 10% $H_2$ in $N_2$ and air. b) Mass loss of SFCM-GDC and NiO-GDC during reduction in 3% $H_2$ /3% $H_2O$ in $N_2$ at 650 °C. . . . .	80
5.2	Mass changes of SFCM during cycling between 21% $O_2$ and 3% $H_2$ /3% $H_2O$ in $N_2$ at 600 °C. Each exposure was 5 hours. a) Percent mass change with time as the gas is switched back and forth. b) Summary of maximum and minimum changes with each cycle. . . . .	81
5.3	a) Fracture toughness of SFCM from 20 °C to 600 °C. b) Thermal expansion of SFCM, GDC, and SFCM-GDC. . . . .	83
5.4	Flexural strengths of half-cell coupons made from SFCM-GDC anode with GDC electrolyte tested at 20 °C in air, 600 °C in air, and 600 °C in 5% $H_2$ . . . . .	85
5.5	Fitted Weibull distributions of SFCM-GDC/GDC half-cells at different environments, plotted linearly with 95% confidence intervals shaded. . . . .	87
5.6	Scanning electron microscope images of epoxy filled and polished SFCM-GDC/GDC half-cell cross sections tested at a) 20 °C in air, b) 600 °C in air and c) 600 °C in 5% $H_2$ . . . . .	88

5.7	Results of four point bend test at ambient conditions of SFCM-GDC ASL with a) strength and b) modulus for samples before any cycling and after 10 redox cycles between 10% H <sub>2</sub> and N <sub>2</sub> . . . . .	89
5.8	Fitted Weibull distributions of SFCM-GDC ASL before any cycling and after 10 redox cycles between 10% H <sub>2</sub> and N <sub>2</sub> , plotted linearly with 95% confidence intervals shaded . . . . .	91
5.9	Scanning electron microscope images of epoxy filled and polished SFCM-GDC ASL cross sections tested a) before any cycling, b) after 10 cycles between 10% H <sub>2</sub> and N <sub>2</sub> . . . . .	92

## List of Abbreviations and Symbols

GDC gadolinium doped ceria

LSM lanthanum strontium manganite

MIEC mixed ionic-electronic conductor

SOFC solid-oxide fuel cell

TPB triple phase boundary

YSZ yttria-stabilized zirconia

## Chapter 1: Introduction

### 1.1 Motivation for Solid-Oxide Fuel Cell Research

The world depends on fossil fuels for its daily energy needs. This is a fact that is going to stay with us for the foreseeable future. By 2040, it is estimated that fossil fuels will still supply 78% of total energy demand. [1] Traditionally, the annual increase in demand is met by an increase in supply of fuel. This increase is supplied by developments in mining and drilling operations, although recent advances have been found to be controversial, such as hydraulic fracturing. [2, 3] These concerns do not even account for the increased emissions caused from combustion of fossil fuels and their effect on the global environment. [4–6]

An alternative to increasing the supply and use of fossil fuels is to increase the efficiency of converting the fuel into useful work. Combustion generators convert chemical energy to thermal energy, then to mechanical energy, and finally into electrical energy. Each energy conversion step has intrinsic losses which limit efficiency. SOFCs have the ability to solve this for applications where electrical power is desired. SOFCs allow for side stepping of these losses by allowing for the direct conversion of chemical energy to electrical energy. Power generation plants have efficiencies around 30%, while a stand-alone SOFC generator can convert fuel to electricity at 45 to 65%

efficiency. [7, 8] SOFCs are able to run on a variety of fuel sources, such as hydrogen, methane or even biogas. [9, 10] This fuel flexibility and higher efficiency positions SOFCs to bridge the gap in the energy economy as it transitions from fossil fuels to renewable sources. However, many technical hurdles still remain which currently limit SOFCs' viability and must be addressed.

## 1.2 Solid-Oxide Fuel Cell Operation

The layout for a hydrogen-fueled SOFC is presented in Figure 1.1. Fuel is exposed to the anode side of the cell, while an oxygen rich gas (usually air) is exposed to the cathode side. Separating the two sides is the cell itself, with anode, electrolyte, and cathode. The electrolyte is only conductive to oxygen ions, not electrons. A perfect electrolyte would have no electronic conduction, allowing no leakage current from anode to cathode and forcing all electrons to travel via an alternative route. At the cathode, diatomic oxygen gas will disassociate into oxygen ions, each with a 2– charge from the addition of electrons from the cathode to the oxygen. The oxygen ions then travel through the electrolyte and react with the fuel at the anode, freeing the previously captured electrons. To maintain charge balance, electrons must travel in the opposite direction to the cathode. Because the electrolyte only allows oxygen ions to diffuse through it, the electrons travel through an external circuit performing useful work in the process. A limiting factor in this movement is the ability of oxygen to transport into, through, and out of the cell. As the rate of oxygen transport is increased, the ability for electrons to perform work also increases.

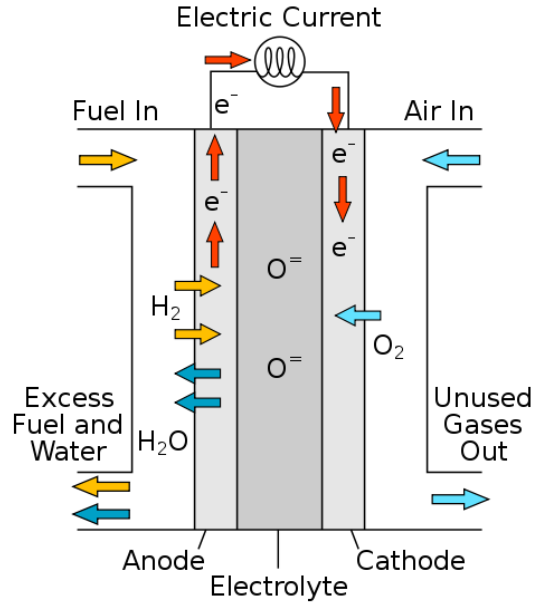
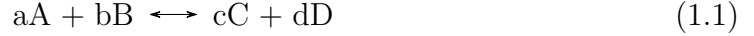


Figure 1.1: Diagram showing flow of materials in the operation of an SOFC. [11]

The driving force for the movement of oxygen ions and electrons comes from the chemical potential gradient across the cell. When the anode is exposed to fuel, it creates a low partial pressure of oxygen ( $p_{O_2}$ ) in comparison to the cathode, which is exposed to air. This gradient drives the motion of oxygen through the cell from the high  $p_{O_2}$  of the cathode to the low  $p_{O_2}$  of the anode, and generates electric current in the opposite direction to maintain a charge balance. The electrical potential at open circuit conditions (voltage with no current draw) is expressed by the Nernst equation, given in Equation 1.2 for the reaction given in Equation 1.1, where  $f_A$  is the fugacity of species A,  $E^o$  is the standard potential for the reaction, and  $n$  is the number of charges involved in the reaction,  $R$  is the ideal gas constant and  $F$  is Faraday's constant. [12] Commonly, the fugacity is replaced by the partial pressure of

the species. For the case of a hydrogen-fueled SOFC, Equation 1.2 can be simplified to Equation 1.3. [13] From these equations it can be seen that the partial pressures of the involved species have a large role to play in the open circuit voltage of the cell.



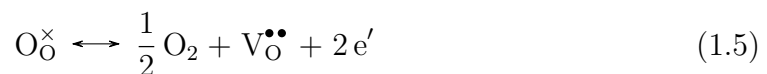
$$E = E^o - \frac{RT}{nF} \ln \left( \frac{f_C^c f_D^d}{f_A^a f_B^b} \right) \quad (1.2)$$

$$E = E^o + \frac{RT}{2F} \ln \left( \frac{p_{H_2}(p_{O_2})^{1/2}}{p_{H_2O}} \right) \quad (1.3)$$

While the electric potential is established by the partial pressure gradient, the ability for oxygen to move is controlled by the ionic conduction of oxygen ions from the cathode to the anode. In ionic conduction, oxygen ions hop from site to site via oxygen vacancies, locations where an oxygen atom is missing from the site it usually occupies in the crystal lattice. Because conduction depends on vacancies, the more vacancies that are present in the lattice, the more available sites for oxygen to move between, the greater the conductance, and the greater power output of an cell. The relationship between oxygen vacancy concentration and oxygen conductance is given by Equation 1.4, where  $\sigma_i$  is the ionic conductivity,  $[V_O^{••}]$  is the concentration of oxygen vacancies in the lattice,  $\mu_O$  is the ionic mobility of the oxygen, and  $Z_e$  is the charge of the conducting species. [14] Thus, by adding more oxygen vacancies the ionic conductivity increases. While additional oxygen vacancies are a benefit to the electrical performance of the cell, it can have detrimental effects to the mechanical properties.

$$\sigma_i = [V_O^{••}] Z_e \mu_O \quad (1.4)$$

During operation, oxygen vacancies are created by removal of lattice oxygen from the anode as it reacts with the fuel, as shown in the half-cell reaction of Equation 1.5. This reaction takes place on the surface of the anode, but for convenience it is written where oxygen has associated back into a diatomic state and the fuel subsequently react with it. This reaction of fuel with oxygen creates an environment with a very low  $p_{O_2}$  at the surface of the anode. A steady state concentration of oxygen vacancies will be reached as the cell comes into equilibrium with the environment, but this concentration will depend on the exact environmental, material, and performance conditions of the cell.



The cathode and anode materials must facilitate the incorporation of oxygen into the cell and the reaction with the fuel. They must also serve to transport the electrons into and out of the cell as oxygen changes state. As a result, the anode and cathode must possess both electrical and ionic conductivity. To achieve this, a combination of the electrolyte material is used with an electronically conductive material to create these structures. This mixture of materials creates specific sites where the cell is active, known as triple phase boundarys (TPBs) and demonstrated in Figure 1.2. The TPB is the location where gas, electronic conductor, and ionic conductor meet and oxygen can incorporate into the cell or react with the fuel. To assist gas diffusion to the TPB and to maximize the length of TPBs, pores are added, greatly increasing the available surface area of the electrodes. The more TPBs that are present, the more exchange can occur between the gas and the cell at

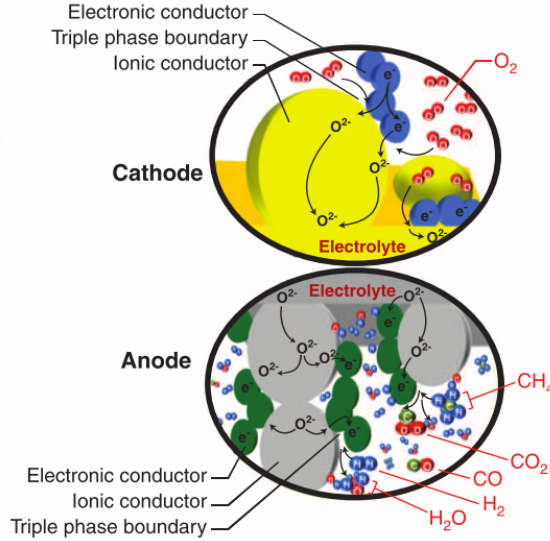


Figure 1.2: Diagram showing the triple phase boundary and the importance as being the site where incorporation and reactions occur. [7]

any given time and the current output of the cell is increased. This added porosity does not come without the disadvantage of decreasing the mechanical strength of the cell. [15, 16]

An operating SOFC would consist of a series of individual cells stacked together for combined power output. The individual cells would be sealed between current collectors and gas delivery channels and heated to operating temperature. The elevated temperature enables conduction though the electrolyte, but decreases theoretical power output and Typically, the cell operates at temperatures ranging from 600 °C to 1000 °C in order to increase the ionic conductivity and performance. It is critical that the fuel and air remain separated by the cell. If there is a leak either through the cell or around it, then the electric potential across the cell will decrease leading to failure.

### 1.3 Solid-Oxide Fuel Cell Materials

Each structure of an SOFC is fabricated from a combinations of materials designed to optimize that part's function then laminated with the other structures to create the cell. For example, a cell can be comprised of a nickel metal-gadolinium doped ceria (GDC) anode, a GDC electrolyte, and then a lanthanum strontium manganite (LSM) cathode. [17, 18] The individual parts are cast into thin flexible sheets (tapes) from bulk powders, with additives such as pore formers where appropriate, and then laminated together and co-fired to create a single cell. As a result, a completed cell has distinct layers in it where the material and properties abruptly change. This composite structure can then have inter-diffusion between layers, smoothing out the abrupt changes, but creating new structures and compositions that were not present upon lamination. [19]

Nickel has traditionally been used as an anode material in SOFCs, due to its high conductivity and catalytic properties in combination with an ionic conductor such as GDC. A challenge with nickel is that at ambient conditions it oxidizes into nickel oxide, but at operating conditions it reduces to the desired nickel metal. There is a large lattice parameter change between nickel and nickel oxide, so that as it reduces, it decreases volume by over 15%. This means that the overall porosity of the anode layer increases as the SOFC is put into service. [20, 21] This increased porosity can greatly decrease the flexural strength and modulus of the anode and of the overall cell. [22, 23] Additionally, nickel is prone to poisoning from sulfur contaminants in the fuel, so alternative anodes are of interest for use in SOFCs.

A first approach has been to develop other metal-ceramic systems to serve the function of the anode. These have included copper, cobalt, and platinum systems, but each suffer from a significant drawback such as coking, long-term performance degradation or cost. A different approach is to use an all-ceramic anode, made of a mixed ionic-electronic conductor (MIEC). Perovskite materials have easily been developed into MIECs with the use of a transition metal occupying the octahedral B-site. Examples of MIEC ceramics are  $\text{La}_{1-x}\text{Sr}_x\text{Cr}_{1-y}\text{Mn}_y\text{O}_3$ ,  $\text{Sr}_{0.94}\text{Ti}_{0.9}\text{Nb}_{0.1}\text{O}_{3-\delta}$ ,  $\text{Ba}_{0.98}\text{La}_{0.02}\text{SnO}_3$ , or  $\text{Sr}_2\text{MgMoO}_6$ . [24–30]. Due to the all-ceramic nature of these anodes, their thermal expansion coefficients better match that of the other ceramic components of the cell, reducing sintering stresses and improving redox cycling durability. Conversely, all-ceramic anodes tend to have lower conductivity and catalytic performance.

As mentioned previously, GDC is one of two common choices for electrolyte materials. The other, more traditionally used material is yttria-stabilized zirconia (YSZ). YSZ is very stable, has a ratio of ionic conductivity to total conductivity (transference number) near 1, and good conductivity at temperatures in excess of 800 °C. A transference number of 1 is desired for the electrolyte as to permit only ionic conductivity with no electronic conductivity. A lower transference number, as low as 0.9, allows a leakage current of electrons through the electrolyte, decreasing the current available through the external circuit. At lower temperatures GDC exhibits conductivity, but does suffer from a lower transference number compared to YSZ, especially under extremely reducing conditions. Other rare-earth doped cerias have been used as electrolytes, but GDC tends to outperform them under a variety of

conditions. As SOFC operating temperatures are reduced for improved efficiency, GDC is favored for the electrolyte and anode composite material.

Various cathode materials exist which assist in the incorporation of oxygen into the lattice. LSM is one of the most common. The cathode does not tend to play a structural role in the fabrication of a cell, and thus is not investigated or developed in this work.

## 1.4 Mechanical Properties

Ideally, an SOFC is as thin as possible to minimize diffusion path lengths and ionic resistances in the cell. [31] Realistically, the cell must be able to withstand the stresses of being manufactured, sealed, heating, and use. This means that a compromise must be made as to how the cell is supported and which components do the supporting. Traditionally, electrolyte supported cells were used with YSZ electrolytes where the thick dense electrolyte provides the structural support for the cell. Recently anode supported cells made from GDC have been able to provide lower resistances due to the thinner electrolyte while adequately supporting the cell with a thicker anode which fuel can diffuse further into. [32, 33] Now the anode layer with its porosity, must support the majority of the stresses the cell is subjected to.

Materials fail when the applied stresses exceed the strength. In a homogeneous material, stresses are applied uniformly throughout the material. In practice, defects will exist in the material creating points of inhomogeneities. These could be intentional with pores which are added to the material or unintended flaws such

as inclusions, contamination or grain agglomeration. These microstructural flaws are locations where stresses are concentrated and lead to the ultimate failure of the material.

Stresses are concentrated most by large, sharp featured flaws. As a result, in a uniform stress field, the largest flaw will usually cause failure. Ceramic materials will tend to fail where the sample is under tensile load and at a location near the point of maximum applied stress. Samples, even if processed together from the same raw materials, will each have a random sampling of flaws from the total batch, and a particular one which causes failure. No matter the care and attention paid to processing, some distribution of flaws will exist. The analysis of the distribution of flaws from a batch of samples is known as Weibull analysis and is explained in detail in Appendix A.2. To perform Weibull analysis a large number of samples must be tested, but as a result the overall distribution of flaws can be obtained. This allows for the observation of the flaw distribution and if it changes at different points or if another phenomenon is occurring.

Many of the materials used in SOFCs have crystal structures which promote the generation of oxygen vacancies. As oxygen vacancies are produced, the interatomic bonding of the structure changes, which can decrease the elastic modulus and fracture toughness of the crystal. [34, 35] If the strength of the atomic bonds weakens on average, due to added vacancies, it then follows that the elastic modulus and fracture toughness of the crystal would also decrease. This relationship has been shown to fit for single grains of GDC using nanoindentation, but this does not necessarily hold true for an actual cell. [36] Grain boundaries can play a large role in

the mechanical properties of a bulk sample. For this reason microstructure combined with environmental conditions can play a large role on the overall mechanical properties of a fuel cell.

The first external stress to the cell, and the one most likely to result in failure, comes from the sealing of an individual cell into a stack, creating a gas tight seal between the anode and cathode sides. While it is a compressive force that is applied, the cells are never perfectly flat, resulting in a flexural stresses as the cell is pressed flat. Figure 1.3 highlights this fact by using an optical profilometer to measure the flatness of a 10 cm by 10 cm Ni-GDC/GDC half-cell. It can be seen that the cell curves by over a millimeter, mostly at edges, where the seal would be taking place. It is for this reason that the study of the failure of SOFC materials utilizes flexural testing.

To help develop SOFCs into a viable technology which can stretch the gap in the energy economy, research is needed to improve the reliability of the cells during manufacturing and operation. This work aims to develop the understanding of fracture mechanics of real-world structures, by understanding how temperature and partial pressure of oxygen affect the strength, fracture toughness, and flaw distributions of SOFC components. This is done by analyzing the flexural properties of bulk bars and half-cell coupons at ambient conditions and at conditions similar to those found in an SOFC. Microscopy was used to look for changes in microstructure after various treatments in addition to Weibull analysis. Additionally, thermogravimetry, conductivity, and temperature programed desorption were used to understand the atomic defect structure of a new material to relate it to the mechanical properties.

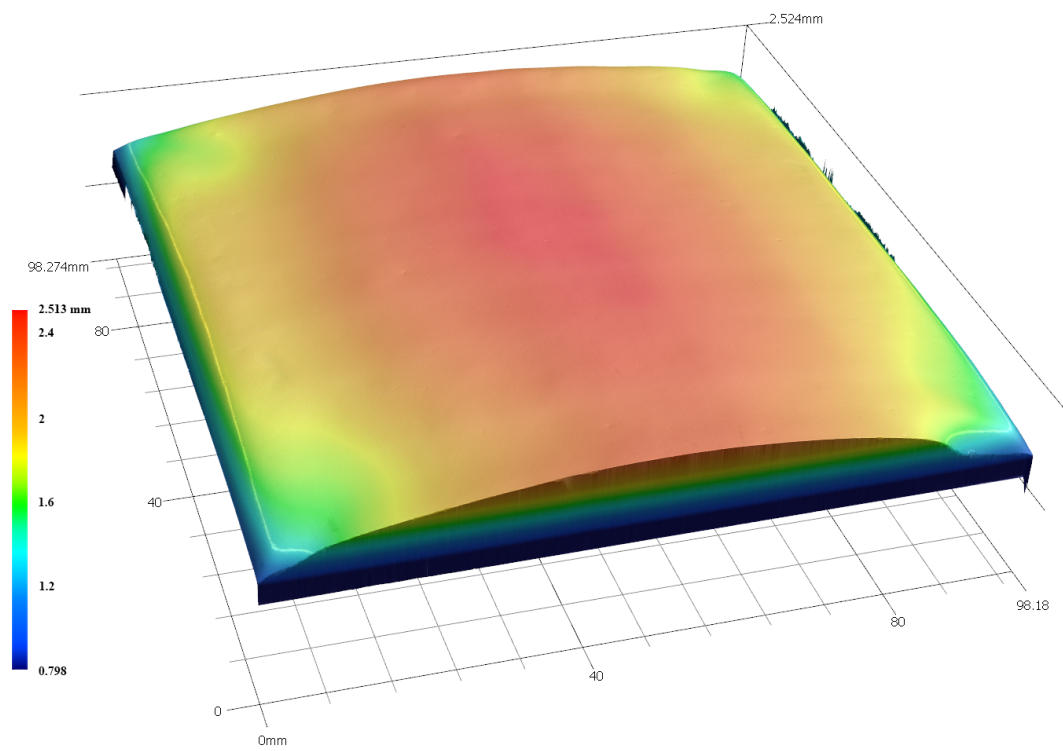


Figure 1.3: Optical profilometer measurements of a a 10 cm by 10 cm Ni-GDC/GDC half-cell where the z-axis has been magnified 6X to highlight curvature.

## Chapter 2: Experimental Procedures

### 2.1 Sample Preparation

#### 2.1.1 $\text{SrFe}_{0.2}\text{Co}_{0.4}\text{Mo}_{0.4}\text{O}_{3-\delta}$ Powder

$\text{SrFe}_{0.2}\text{Co}_{0.4}\text{Mo}_{0.4}\text{O}_{3-\delta}$  (SFCM) was created from stoichiometric amounts of strontium carbonate ( $\text{SrCO}_3$ , Sigma-Aldrich), iron oxide ( $\text{Fe}_2\text{O}_3$ , Sigma-Aldrich), cobalt oxide ( $\text{Co}_2\text{O}_3$ , Inframat Advanced Materials), and molybdenum oxide ( $\text{MoO}_3$ , Alfa-Aesar) using conventional solid-state methods. The constituents were ball milled for 24 hours in ethanol and dried using a 100 °C oven. Afterwards the powder was calcined at 1100 °C for four hours.

#### 2.1.2 Bars

GDC bars of varying porosity were fabricated using uniaxial pressing in a rectangular die. GDC10 ( $\text{Ce}_{0.9}\text{Gd}_{0.1}\text{O}_2$ ) powder was mixed with the desired volume of poly(methyl methacrylate) (PMMA) microspheres (5  $\mu\text{m}$  diameter) or graphite flake to create the green body, with 0.1wt% of polyvinyl butyral added to aid in pressing and a drop of fish oil to act as a dispersant during milling. The two different pore formers were used to create differing pore geometry. The PMMA or graphite

was removed by a 400 °C pre-sintering step, and the remaining ceramic structure was sintered at 1500 °C for 4 hours. Archimedes density measurements were used to confirm porosity percent. Samples were polished with 600 grit sandpaper on all sides before testing.

Dense SFCM bars were used to maximize the total mass and mass changes during thermogravimetric testing. Samples were made by combining SFCM powder with 0.6 wt% polyethylene glycol 600, 1.8 wt% ethylene glycol, and 0.6 wt% glycerol in isopropyl alcohol and ball milling overnight. After drying at 100 °C, the powder was ground by mortar and pestle, then pressed uniaxially into rectangular bars at 30 MPa, then isostatically pressed at 30 MPa. Bars were sintered by heating to 400 °C for one hour and then 1340 °C for four hours, using a 3 °C min<sup>-1</sup> heating and cooling rate. This produced bars with 97% theoretical density by Archimedes' technique.

To create fracture toughness test samples, SFCM powder was ball milled overnight with a mixture of 0.6 wt% polyethylene glycol 600, 1.8 wt% ethylene glycol, and 0.6 wt% glycerol in isopropyl alcohol. It was then dried at 100 °C, ground by mortar and pestle, pressed uniaxially into rectangular bars at 30 MPa, then isostatically pressed at 30 MPa. Sintering followed by heating to 1340 °C for four hours at 3 °C/min with a one hour hold at 400 °C to allow the binders to burn out. This process achieved dense samples at 97% average theoretical density with no apparent flaws in the bars. Bars were then cut and sanded to final dimensions of 3 mm x 4 mm x 25 mm. The chevron notch was cut using the jig described by Jenkins, Chang and Okura following the ASTM procedure. [37, 38]

### 2.1.3 Test Coupons

The ASL and half-cell coupons used in the flexural testing were made using tape casting. NiO and GDC powders in a 6:4 weight ratio were mixed with ethanol, toluene, and fish oil. The mixture was ball milled on a rotary mill for 24 hours. Polyvinyl butyral and benzyl butyl phthalate were added, followed by another 24 hours milling. The resulting slurry was degassed and tape cast using a 700 micron blade height. The tapes were left to dry overnight before being cut into 12 cm by 12 cm squares. Three squares were stacked and hot pressed at 49 °C and 2 tons for 30 minutes. Following this lamination, the tape was cut into rectangular coupons measuring 25mm by 10mm. The coupons were fired at 1400 °C for 4 hours. Final bar dimensions were 8.16 by 24.15 by 2.98 mm on average. For half-cell coupons GDC electrolyte slurry was prepared and tape cast with a 40 micron blade height. After the lamination of the three ASL layers, a single layer of electrolyte tape was laminated to the ASL using the same pressure for 2 hours. The sintering procedure for half-cell coupons was identical to the ASL coupons. Samples were polished with 600 grit sandpaper on edges before testing.

Tape casting was used to create test coupons of porous SFCM-GDC ASL and SFCM-GDC/GDC half-cells. Using ethanol as a solvent, SFCM-GDC was ball milled with polyvinyl butyral, benzyl butyl phthalate, 12 µm poly(methyl methacrylate) (16 wt% with respect to SFCM-GDC), and Menhaden fish oil. The tape was cast to a thickness of 110 µm on Mylar then laminated using a hot press to a final thickness of 660 µm. Dense GDC was casted to 30 µm and laminated to the top of

the SFCM-GDC to create half-cells. Individual coupons were cut from the green tape, sintered at 1200 °C for four hours, with holds at low temperatures to burn out organic binder and pore former. The final thicknesses were measured to be 400  $\mu\text{m}$  for the SFCM-GDC ASL and  $\sim$ 20  $\mu\text{m}$  thick GDC electrolyte. Test coupons had their edges sanded to remove defects left from cutting, following ASTM standards. [39] Top and bottom surfaces were not sanded to preserve possible defects left from tape casting procedure, which would be representative of industrially manufactured SOFCs.

## 2.2 X-Ray Diffraction

X-ray diffraction (XRD) was used confirm phase purity of the SFCM after synthesis and during the testing process. A Bruker D8 Advance with LynxEye was used with a Cu K $\alpha$  source. A step size of 0.02° was used with a dwell of 0.8 s was used. Rietveld refinement was performed on samples as synthesized, after oxidation in pure O<sub>2</sub> and after reduction in pure H<sub>2</sub> at 600 °C for both. GSAS-II was used to perform the refinement calculations and VESTA was used to visualize the unit cell. [40, 41]

### 2.3 Archimedes Density Measurements

### 2.4 Thermogravimetric Analysis

Mass of samples during oxidation and reduction cycling was measured using a Cahn D200 microbalance. The samples were placed in a crucible suspended from a platinum wire attached to the microbalance and enclosed by an alumina tube inside a furnace. Heating control was achieved with a PID loop and temperature measurement done by a K-type thermocouple placed immediately below the sample inside the alumina tube. Gas flow was controlled at a constant 50 sccm by mass flow controllers. 21% O<sub>2</sub> in dry N<sub>2</sub> was used for the oxidizing condition while 3% H<sub>2</sub> in N<sub>2</sub> humidified with 3% H<sub>2</sub>O was used for the reducing conditions.

To understand the degree of reduction in test coupons, thermogravimetric analysis (TGA) was used to measure the mass loss as a function of time, temperature, and gas environment. A Cahn D200 microbalance was used to measure the weight changes as the sample was heated in a furnace with controlled atmosphere. A small section of test coupon was placed in a crucible suspended from the balance and heated to 650 °C at 10 °C min<sup>-1</sup>, the environment was switched from 50 sccm of 21% O<sub>2</sub> in N<sub>2</sub> to 50 sccm of 3% H<sub>2</sub>, 3% H<sub>2</sub>O in N<sub>2</sub>. Mass, temperature, and p<sub>O<sub>2</sub></sub> measurements were taken at 30 second intervals. p<sub>O<sub>2</sub></sub> measurements were taken using a calibrated YSZ sensor placed immediately before the sample. Samples were cooled at 10 °C min<sup>-1</sup> in the desired atmosphere.

Changes in mass of SFCM were measured by a Cahn D200 microbalance with

the sample suspended down a quartz tube into a furnace. The furnace used to heat the sample and quartz tube was controlled by a PID controller with a K-type thermocouple placed immediately below the sample inside the quartz tube. Gas flow was controlled at consistent 50 sccm by mass flow controllers, which mixed dry nitrogen, oxygen, hydrogen, and humidified nitrogen to obtain the  $p_{O_2}$  desired. Measurements of the  $p_{O_2}$  were taken by a calibrated YSZ oxygen sensor at 800 °C located before the sample. Again, intermediate  $p_{O_2}$  ranges were not able to be tested due to SFCM's incompatibility with the species required to create that environment.

Further details of the operation of the TGA and its various components are given in Appendix [B](#).

To prepare the sample, it was pre-weighed, wrapped in platinum wire and suspended from the balance, placed in the furnace with simulated air (21% O<sub>2</sub>, 79% N<sub>2</sub>) flowing. Once the mass had stabilized, the furnace was heated to 800 °C to allow for any organic contamination to burn off. After the mass stabilized at this elevated temperature the sample was introduced to various environments. The mass of the sample would be noted only after steady state had been reached for a condition. After testing a sample, a bar of alumina was cut to the same dimensions as the sample and the process was repeated to obtain a blank which could be subtracted from the measurements to remove buoyancy effects.

Oxygen non-stoichiometry was calculated using Equation [4.1](#), where  $\Delta\delta$  is the change in oxygen stoichiometry,  $MW_{SFCM}$  is the molecular weight of SFCM (208.74 g mol<sup>-1</sup>),  $MW_O$  is the molecular weight of oxygen (16.0 g mol<sup>-1</sup>),  $w_{sample}$  is the weight of the sample, and  $\Delta w$  is the weight change as recorded by the TGA. The

oxygen vacancy concentration ( $[V_O^{\bullet\bullet}]$ ) is calculated using Equation 4.2, where  $\rho$  is the density of SFCM and  $N_A$  is Avogadro's number. To calculate the oxygen vacancy concentration, the non-stoichiometry of SFCM at a point needs to be established. For this work, based on the plateau present in the data at oxidizing conditions, it is assumed that in a pure oxygen environment ( $\log(p_{O_2}) = 0$ ) all oxygen vacancies are filled with no oxygen interstitial or surface species, thus  $\delta = 0$ .

$$\Delta\delta = \frac{MW_{SFCM}}{MW_O w_{sample}} - \Delta w \quad (2.1)$$

$$[V_O^{\bullet\bullet}] = \frac{\delta\rho N_A}{MW_{SFCM}} \quad (2.2)$$

#### 2.4.1 Temperature Programmed Desorption

The effluent from the TGA was used as the inlet to a mass spectrometer (MS) to perform temperature programmed desorption. The sample was prepared as before and heat treated to remove any carbon contaminants but was allowed to cool under simulated air. It was then heated to  $800^\circ\text{C}$  at  $5^\circ\text{C min}^{-1}$  under a 50 sccm flow of nitrogen as the MS measured the  $32\text{ m/z}$  signal which corresponded to  $O_2$  desorption. Additional  $m/z$  signals were monitored to observed for other species.

#### 2.5 Conductivity

Electric conductivity across  $p_{O_2}$  was measured using the four-wire technique and a Stanford SR 830 lock-in amplifier. A bar shape sample was used with dimensions of  $6.46\text{ mm} \times 3.3\text{ mm} \times 1.3\text{ mm}$ . Gold paste was used as a current collector, and the current range was between 0.005 to 0.05 A. A yttria-stabilized zirconia (YSZ)

oxygen sensor operating at 800 °C was used to monitor the changes in oxygen partial pressures. Intermediate  $p_{O_2}$  ranges were not tested due to an incompatibility between SFCM and the CO and  $CO_2$  required to obtain those  $p_{O_2}$ .

Conductivity during redox cycling was measured using rectangular bars of SFCM and SFCM-GDC (2:1) composite. The samples were connected to a Keithley 2400 source meter by silver paste and wire. Using an in-house built reactor, the sample could be heated and the gas environment could be controlled. An initial measurement was taken after heating and 50 hours of exposure to 10%  $H_2$  in  $N_2$ , then the sample exposed cycled between air and reducing conditions over a period of 14 days.

## 2.6 Mechanical Testing

Measurements of mechanical properties were collected using a Tinius Olsen 10ST Universal Testing Machine equipped with a 250 N load cell. Experiments where any samples would be tested at elevated temperatures or under reducing environments were conducted using a custom built three point flexural test fixture placed inside a gas-tight chamber and furnace. Otherwise, a fully-articulating four point flexural test fixture was used. Samples tested at ambient conditions were placed on the appropriate testing fixture and loaded until failure. For samples tested at elevated temperatures the sample was heated in the test chamber at  $10\text{ }^{\circ}\text{C min}^{-1}$ , allowed to equilibrate for 20 minutes, then tested. Samples to be reduced were placed in the chamber, heated and exposed to reducing gas for 18 hours before being tested.

All tests conducted in the UTM (Tinius Olsen 10ST with 250 N load cell) were done at a rate of  $0.2 \text{ mm min}^{-1}$  with a 20 mm lower span. After measuring the force at fracture, stress was calculated using Equation 5.3 for 3-point flexural of rectangular samples, where  $\sigma_f$  is the stress at failure, F is the load at failure, L is the span of the fixture, b is the width of the sample and d is the thickness of the sample. At room temperature, the coupons or bars were loaded into the fixture and tested in batches of 5 per condition. Occasionally samples would break or be damaged before testing, reducing the sample set. For sample sets at elevated temperatures in ambient atmosphere, the samples were loaded into the front of the chamber, acting as a staging area, prior to heating the on fixture in the center. Upon transferring the next coupon from the staging area to the fixture, a 20 minute waiting period was used to ensure that the coupon had reached thermal equilibrium prior to testing.

$$\sigma_f = \frac{3FL}{2bd^2} \quad (2.3)$$

Following the completion of the set, all coupon pieces were cooled at a rate of  $10^\circ\text{C}/\text{min}$ . For testing in reducing atmosphere, each coupon was reduced and tested individually. Half-cell coupons were tested in two orientations, "electrolyte-up" and "electrolyte-down." These orientations cause the dense electrolyte layer to experience compressive or tensile stress. The "electrolyte-up" orientation subjects the electrolyte to compressive stress and vice-versa.

Following the destructive tests, SEM analyses of the fracture surfaces were performed. The purpose of this was to observe the trans-granular, inter-granular, or mixed nature of crack propagation, and to find any anomalous features on the



Figure 2.1: Assembled Alumina 3-Point Bend Fixture

fracture surface, as well as to observe pore geometry.

### 2.6.1 Development of Mechanical Test Apparatus

To develop a testing apparatus capable of simulating the various conditions experienced by operating SOFCs, appropriate materials were chosen based on thermal and chemical stability criteria. Alumina was chosen to build the bend fixture due to its chemical stability and high hardness. The sample rests crossways on two stationary 6.35 mm diameter rods which are placed in troughs separated by 20 mm. The upper half of the fixture consists of a 6.35 mm rod used to apply stress to the sample from the UTM crosshead. Both pieces are attached using silica-based cement to 300 mm rods attached at the anchor points of the UTM. Assembly and alignment is assisted with the use of a 3D printed jig to ensure repeatability. The complete alumina, 3-point bend fixture is seen in Figure 3.1 with the two bottom rollers, a sample, and the top roller making contact, applying flexural stresses to the sample.

To create the atmosphere control system, a combination of standard and custom vacuum system parts were used to enclose the bend fixture. For the main body of the chamber, a 3-inch inner diameter, stainless steel tee was made with QF80 and QF50 flanges. Welded NPT ports on top and bottom allow for gas inlet and

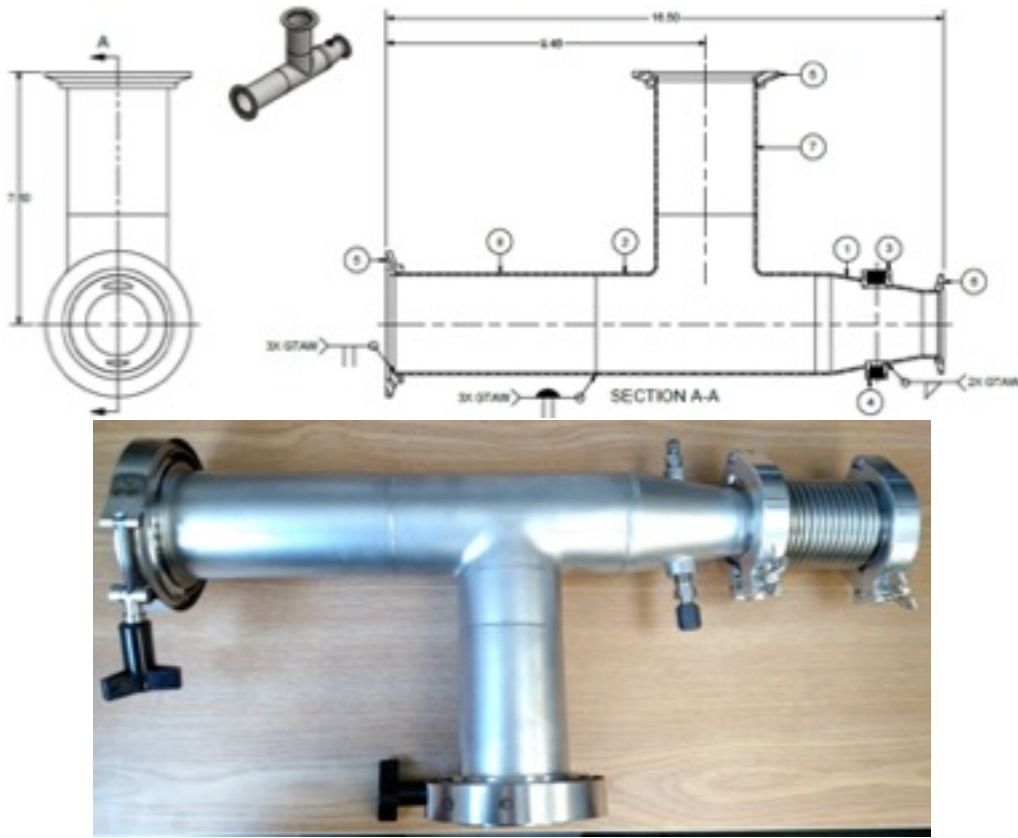


Figure 2.2: Design drawing and photo of mechanical testing atmospheric chamber

outlet and the introduction of a thermocouple through a Swagelok Ultra-Torr fitting. Figure 3.2 shows the engineering drawings and photo of the custom pieces from A&N Corp. Flexible bellows allow for the motion of the cross-bar to be translated into the fixture, requiring the subtraction of the spring force to be removed during analysis. The alumina fixture was then inserted through each end and the chamber incorporated into the furnace with QF50 to 1/2 inch tube adapters that fit over the alumina rods.

To heat the fixture and chamber, a 1 ft. cube was assembled from steel plates with cutouts on top, bottom and front. Steel wire mesh was used to create

a framework inside to hold nickel-chromium alloy heating elements. Silica-based wool insulation was packed between the center cavity and the case walls. A K-type thermocouple was inserted into the chamber and used with an external PID controller to cycle the heating elements. The furnace was placed on a supporting scaffold to hold it in position during tests. The test fixture, atmosphere chamber, and furnace were affixed together as one unit and inserted into the UTM. The design was compared and qualified to a regular steel 3-point bend apparatus to ensure accurate results at room temperature.

### 2.6.2 Atmospheric Treatment

To test individual coupons under reducing environments, samples were loaded into the test chamber at 400 °C, after previous pre-heating in the staging area. After 20 minutes, the temperature would be increased to the desired set-point of 650 °C at a ramp rate of  $10\text{ }^{\circ}\text{C min}^{-1}$  and the gas would be switched first to N<sub>2</sub> to flush the chamber, then to humidified argon containing 3% H<sub>2</sub>. It would then be allowed to sit for 18 hours before testing to allow reduction. After testing, the chamber would be flushed again with N<sub>2</sub> and cooled to 400 °C before opening to change samples and repeat the process.

If samples had been previously reduced as a batch by exposure to hydrogen in a tube furnace and cooled under hydrogen, the atmospheric treatment was shortened, as supported by TGA results. Pre-reduced samples were loaded into the chamber at or below 400 °C, the chamber flushed N<sub>2</sub>, then with H<sub>2</sub> in Ar. After this the chamber

would be heated to 650 °C, the sample tested after a 30 minute period, and cooled back down to 400 °C. At this point, the chamber would be flushed with N<sub>2</sub>. While the chamber maintained a positive pressure of N<sub>2</sub>, it could be opened, a new sample loaded, closed, and allowed to flush. This procedure allows for the batch reduction of many test coupons and replaced the 18 hour reduction time with a shorter 30 minute period.

### 2.6.3 Fracture Strength

A loading rate of 0.2 mm/min was used for all strength measurements. Strength was calculated from the maximum force measured before failure according to Equation 5.2 or 5.3 depending on if the four point or three point fixture is used respectively, where  $\sigma$  is the strength,  $P$  is the maximum force,  $L$  is the span width of the test fixture,  $b$  is the width of the sample and  $d$  is the thickness of the sample. Equation 5.2 is for a fixture where the top span is 1/2 the width of the bottom span. [39]

$$\sigma = \frac{3PL}{4bd^2} \quad (2.4)$$

### 2.6.4 Fracture Toughness

The fracture toughness of chevron notched samples were measured using a loading rate of 0.001 mm/min. Fracture toughness was calculated from the maximum force using Equation 5.4 or 5.5 for four point or three point fixtures. [38, 42]  $Y_{min}^*$  is the shape factor as calculated by Equation 5.6,  $S_o$  and  $S_i$  are the outer and inner spans,  $B$  is the width of the sample,  $W$  is the height of the sample,  $a_0$  is the distance

from the tip of the chevron notch to the bottom of the sample, and  $a_1$  is the average distance from the side of the chevron notch to the bottom of the sample. Each sample was measured after failure, but in this study the approximate values were  $S_o = 40mm$ ,  $S_i = 20mm$ ,  $B = 3.0mm$ ,  $W = 4.0mm$ ,  $a_0 = 0.80mm$ ,  $a_1 = 3.8mm$ . Fracture toughness was measured only under air at room temperature and up to 600 °C. Under reduction the fracture toughness bars would spontaneously fracture, preventing measurements under that condition.

$$K_{Ivb} = Y_{min}^* \left[ \frac{P[S_o - S_i]}{BW^{3/2}} \right] 10^{-6} \quad (2.5)$$

$$K_{Ivb} = Y_{min}^* \left[ \frac{P}{BW^{1/2}} \right] 10^{-6} \quad (2.6)$$

$$Y_{min}^* = \frac{0.38742 - 3.0919(a_0/W) + 4.2017(a_1/W) - 2.3127(a_1/W)^2 + 0.6379(a_1/W)^3}{1.0000 - 2.9686(a_0/W) + 3.5056(a_0/W)^2 - 2.1374(a_0/W)^3 + 0.0130(a_1/W)} \quad (2.7)$$

## 2.7 Scanning Electron Microscopy

# Chapter 3: High Temperature Mechanical Behavior of Porous Ceria and Ceria-Based SOFCs

## 3.1 Introduction

For planar SOFCs, a standard stack design consists of a number of square cells separated by metal interconnects. [43] These interconnects act as current collectors, gas channels, and separators to prevent fuel and air from mixing. Sealing of these stacks is accomplished by compressing the layered structure which includes sealing material. As more compressive force is applied to the stack, the quality of the seals improves. However, any cell which is not perfectly flat will experience flexural stress as a result and this can lead to cells fracturing. Due to the brittle nature of the ceramic materials that constitute SOFCs, a very thorough understanding of the mechanical limits of these devices is critical to their successful deployment.

The vulnerability of SOFCs to mechanical failure is a well-known issue. However, much of the research into this phenomenon has focused on yttrium stabilized zirconia (YSZ) based devices. [21,44,45] This material has been the standard for the field and has desirable mechanical properties but requires high temperatures to function well. As efforts are made to lower SOFC operating temperatures, a shift to ceria-based

electrolytes has occurred. Less attention has been given to the mechanical behavior of doped ceria materials across SOFC operating conditions.

Much of the study of fracture in ceramic materials has been done on technical ceramics for medical applications and for coating metal components. [46–53] These materials are optimized for fracture toughness and durability and very rarely experience temperatures above a few hundred degrees Celsius. The fracture surface analysis and correlations between microstructure and strength described for these materials are a valuable starting point for investigating fuel cell materials. However, there is a lack of extensive investigation into the properties of IT-SOFC materials at their expected operating temperatures and environments.

Efforts have been made to comprehensively examine the mechanical properties of SOFC materials and the effect of non-standard conditions on those properties. Nakajo et al. conducted a wide ranging study of materials used in anode supported SOFCs which included some attention to temperature and atmosphere effects. [45] While providing a solid base of material knowledge, this work did not fully cover materials beyond YSZ and there remains a need for further testing, especially for doped ceria. Flexural strength and Young's modulus measurements for gadolinium doped ceria (GDC) have been carried out in ambient conditions by Yasuda et al. [54] They characterized the effects of sintering temperature on density and the resulting mechanical properties. Further testing of this material system at elevated temperatures and anode gas reducing environments must be done to fully understand the mechanical behavior of GDC.

This article presents the results of a broad range of flexural tests involving the

materials used in ceria-based anode supported SOFCs along with the assembled half-cells. Using a purpose-built temperature controlled environmental chamber installed in a universal testing machine (UTM), porous doped ceria bars, anode support layers (ASL) composed of nickel and doped ceria cermet, and half-cells composed of an ASL and a doped ceria electrolyte were tested. The various test conditions used included expected operating temperatures (450 °C–650 °C), and both reducing and oxygenated atmospheres. These variations in test conditions are important because these cells must maintain their integrity from when they are first placed in a sealed stack to when they reach operating conditions. In particular, this study was intended to determine at what point in their life SOFCs are most vulnerable to mechanical failure and the mechanisms involved. Additionally, the effect of the anode-electrolyte interface on flexural strength was explored.

## 3.2 Experimental

### 3.2.1 Sample Preparation

GDC bars of varying porosity were fabricated using uniaxial pressing in a rectangular die. GDC10 ( $\text{Ce}_{0.9}\text{Gd}_{0.1}\text{O}_2$ ) powder was mixed with the desired volume of poly(methyl methacrylate) (PMMA) microspheres (5 µm diameter) or graphite flake to create the green body, with 0.1wt% of polyvinyl butyral added to aid in pressing and a drop of fish oil to act as a dispersant during milling. The two different pore formers were used to create differing pore geometry. The PMMA or graphite was removed by a 400 °C pre-sintering step, and the remaining ceramic structure

was sintered at 1500 °C for 4 hours. Archimedes density measurements were used to confirm porosity percent. Samples were polished with 600 grit sandpaper on all sides before testing.

The ASL and half-cell coupons used in the flexural testing were made using tape casting. NiO and GDC powders in a 6:4 weight ratio were mixed with ethanol, toluene, and fish oil. The mixture was ball milled on a rotary mill for 24 hours. Polyvinyl butyral and benzyl butyl phthalate were added, followed by another 24 hours milling. The resulting slurry was degassed and tape cast using a 700 micron blade height. The tapes were left to dry overnight before being cut into 12 cm by 12 cm squares. Three squares were stacked and hot pressed at 49 °C and 2 tons for 30 minutes. Following this lamination, the tape was cut into rectangular coupons measuring 25mm by 10mm. The coupons were fired at 1400 °C for 4 hours. Final bar dimensions were 8.16 by 24.15 by 2.98 mm on average. For half-cell coupons GDC electrolyte slurry was prepared and tape cast with a 40 micron blade height. After the lamination of the three ASL layers, a single layer of electrolyte tape was laminated to the ASL using the same pressure for 2 hours. The sintering procedure for half-cell coupons was identical to the ASL coupons. Samples were polished with 600 grit sandpaper on edges before testing.

### 3.2.2 Thermogravimetric Analysis

To understand the degree of reduction in test coupons, thermogravimetric analysis (TGA) was used to measure the mass loss as a function of time, temperature,

and gas environment. A Cahn D200 microbalance was used to measure the weight changes as the sample was heated in a furnace with controlled atmosphere. A small section of test coupon was placed in a crucible suspended from the balance and heated to  $650\text{ }^{\circ}\text{C}$  at  $10\text{ }^{\circ}\text{C min}^{-1}$ , the environment was switched from 50 sccm of 21% O<sub>2</sub> in N<sub>2</sub> to 50 sccm of 3% H<sub>2</sub>, 3% H<sub>2</sub>O in N<sub>2</sub>. Mass, temperature, and p<sub>O<sub>2</sub></sub> measurements were taken at 30 second intervals. p<sub>O<sub>2</sub></sub> measurements were taken using a calibrated YSZ sensor placed immediately before the sample. Samples were cooled at  $10\text{ }^{\circ}\text{C min}^{-1}$  in the desired atmosphere.

### 3.2.3 Development of Mechanical Test Apparatus

To develop a testing apparatus capable of simulating the various conditions experienced by operating SOFCs, appropriate materials were chosen based on thermal and chemical stability criteria. Alumina was chosen to build the bend fixture due to its chemical stability and high hardness. The sample rests crossways on two stationary 6.35 mm diameter rods which are placed in troughs separated by 20 mm. The upper half of the fixture consists of a 6.35 mm rod used to apply stress to the sample from the UTM crosshead. Both pieces are attached using silica-based cement to 300 mm rods attached at the anchor points of the UTM. Assembly and alignment is assisted with the use of a 3D printed jig to ensure repeatability. The complete alumina, 3-point bend fixture is seen in Figure 3.1 with the two bottom rollers, a sample, and the top roller making contact, applying flexural stresses to the sample.

To create the atmosphere control system, a combination of standard and custom



Figure 3.1: Assembled Alumina 3-Point Bend Fixture

vacuum system parts were used to enclose the bend fixture. For the main body of the chamber, a 3-inch inner diameter, stainless steel tee was made with QF80 and QF50 flanges. Welded NPT ports on top and bottom allow for gas inlet and outlet and the introduction of a thermocouple through a Swagelok Ultra-Torr fitting. Figure 3.2 shows the engineering drawings and photo of the custom pieces from A&N Corp. Flexible bellows allow for the motion of the cross-bar to be translated into the fixture, requiring the subtraction of the spring force to be removed during analysis. The alumina fixture was then inserted through each end and the chamber incorporated into the furnace with QF50 to 1/2 inch tube adapters that fit over the alumina rods.

To heat the fixture and chamber, a 1 ft. cube was assembled from steel plates with cutouts on top, bottom and front. Steel wire mesh was used to create a framework inside to hold nickel-chromium alloy heating elements. Silica-based wool insulation was packed between the center cavity and the case walls. A K-type thermocouple was inserted into the chamber and used with an external PID controller to cycle the heating elements. The furnace was placed on a supporting scaffold to hold it in position during tests. The test fixture, atmosphere chamber, and furnace were affixed together as one unit and inserted into the UTM. The design was

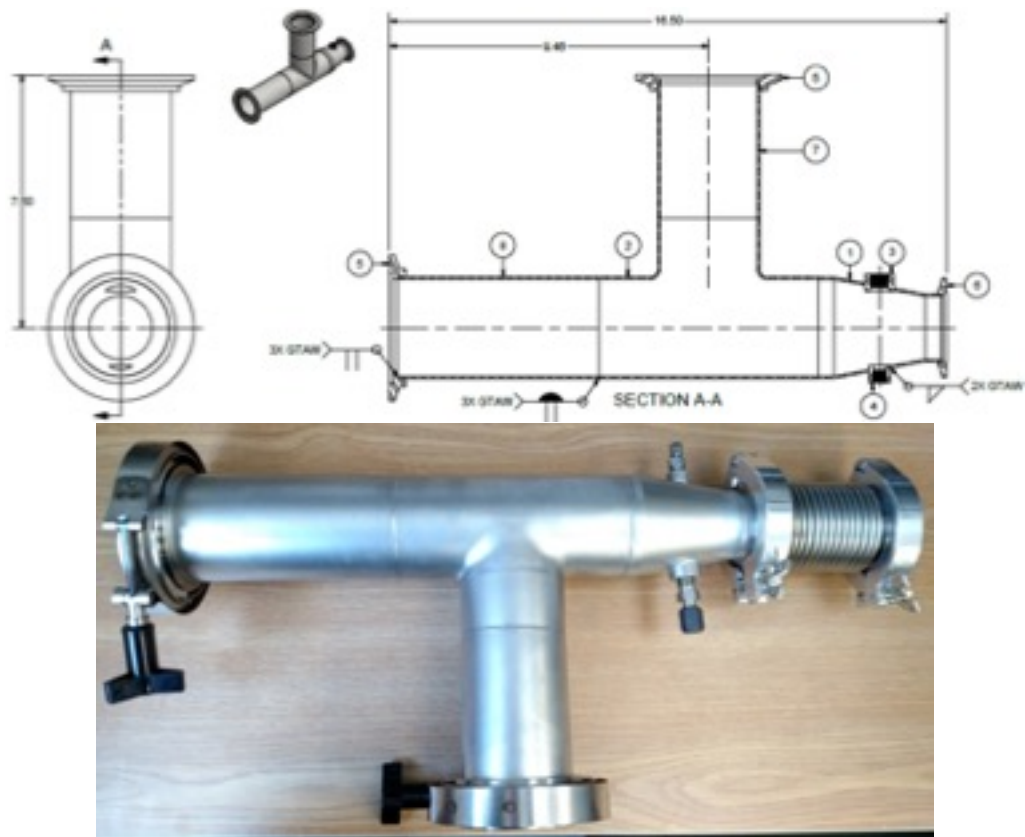


Figure 3.2: Design drawing and photo of mechanical testing atmospheric chamber

compared and qualified to a regular steel 3-point bend apparatus to ensure accurate results at room temperature.

### 3.2.4 Bend Testing

All tests conducted in the UTM (Tinius Olsen 10ST with 250 N load cell) were done at a rate of  $0.2 \text{ mm min}^{-1}$  with a 20 mm lower span. After measuring the force at fracture, stress was calculated using Equation 5.3 for 3-point flexural of rectangular samples, where  $\sigma_f$  is the stress at failure, F is the load at failure, L is the span of the fixture, b is the width of the sample and d is the thickness of the sample. At room temperature, the coupons or bars were loaded into the fixture and tested in batches of 5 per condition. Occasionally samples would break or be damaged before testing, reducing the sample set. For sample sets at elevated temperatures in ambient atmosphere, the samples were loaded into the front of the chamber, acting as a staging area, prior to heating the on fixture in the center. Upon transferring the next coupon from the staging area to the fixture, a 20 minute waiting period was used to ensure that the coupon had reached thermal equilibrium prior to testing.

$$\sigma_f = \frac{3FL}{2bd^2} \quad (3.1)$$

Following the completion of the set, all coupon pieces were cooled at a rate of  $10^\circ\text{C}/\text{min}$ . For testing in reducing atmosphere, each coupon was reduced and tested individually. Half-cell coupons were tested in two orientations, "electrolyte-up" and "electrolyte-down." These orientations cause the dense electrolyte layer to experience compressive or tensile stress. The "electrolyte-up" orientation subjects the electrolyte

to compressive stress and vice-versa.

Following the destructive tests, SEM analyses of the fracture surfaces were performed. The purpose of this was to observe the trans-granular, inter-granular, or mixed nature of crack propagation, and to find any anomalous features on the fracture surface, as well as to observe pore geometry.

### 3.2.5 Atmospheric Treatment

To test individual coupons under reducing environments, samples were loaded into the test chamber at 400 °C, after previous pre-heating in the staging area. After 20 minutes, the temperature would be increased to the desired set-point of 650 °C at a ramp rate of 10 °C min<sup>-1</sup> and the gas would be switched first to N<sub>2</sub> to flush the chamber, then to humidified argon containing 3% H<sub>2</sub>. It would then be allowed to sit for 18 hours before testing to allow reduction. After testing, the chamber would be flushed again with N<sub>2</sub> and cooled to 400 °C before opening to change samples and repeat the process.

If samples had been previously reduced as a batch by exposure to hydrogen in a tube furnace and cooled under hydrogen, the atmospheric treatment was shortened, as supported by TGA results. Pre-reduced samples were loaded into the chamber at or below 400 °C, the chamber flushed N<sub>2</sub>, then with H<sub>2</sub> in Ar. After this the chamber would be heated to 650 °C, the sample tested after a 30 minute period, and cooled back down to 400 °C. At this point, the chamber would be flushed with N<sub>2</sub>. While the chamber maintained a positive pressure of N<sub>2</sub>, it could be opened, a new sample

loaded, closed, and allowed to flush. This procedure allows for the batch reduction of many test coupons and replaced the 18 hour reduction time with a shorter 30 minute period.

### 3.3 Results

#### 3.3.1 Porosity and Pore Former Choice

As expected, GDC bars with greater porosity displayed lower flexural strength values as compared to less porous samples. The relationship between porosity and strength followed an exponential trend. This behavior is well established for porous ceramics and is described by Equation 3.2, where  $\sigma_f$  is the flexural strength with porosity,  $\sigma_o$  is the flexural strength without porosity,  $\eta$  is a geometric constant dependent on the system, and  $P$  is the volume percent porosity of the sample. [55]

$$\sigma_f = \sigma_o e^{-\eta P} \quad (3.2)$$

The data was fit using this equation and both a fixed geometric constant,  $\eta$ , of 0.047 (Figure 3.3a) and a variable geometric constant (Figure 3.3b).

Chi-squared values, indicating the divergence of the fit from the measured data for each sample set, were calculated for the two fitting methods and are displayed in Table 3.1.

The deviance from the fit curve for the fixed  $\eta$  method is quite large relative to the variable  $\eta$  fit for both sample sets tested at 650 °C. Both fitting methods are fairly poor in the case of the room temperature graphite set. The poor fitting

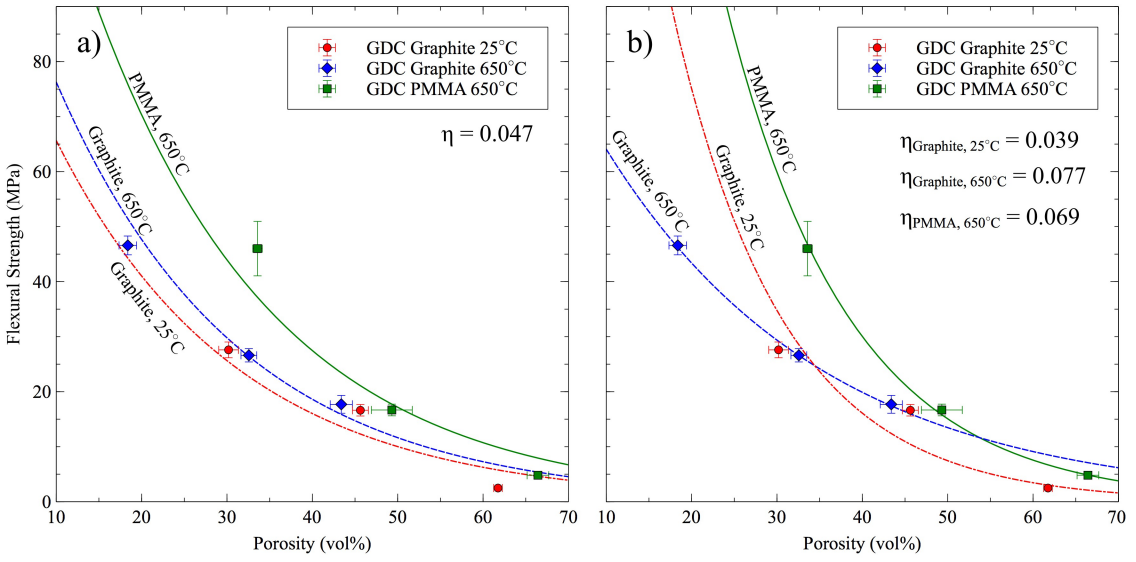


Figure 3.3: Flexural strength-porosity dependence for porous GDC10 at 650 °C and 25 °C using spherical PMMA or graphite flake pore former: a) Measured strengths fitted using fixed geometric constant; b) Measured strengths fitted using different geometric constants

Table 3.1: Chi-squared values for fixed  $\eta$  and variable  $\eta$  fits of porous GDC strength data (Figure 3.3)

Sample Set	$\chi^2$	$\chi^2$
	(Fixed $\eta$ )	(Variable $\eta$ )
GDC PMMA 650 °C	3.406	0.062
GDC Graphite 650 °C	0.668	0.008
GDC Graphite 25 °C	3.575	5.063

results in this case is due to the >60% porosity samples. The flatter pore geometry caused by the graphite likely leads to comparatively greater strength loss at high porosity due to likely greater pore connectivity. The comparison between the high temperature data sets is the most useful, given this, and the fact that SOFCs operate at this temperature. The poor fit of fixed  $\eta$  models suggests that a material-specific  $\eta$  value may be an oversimplification of the porosity-stress relationship in ceramics.

Samples tested at higher temperatures displayed a slightly higher flexural strength. Generally, it is expected that increasing temperature lowers strength of dense ceramics once plastic deformation processes become activated at high temperatures. [56] Below the temperature at which plastic deformation starts to occur, temperature has a minimal effect on flexural strength of dense ceramics. For dense GDC it has been demonstrated that the strength decreases by 19% between room temperature and 800 °C. [14] Porosity changes this behavior, by essentially creating a composite material, keeping the rate of change constant or increasing with temperature. [57] For porous GDC, thermal expansion places a compressive stress on any surface flaws that are sites for crack initiation and propagation. Additionally, the porosity helps reduce bulk stresses caused by thermal expansion. These two effects increase the material's fracture strength more than any decrease from plastic deformation at 625 °C.

Cross-sectional SEM of the fracture surfaces of the porous GDC samples, both PMMA and graphite, is shown in Figure 3.4. Figure 3.4a shows individual spherical pores left by the PMMA while Figure 3.4b has an inter-connected network of long pores left by the graphite flakes.

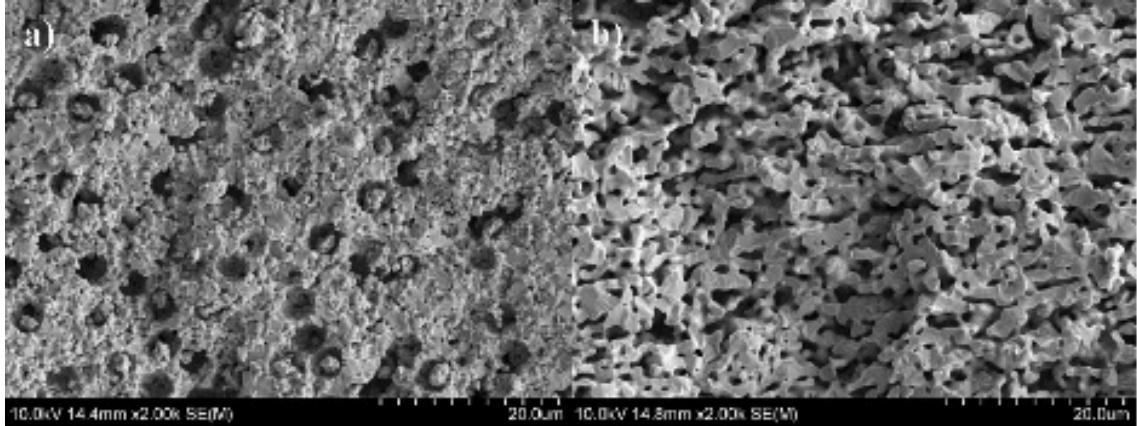


Figure 3.4: SEM micrographs of porous GDC bars made using: a) PMMA pore former; b) graphite flake pore former

The differences in quality of fit between Figure 3.3a and Figure 3.3b shows that the geometric factor is microstructurally dependent. Samples with porosity formed using PMMA spheres showed significantly greater strength as compared to samples with graphite-formed porosity. This can be explained by the effect of pore geometry on crack initiation and propagation in the ceramic. If a crack enters a pore, the pore can now be considered the new crack tip. The energy required to advance the crack is highly dependent on the geometry of the tip. For a spherical pore, this geometric factor is maximized and results in higher resilience to fracture. This is summarized by Equation 3.3 where  $\sigma_o$  is the stress at the crack tip,  $c$  is the length of the crack tip and  $\rho$  is the radius of curvature of the crack tip. [58]

$$\sigma_f = \frac{\sigma_o}{2} \sqrt{\frac{\rho}{c}} \quad (3.3)$$

Based on the mechanical behavior of these samples, porous ceramics should be designed and constructed such that the pore geometry is as low aspect ratio as possible to maximize strength.

### 3.3.2 Flexural Stress Orientation

Figure 3.5 shows the measure flexural strengths of a number of SOFC coupon samples. Anode support coupons were tested along with half-cells consisting of anode supports and electrolyte layers at temperatures ranging from 25 °C to 650 °C. The highest temperature test was repeated with coupons under reducing conditions (3% H<sub>2</sub>, balance Ar).

All unreduced sample types showed increased strength at elevated temperatures with little difference between types at a given temperature. The high-temperature reduced coupons displayed large differences in strength depending on the orientation of the sample. Tests in which the dense electrolyte layer was placed in compression resulted in the highest strength values, while the samples were weakest when the electrolyte was placed in tension. In reduced samples, the anode support layer becomes a ceramic-metal composite and is therefore somewhat elastic while the electrolyte remains a brittle ceramic. The electrolyte-in-compression condition maximizes the mechanical performance of the coupon by placing the layers in their preferred stress state.

Figure 3.6 shows the box plots for the unreduced SOFC coupon samples. A Student's t-test was used to statically determine if the means of samples tested at different conditions were equal based on 95% confidence. There is no discernible difference in the strength between the three sample types at each temperature. At elevated temperature there was a significant difference in the modulus of ASL only samples and samples with electrolyte in tension with a p-value of 0.0091. This

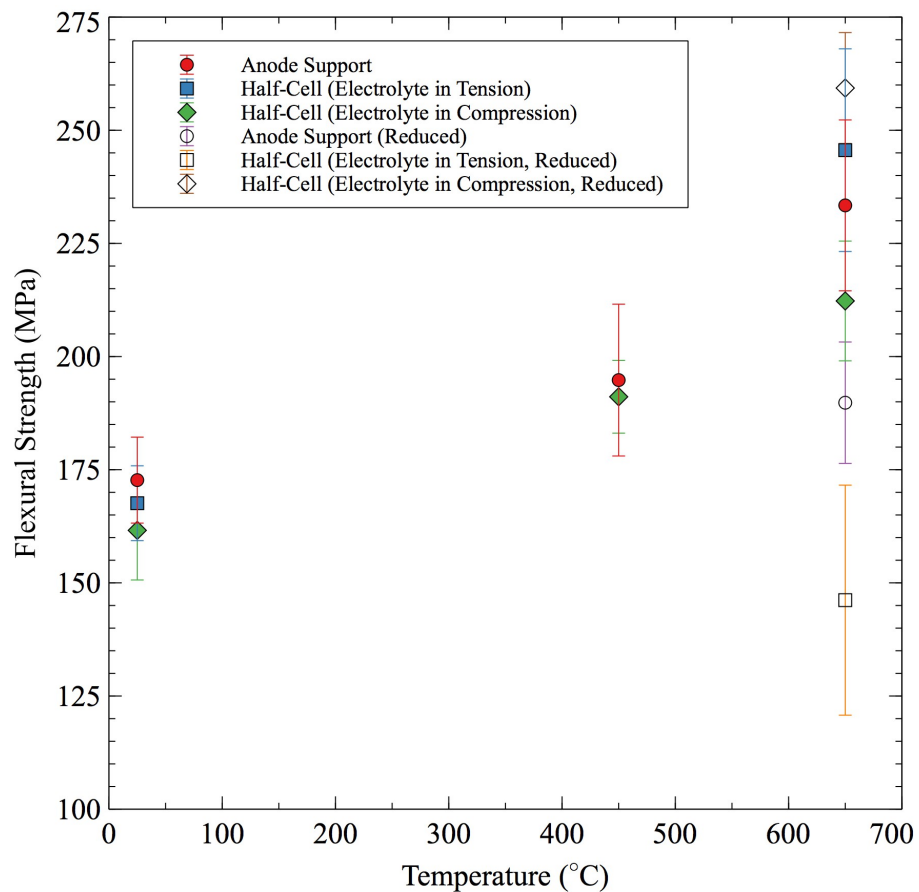


Figure 3.5: Temperature dependent strength of Ni-GDC anode supports and half-cells in both air (filled data points), and reducing atmosphere (3% H<sub>2</sub>, balance Ar, hollow data points), tested in both "electrolyte-up" and "electrolyte-down" orientations resulting in the electrolyte layer experiencing tension and compression, respectively

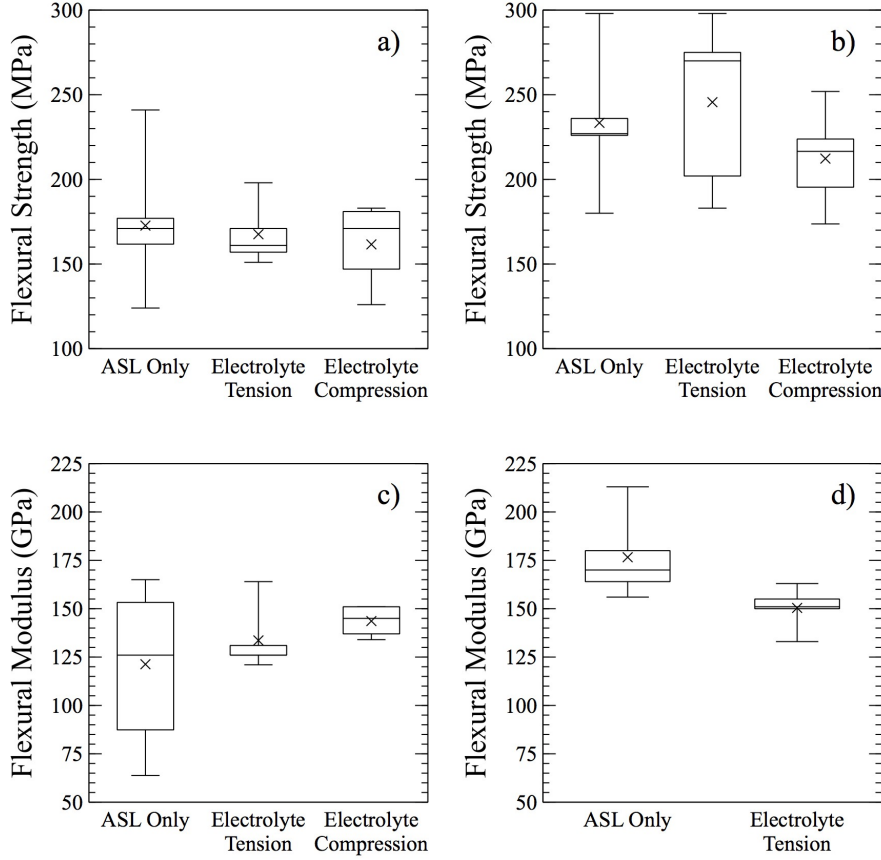


Figure 3.6: Flexural test measurements of coupons sample sets: a) Strength at 25 °C b) Strength at 650 °C c) Modulus at 25 °C d) Modulus at 650 °C

difference was not present at room temperature. As the materials reach elevated temperature, small differences in elasticity become magnified due to different thermal effects on dense and porous layers.

Additionally, SEM analysis of the fractured half-cells showed very good adhesion between layers (Figure 3.7). Delamination is a common failure mode in layered ceramics and one that would be particularly damaging to SOFCs due to resulting ionic conductivity loss between layers. [59] In the half-cell coupons, it was clear that

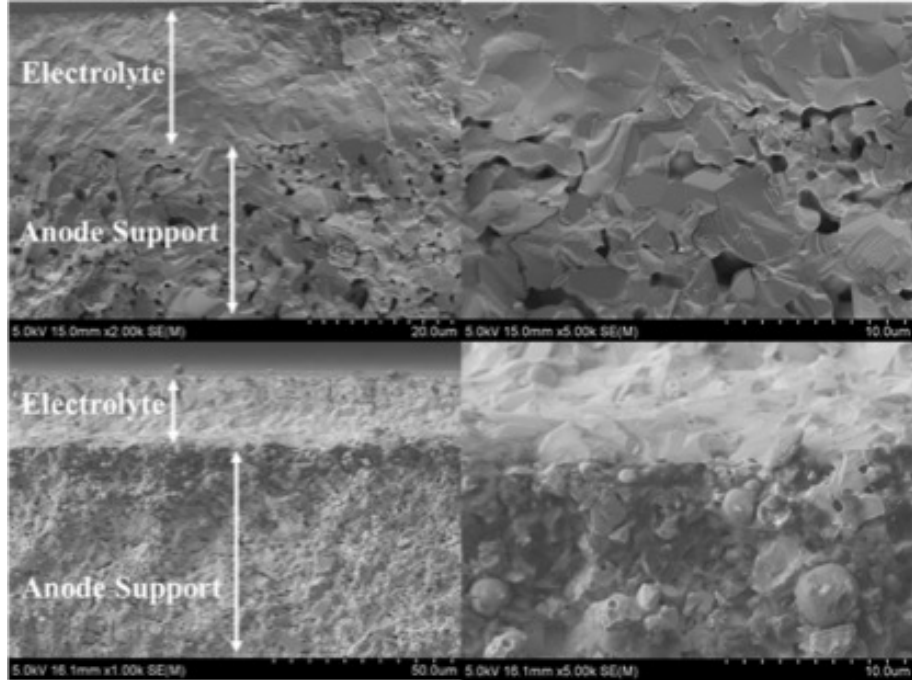


Figure 3.7: SEM micrographs of unreduced and reduced half-cell fracture surface: tested in air at 25 °C (top) and tested in reducing atmosphere at 650 °C (bottom), showing good adhesion between anode and electrolyte

the fracture plane contained mixed transgranular and intergranular fracture. Some grains were sheared through while others remained whole. The striations visible in Figure 3.7 are characteristic of fracture proceeding through a grain, while other grains remained whole.

### 3.3.3 Reduction and Strength

Mass loss of SOFC half-cell coupons exposed to reducing atmosphere at various elevated temperatures is shown in Figure 3.8. Mass loss is attributed to the reduction of NiO, used as a precursor in fabrication, to Ni metal, which serves as the catalyst for fuel oxidation and electronic conductor, and the reduction of ceria to  $\text{CeO}_{2-\delta}$ .

Table 3.2: Summary of fit parameters for reduction of NiO-GDC/GDC half-cell coupons under 3% H<sub>2</sub>, 3% H<sub>2</sub>O, 94% N<sub>2</sub> at different temperatures.

Temperature (°C)	Exponential Rate (h <sup>-1</sup> )	Asymptote (Mass %)
550	0.0463	89.78
575	0.135	89.09
600	0.182	88.36
650	0.512	87.75
750	0.821	87.87

Ni-GDC/GDC half cells showed the expected trend of increasing reduction rate at higher temperatures. Reduction curves were fit to an exponential decay and the summary of parameters is shown in Table 3.2. At 650 °C and 700 °C the reduction occurs very quickly, reaching steady state values after 18 hours. 550 °C showed a much slower mass loss than even 575 °C. At temperatures lower than 550 °C the kinetics are slow enough to tolerate a brief exposure to oxygen without re-oxidizing the sample. Of note in the reduction is that each temperature appears to approach a different asymptote, showing that the amount of NiO and GDC reduced at steady state is dependent on the temperature of the cell. This will affect the mechanical properties of the cells as it changes both the porosity and amount of nickel metal in the samples.

Ni-GDC/GDC fuel cells are sensitive to re-oxidation once reduced. Re-oxidation causes fracture of cells due to the large volume difference between NiO and Ni. [45]

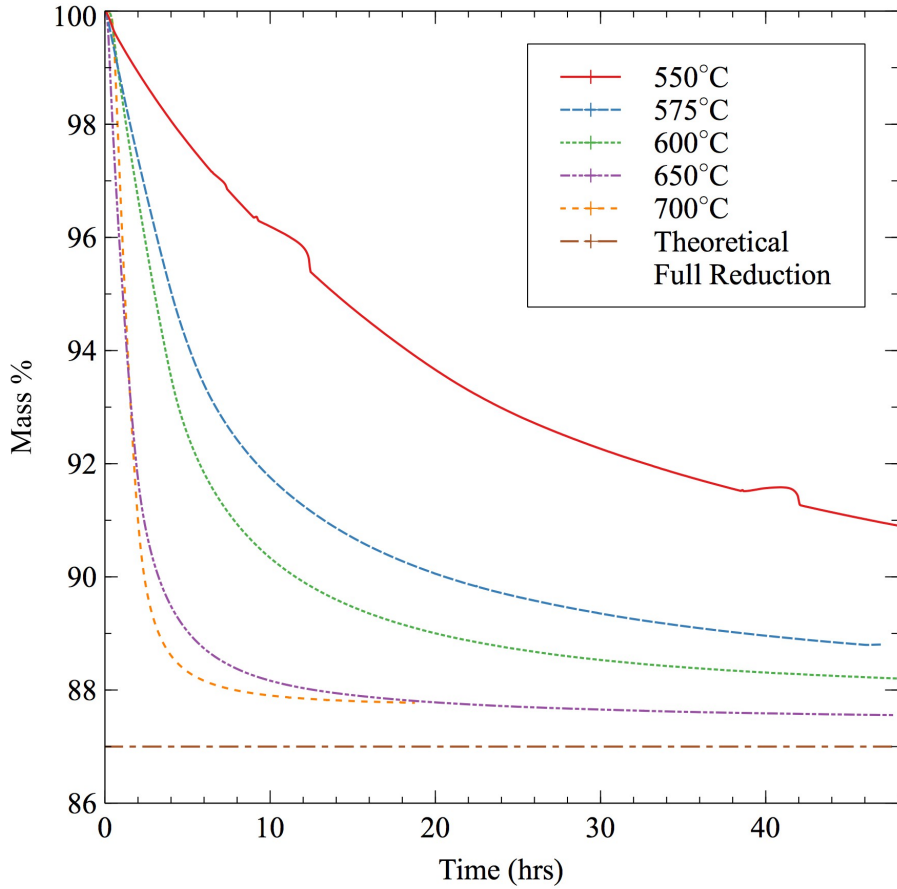


Figure 3.8: Thermogravimetric analysis curves for Ni-GDC/GDC half-cells showing mass loss over time at temperatures ranging from 550 °C to 750 °C in 3% H<sub>2</sub> 3% H<sub>2</sub>O balance N<sub>2</sub>, 50 sccm flow.

Based on the results from the TGA, the reaction rates below 300 °C are sufficiently slow to allow for the exposure of a reduced cell to oxygen without detrimental results. [60] To confirm this a sample was measured by TGA to ensure no mass gain during oxygen exposure and the strength of samples were tested to ensure there was no discernible difference between reduction methods.

For TGA analysis, a piece of a half cell was heated to 650 °C with a 10 °C min<sup>-1</sup> ramp rate and reduced. It was then cooled while still under reducing atmospheres. Once below 100 °C, it was exposed to simulated air (21% O<sub>2</sub>) for 18 hours, placed back into reducing atmosphere, and heated back up to 650 °C. Figure 3.9 shows the change in mass overlaid onto the temperature and oxygen partial pressure experienced by the sample. Following this treatment, the cell showed no mass gain during the oxygen exposure and continued to reduce at the same rate as before once it was returned to the initial conditions. This shows that cells which are cooled appropriately do not re-oxidize and could be handled in between a batch reduction of cells, and their assembly into a stack configuration.

Box plots of flexural strength and modulus of the in-situ reduced and batch reduced coupons are shown in Figure 3.10. Mechanical strength of half-cell coupons which had been reduced in-situ with an 18 hour reduction time showed no difference in strength when compared with coupons which had been previously batch reduced, cooled, and reheated under reducing environments. Both of these sample types showed a dramatic decrease in strength and Young's modulus compared to the un-reduced samples, but no statistically significant difference between treatments. The decrease in strength and modulus is due to the increase in porosity and conversion of

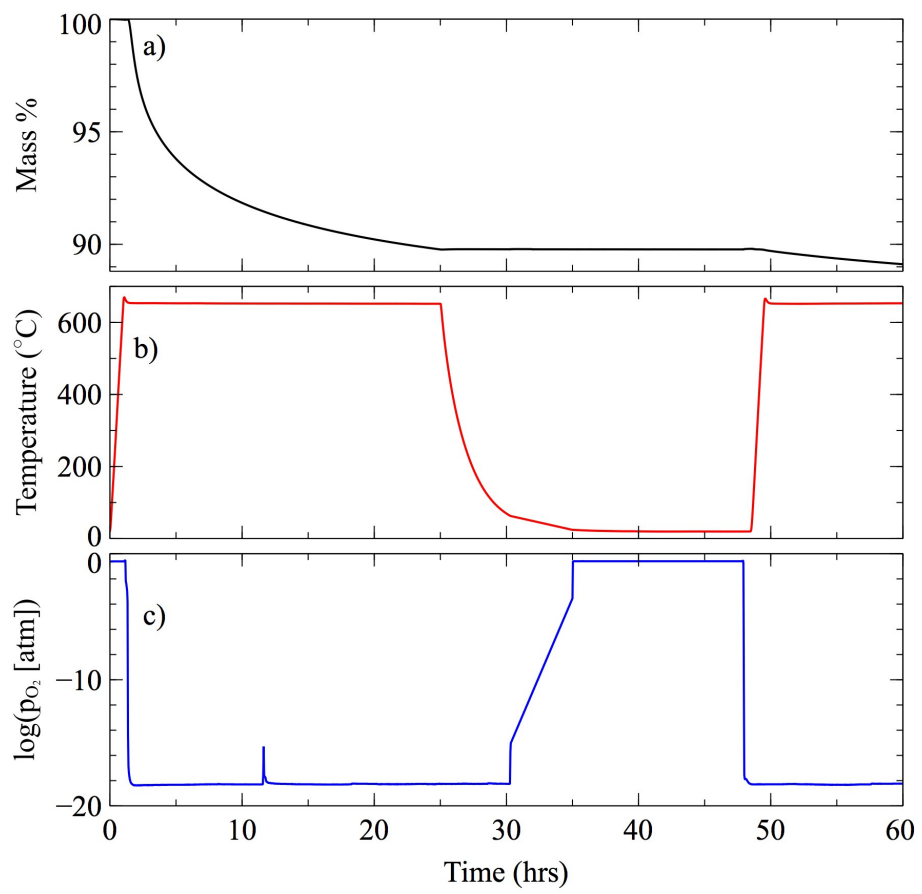


Figure 3.9: Thermogravimetric analysis of Ni-GDC/GDC half-cell showing no mass gain after reduction and exposure to room temperature and simulated air: a) Mass loss of interrupted reduction with exposure to ambient condition; b) Temperature of sample during cycle c) Oxygen partial pressure measured at the sample during cycle

NiO to metallic nickel in the cells. The decrease in variation between measurements in reduced cells is likely due to the increased number of large voids that form during NiO reduction.

The statistical similarity of the properties of the samples reduced via each method indicates that planar, Ni-GDC/GDC based SOFC ASL and half-cells are able to be safely reduced, cooled, and handled in ambient conditions without leading to damaging re-oxidation of the nickel anode material. This resilience could enable some degree of large-batch reduction of cell anodes prior to SOFC stack assembly, leading to more rapid startup and a greater degree of sealing control.

### 3.4 Conclusions

A temperature and atmosphere controlled three-point bend fixture was designed and built for use in a universal testing machine. SOFC coupons and component materials were evaluated for flexural strength at room temperature and IT-SOFC operating temperatures. In addition, the effects of porosity percent and pore geometry on flexural strength in GDC were investigated. Furthermore, the impact of temperature on the reduction rate of NiO in NiO-GDC SOFC anodes was examined along with the resilience to re-oxidation at ambient conditions of this SOFC component.

Pore geometry had a significant impact on the flexural strength of GDC10, with spherical pores showing the greatest resistance to fracture. This supports the concept of pores acting as the new crack tip once a crack has advanced to the pore. Additionally, samples tested at 650 °C were stronger than those at room temperature.

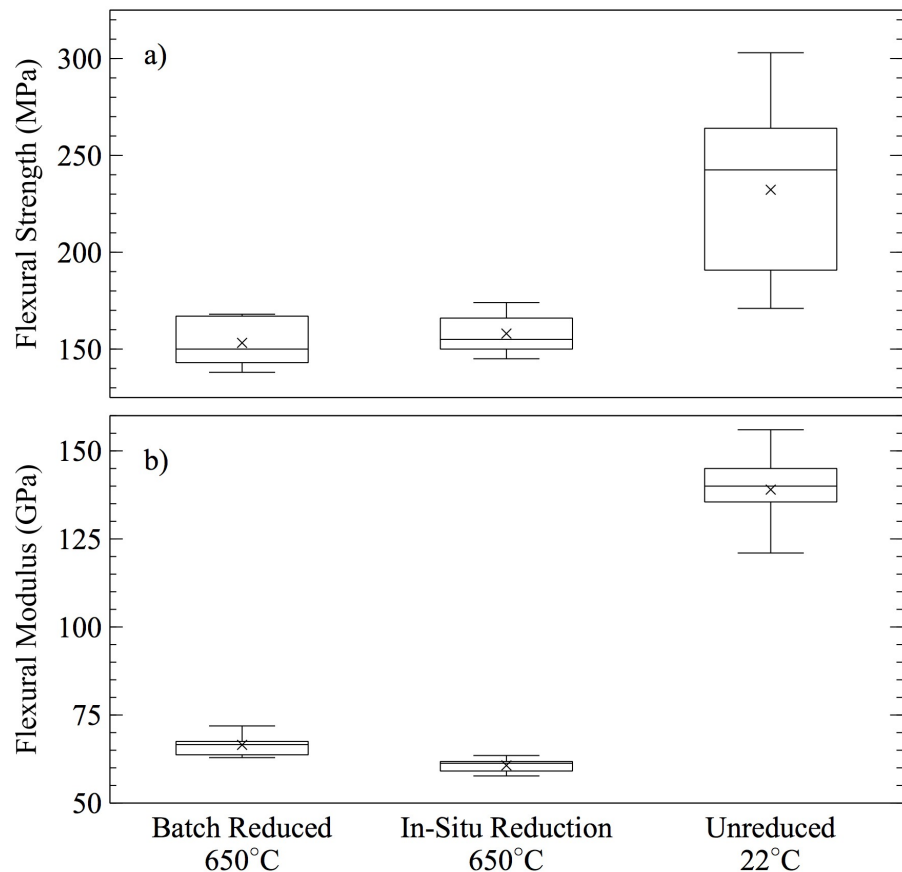


Figure 3.10: Flexural properties, a) strength and b) modulus, of Ni-GDC/GDC half-cell coupons after reduction via two different methods, compared to unreduced cells. Strength and modulus show decrease upon reduction but no significant difference between methods.

This is likely due to localized compressive stresses from thermal expansion of the material. This hypothesis is further supported by the results of testing NiO-GDC anode support coupons and half-cells. Coupons tested at 25 °C, 450 °C, and 650 °C displayed a linear strength dependence with temperature. There was no statistical difference in strength between anode support layers and half-cells composed of anode support and electrolyte at a given temperature in air. Half-cells in which NiO was reduced to Ni by exposure to H<sub>2</sub> at 650 °C displayed significant differences in strength when the electrolyte layer was subjected to compressive stress as opposed to tensile stress. Placing the ceramic electrolyte in compression and the metal-ceramic composite anode in tension resulted in the highest strength.

The reduction temperature of NiO-GDC/GDC half-cells was shown to have an effect on the rate of NiO reduction and amount of NiO reduced. At lower temperatures, the oxidation rate of Ni-GDC is slow enough that the anode can be exposed to air for significant periods below 100 °C. Any re-oxidation, combined with the cooling and re-heating of a cell back to 650 °C, showed no effect on the mechanical properties when compared to cells which had been reduced in-situ at 650 °C. These results indicate that it is possible to reduce and cool cell components to an extent without any additional effects to mechanical properties, allowing for more flexibility during cell manufacturing, stack assembly, and with quality control screenings.

This work leads to three important conclusions for the mechanical properties of GDC-based SOFCs using Ni anodes. Porous GDC used in anode supported SOFCs should be fabricated such that the pore geometry is spherical as this maximizes

energy required to advance a crack through the ceramic. Care should be taken in stack construction to ensure any out-of-plane cells are placed to compress the electrolyte and place the reduced anode in tension so as to lower the chance of fracture. Finally, it is possible to reduce the anodes of Ni-GDC SOFCs and then handle them at ambient conditions for quality control and stack assembly. This will remove a degree of variability from the manufacture of cells and stacks.

## Chapter 4: Defect chemistry and oxygen non-stoichiometry of double perovskite $\text{SrFe}_{0.2}\text{Co}_{0.4}\text{Mo}_{0.4}\text{O}_{3-\delta}$

### 4.1 Introduction

Solid-state electrochemical devices that perform energy conversion and storage rely on a material's abilities to transport charged carriers through the material. Devices such as solid-oxide fuel cells (SOFCs), oxygen separation membranes, and gas sensors can utilize materials which conduct both oxygen and electronic conductors, known as mixed ionic electronic conductors (MIEC), in the electrodes where both conductions need to occur simultaneously. [30] SOFCs in particular are limited in their application due to high operating temperatures, performance degradation due to fuel contamination, and inability to tolerate thermal and redox cycling. To improve the performance and reliability of SOFCs the operating temperature needs to be lowered from the intermediate temperature range ( $650\text{ }^\circ\text{C}$  to  $800\text{ }^\circ\text{C}$ ) to the low temperature range ( $<650\text{ }^\circ\text{C}$ ). [7] Additionally, the use of an all-ceramic anode, as opposed to the traditional nickel metal anode, would improve long term performance, resistance to poisoning or coking, and better match the thermal expansion of the rest of the cell. [24]

Perovskite structures have yielded number of MIECs with potential uses as electrode materials. [61–63]  $\text{Sr}_2\text{MgMoO}_6$  (SMM) and its related family of materials ( $\text{Sr}_2\text{MMoO}_6$ , where M is a transition metal dopant) yield good conductivities and catalytic actives. [64] The mixed valence state of Mo(VI)/Mo(V) provides high electronic conduction while supporting oxygen vacancy formation. [65] If a dopant is used which has an overlapping redox couple band, such as Fe, electronic conduction can be further improved. Mo(VI) and Mo(V) are stable in both octahedral and tetrahedral coordination, further adding stability to oxygen vacancy formation. [66]

A new material,  $\text{SrFe}_{0.2}\text{Co}_{0.4}\text{Mo}_{0.4}\text{O}_{3-\delta}$  (SFCM), is of particular interest because of its high conductivity and stability in hydrocarbon fuels. [67] SFCM takes advantage of the perovskite structure and multivalent cations similar to SMM, but the combination of both Fe and Co further increase the performance of the material. It has been shown that an SOFC using SFCM as an anode support material which had been infiltrated with nickel-gadolinium doped ceria nanoparticles is redox stable up to 30 cycles at 600 °C and that it provided long term catalytic activity without detriment to performance. [68, 69]

This work expands upon the fundamental knowledge of SFCM and aims to understand the defect chemistry and electronic structure which leads to its high conductivity. X-ray diffraction and Rietveld refinement show the phase stability and lattice parameter changes of SFCM across partial pressures of oxygen ( $p_{\text{O}_2}$ ). Electrical conductivity is measured as a function of  $p_{\text{O}_2}$  to determine changes electrical conductivity types. Temperature programmed desorption spectroscopy was used to characterize the oxygen desorption as it occurs from the lattice. The

non-stoichiometry of SFCM was measured under oxidizing and reducing environments at various temperatures via thermogravimetric analysis and a defect equilibrium model and diagram is proposed from the data with results compared to SMM and other perovskite materials.

## 4.2 Experimental

### 4.2.1 Sample Preparation

SFCM was created from stoichiometric amounts of strontium carbonate ( $\text{SrCO}_3$ , Sigma-Aldrich), iron oxide ( $\text{Fe}_2\text{O}_3$ , Sigma-Aldrich), cobalt oxide ( $\text{Co}_2\text{O}_3$ , Infram Advanced Materials), and molybdenum oxide ( $\text{MoO}_3$ , Alfa-Aesar) using conventional solid-state methods. The constituents were ball milled for 24 hours in ethanol and dried using a 100 °C oven. Afterwards the powder was calcined at 1100 °C for four hours.

Dense SFCM bars were used to maximize the total mass and mass changes during thermogravimetric testing. Samples were made by combining SFCM powder with 0.6 wt% polyethylene glycol 600, 1.8 wt% ethylene glycol, and 0.6 wt% glycerol in isopropyl alcohol and ball milling overnight. After drying at 100 °C, the powder was ground by mortar and pestle, then pressed uniaxially into rectangular bars at 30 MPa, followed by isostatic pressing at 30 MPa. Bars were sintered by heating to 400 °C for one hour and then 1340 °C for four hours, using a  $3 \text{ }^\circ\text{C min}^{-1}$  heating and cooling rate. This produced bars with 97% theoretical density by Archimedes' technique.

#### 4.2.2 X-ray Diffraction

X-ray diffraction (XRD) was used confirm phase purity of the SFCM after synthesis and during the testing process. A Bruker D8 Advance with LynxEye was used with a Cu K $\alpha$  source. A step size of 0.02° was used with a dwell of 0.8 s was used. Rietveld refinement was performed on powder samples as synthesized, after oxidation in pure O<sub>2</sub> and after reduction in pure H<sub>2</sub> at 600 °C for both. GSAS-II was used to perform the refinement calculations and VESTA was used to visualize the unit cell. [40, 41]

#### 4.2.3 Conductivity

Electrical conductivity was measured using the four-wire technique and a Stanford SR 830 lock-in amplifier. A bar shaped sample with the dimensions of 6.46 mm × 3.3 mm × 1.3 mm was used. Gold paste was used as a current collector, and the current range was between 0.005 to 0.05 A. A yttria-stabilized zirconia (YSZ) oxygen sensor operating at 800 °C was used to monitor the changes in oxygen partial pressures. Intermediate p<sub>O<sub>2</sub></sub> ranges were not tested due to instability between SFCM and the CO and CO<sub>2</sub> required to obtain those p<sub>O<sub>2</sub></sub>.

#### 4.2.4 Thermogravimetric Analysis (TGA)

Changes in mass of SFCM were measured by a Cahn D200 microbalance with the sample suspended down a quartz tube into a furnace. The furnace used to heat the sample and quartz tube was controlled by a PID controller with a K-type

thermocouple placed immediately below the sample inside the quartz tube. Gas flow was controlled at consistent 50 sccm by mass flow controllers, which mixed dry nitrogen, oxygen, hydrogen, and humidified nitrogen to obtain the  $p_{O_2}$  desired. Measurements of the  $p_{O_2}$  were taken by a calibrated YSZ oxygen sensor at 800 °C located before the sample. Again, intermediate  $p_{O_2}$  ranges were not able to be tested due to SFCM's incompatibility with the species required to create that environment.

To prepare the sample, it was pre-weighed, wrapped in platinum wire and suspended from the balance, placed in the furnace with simulated air (21% O<sub>2</sub>, 79% N<sub>2</sub>) flowing. Once the mass had stabilized, the furnace was heated to 800 °C to allow for any organic contamination to burn off. After the mass stabilized at this elevated temperature the sample was introduced to various environments. The mass of the sample would be noted only after steady state had been reached for a condition. After testing a sample, a bar of alumina was cut to the same dimensions as the sample and the process was repeated to obtain a blank which could be subtracted from the measurements to remove buoyancy effects.

Oxygen non-stoichiometry was calculated using Equation 4.1, where  $\Delta\delta$  is the change in oxygen stoichiometry,  $MW_{SFCM}$  is the molecular weight of SFCM (208.74 g mol<sup>-1</sup>),  $MW_O$  is the molecular weight of oxygen (16.0 g mol<sup>-1</sup>),  $w_{sample}$  is the weight of the sample, and  $\Delta w$  is the weight change as recorded by the TGA. The oxygen vacancy concentration ( $[V_O^{••}]$ ) is calculated using Equation 4.2, where  $\rho$  is the density of SFCM, and  $N_A$  is Avogadro's number. To calculate the oxygen vacancy concentration, the non-stoichiometry of SFCM at a point needs to be established. For this work, based on the plateau present in the data at oxidizing conditions, it is

assumed that in a pure oxygen environment ( $\log(p_{O_2}) = 0$ ) all oxygen vacancies are filled with no oxygen interstitial or surface species, thus  $\delta = 0$ .

$$\Delta\delta = \frac{MW_{SFCM}}{MW_O w_{sample}} \Delta w \quad (4.1)$$

$$[V_O^{\bullet\bullet}] = \frac{\delta\rho N_A}{MW_{SFCM}} \quad (4.2)$$

#### 4.2.5 Temperature Programed Desorption

The effluent from the TGA was used as the inlet to a mass spectrometer (MS) to perform temperature programmed desorption. The sample was prepared as before and heat treated to remove any carbon contaminants but was allowed to cool under simulated air. It was then heated to 800 °C at 5 °C min<sup>-1</sup> under a 50 sccm flow of nitrogen as the MS measured the 32 m/z signal which corresponded to O<sub>2</sub> desorption. Additional m/z signals were monitored to observed for other species.

### 4.3 Results and Discussion

The XRD patterns obtained after reduction and oxidation, in addition to the fresh as synthesized powder and the pattern obtained from Rietveld refinement, are presented in Figure 4.1a. An unordered tetragonal, perovskite structure was used as a starting point for Rietveld refinement based on the structures of Sr<sub>2</sub>CoMoO<sub>6</sub>, Sr<sub>2</sub>NiMoO<sub>6</sub> and Sr<sub>2</sub>Fe<sub>0.75</sub>Co<sub>0.25</sub>MoO<sub>6</sub>. [64, 70] Results from the Rietveld refinement calculations are given in Table 4.1. The unordered double perovskite unit cell from the refinement is presented in Figure 4.1b and was used to create the theoretical XRD pattern for visual comparison.

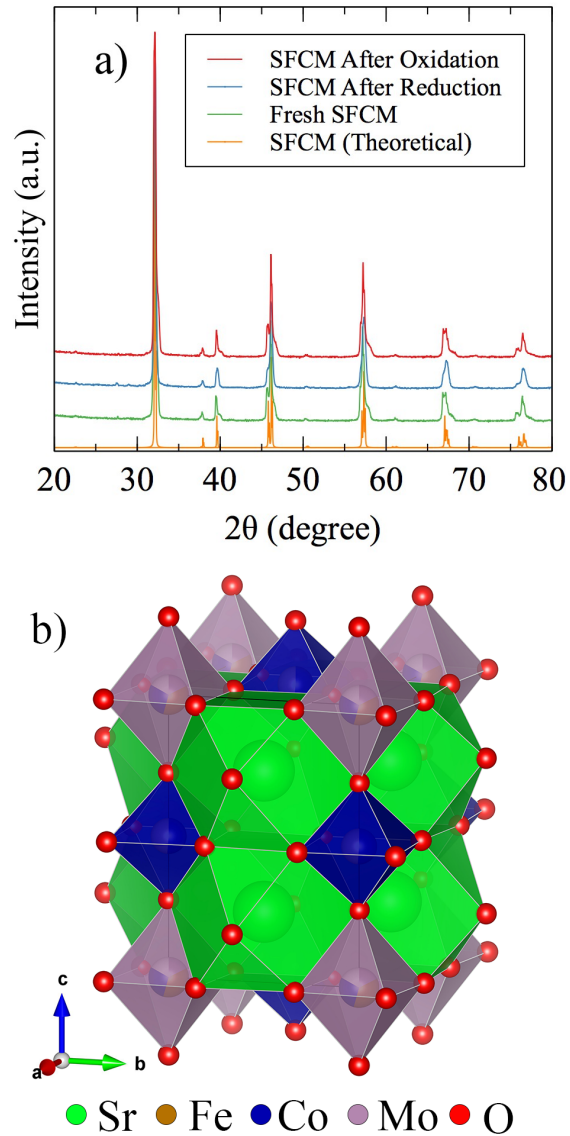


Figure 4.1: a) Powder XRD patterns of SFCM samples taken after synthesis, reduction, and oxidation compared to pure phase SFCM diffraction pattern. b) Crystal structure of ordered double perovskite SFCM.

Table 4.1: Refinement results of SFCM before and after exposure to reducing and oxidizing environments

Condition	Oxidized	Fresh	Reduced
Space Group	I 4 $\overline{m}$	I 4 $\overline{m}$	I 4 $\overline{m}$
a (Å)	5.5636(2)	5.5558(3)	5.5544(2)
c (Å)	7.9310(2)	7.9184(3)	7.9204(2)
Volume (Å <sup>3</sup> )	245.49	244.41	244.35
Sr-O1 (Å)	2.794	2.790	2.790
Sr-O2 (Å)	2.789	2.785	2.784
M1-O1 (Å)	1.993	1.990	1.990
M1-O2 (Å)	1.782	1.780	1.780
M2-O1 (Å)	1.950	1.948	1.947
M2-O2 (Å)	2.183	2.180	2.180
Phase Purity (% SFCM)	85.24	76.08	100.0
R <sub>w</sub> (%)	14.277	15.519	17.324

SFCM proved to be stable under reducing conditions, being pure phase based on the Rietveld refinement.  $\text{Sr}_2\text{Co}_{1.2}\text{Mo}_{0.8}\text{O}_6$  was found to be an impurity in SFCM under ambient and oxidizing conditions. This secondary phase reversibly disappears when returning to reducing conditions. Overall phase purity remains at greater than 76% as synthesized, 85% under oxidizing conditions and at 100% after reduction.

Changes in the SFCM component of the XRD pattern occur after different environmental treatments. These are attributed to the changes in oxidation state, defect concentrations, and thus lattice parameter of the sample after exposure to different  $p_{\text{O}_2}$ . The changes to the lattice were calculated from Rietveld refinements of the XRD data and summarized in Table 4.1. Reduction of SFCM from an as synthesized state causes a 0.025% decrease in  $a$  and the volume of the unit cell and a 0.025% increase in  $c$ . These are result of the bond lengths between Sr-O2 and M2-O1 decreasing. Oxidizing the SFCM results in a 0.14% increase in  $a$  and a 0.16% increase in  $c$  resulting an 0.44% increase in cell volume. This is the result of all bond lengths increasing all bond lengths by 0.002 to 0.004 Å. Perovskite structures can have small to no changes in lattice parameter due to chemical expansion, which is observed in this sample, where the largest observed change in lattice parameter is 0.16%. [34] Additionally, when changes do occur, perovskites have been shown to have anisotropic chemical expansion, as such with SFM where  $a$  increases upon reduction while  $c$  decreases. [71] As a result, SFCM shows very little change to lattice parameters as a result of changing metal oxidation states or vacancy creation as it undergoes reduction or oxidation.

SFCM has a conductivity dependence typical of MIEC conductors, as shown

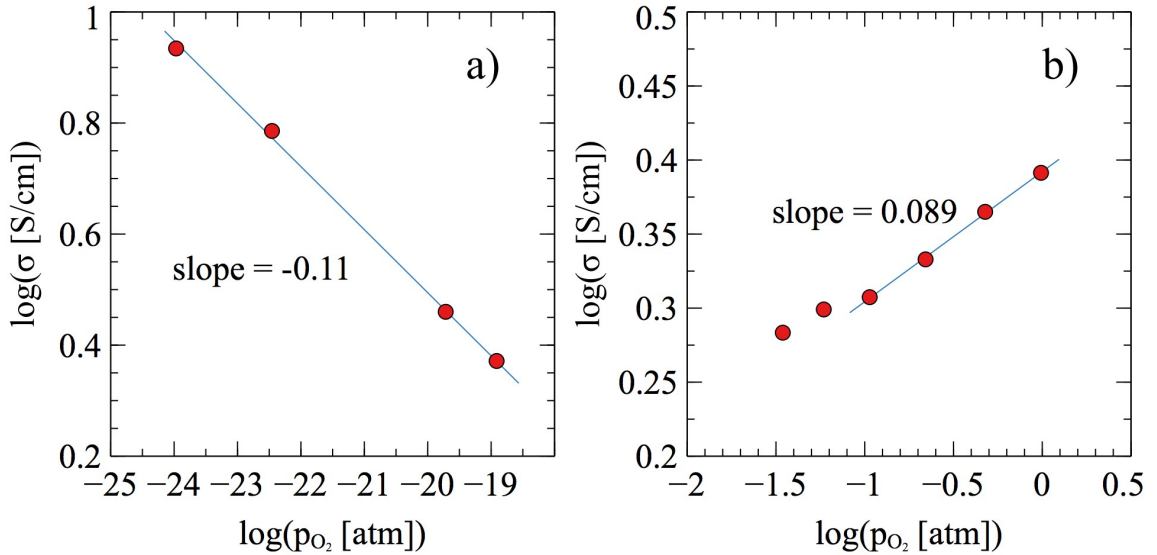


Figure 4.2: Total conductivity as  $p_{O_2}$  changes under a) reducing and b) oxidizing conditions at 600 °C.

in Figure 4.2. At high  $p_{O_2}$  ranges ( $10^{-1.5}$  atm to 1 atm) it shows p-type conductivity, where conductivity increases with  $p_{O_2}$ . Down to  $10^{-1}$  atm, the change in conductivity is linear with a slope of 0.089 (log-log scale). Below  $10^{-1}$  atm the slope changes away from the previous trend, suggesting a change in the predominant charge carrier. At low  $p_{O_2}$  ranges ( $10^{-24}$  atm to  $10^{-19}$  atm) the conductivity behaves linearly with n-type conductivity, increasing at lower  $p_{O_2}$ , with a slope of  $-0.11$  (log-log scale). The sample measured in this work exhibited a lower conductivity than that reported in previous work (2 S/cm compared to 30 S/cm at 600 °C). [67] This difference is likely due to sample preparation creating additional porosity, reducing the absolute conductivity, but the trend with  $p_{O_2}$  remains consistent.

Based on the slopes in the high  $p_{O_2}$  region, at least two defect regimes exist in that area transitioning near  $10^{-1}$  atm. Both high and low  $p_{O_2}$  regions have slopes

much lower than +1/4 or -1/4 respectively, which indicates that the relationship between electronic charge carriers and oxygen is dependent of the other defect species in the material. In fact, the lower than 1/4 slope suggest that the electronic charge carries are taken up by the other species, decreasing the expected number based on  $p_{O_2}$  change. At low  $p_{O_2}$ , n-type conductivity is promoted by the generation of oxygen vacancies, freeing electrons as negative electronic charge carriers to maintain charge balance. Some of these electrons are consumed by the reduction of B-site metals to lower oxidation states. At high  $p_{O_2}$ , oxygen vacancies are filled and B-site metals oxidize, consuming electrons and allowing for the creation of holes, promoting p-type conductivity. The different slopes between high and low  $p_{O_2}$  are the result of different defect species interacting with the electronic carriers at different points in the reduction.

TPD was performed in conjunction with TGA to determine the extent of oxygen desorption from SFCM. Figure 4.3 presents the data from the TGA on top with the mass and rate of mass change, while the 32 m/z signal from oxygen in the mass spectrometer is on bottom. The cyclic noise present in both mass and MS signals is due to an improperly tuned PID controller on the TGA furnace, but the noise remained much lower than the measured signal. The rate of mass loss matches the oxygen signal from the MS, confirming that oxygen is generated from SFCM when heated under mild reducing conditions and is the cause for mass loss in the sample. SFCM shows two maxima for the rate of oxygen loss during heating. The first,  $\alpha$ , occurs at 405 °C with the second peak,  $\beta$ , occurring near 800 °C. The MS monitored for other species, such as carbon and water, but no significant amounts

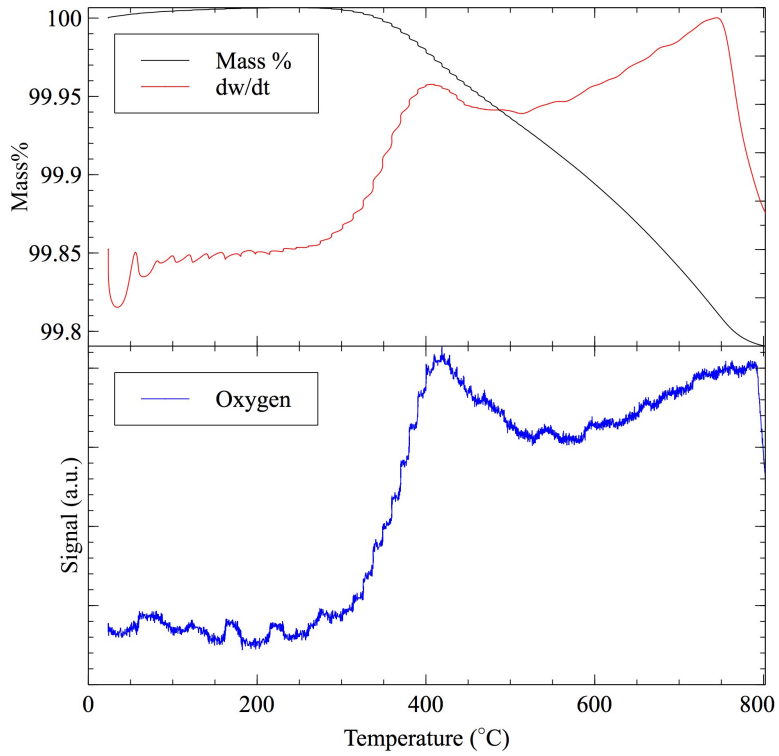


Figure 4.3: Temperature programmed desorption of oxygen in SFCM with mass loss from TGA (top) and oxygen desorption from MS (bottom) as it is heated to 800 °C in N<sub>2</sub>.

were observed.

Perovskite materials have oxygen desorption classified based on the temperature which it occurs. Low temperature desorption (referred to as  $\alpha$ ), occurs due to the reduction of metals and desorption of oxygen near the surface. High temperature desorption (referred to as  $\beta$ ), takes place when oxygen is able to diffuse through the bulk and be released. [72] SFCM shows both  $\alpha$  and  $\beta$  desorption, indicating that both the surface and lattice can generate oxygen vacancies due to the reduction of the different B-site cations and that those vacancies are mobile to move from the bulk to the surface. SMM shows only  $\beta$  desorption above 800 °C and while

$\text{Sr}_2\text{Fe}_{1.5}\text{Mo}_{0.5}\text{O}_6$  (SFM) has  $\alpha$  desorption from 400 °C to 800 °C and  $\text{Sr}_2\text{CoMoO}_6$  (SCM) desorbs starting below 400 °C. [73, 74] In the case of SFM and SCM, the use of the multivalent Fe or Co allows for reduction at a lower temperature than SMM. For SFCM, the same effect is seen through the combined use of Fe and Co. This demonstrates SFCM's ability to begin to create oxygen vacancies at 400 °C and exchange oxygen with the bulk lattice starting as low as 450 °C and peaking near 800 °C.

Oxygen non-stoichiometry and oxygen vacancy concentrations are shown in Figure 4.4 at 600 °C for high and low  $p_{\text{O}_2}$  regions. At high  $p_{\text{O}_2}$ , SFCM has two linear regions, changing between them near  $10^{-0.75}$  atm. The transition between regions in oxygen stoichiometry occurs at a similar  $p_{\text{O}_2}$  to where the conductivity changes in Figure 4.2. This change is the result of a change in defect regime regions. In the low  $p_{\text{O}_2}$  region, a linear trend occurs down until  $10^{-21}$  atm where the non-stoichiometry rate increases. Due to the pure phase XRD under reducing conditions, it is not likely that the increase in non-stoichiometry is due to phase decomposition and instead is a change in regimes where more oxygen vacancies are present.

SFCM shows similar trends in non-stoichiometry to SMM and SFM, but with the added complexity expected from the additional B-site species. SMM approaches a plateau in oxygen content as it reached 1 atm of oxygen the same as SFCM but possesses a constant slope of -1/6 when plotted on a log-log scale. [75] In comparison, SFCM has multiple slopes associated with the degree of vacancy formation, as shown in Figures 4.4c and 4.4d. These different slopes can be attributed to the reduction of the three different B-site cations at different  $p_{\text{O}_2}$ . As an oxygen vacancy forms, the

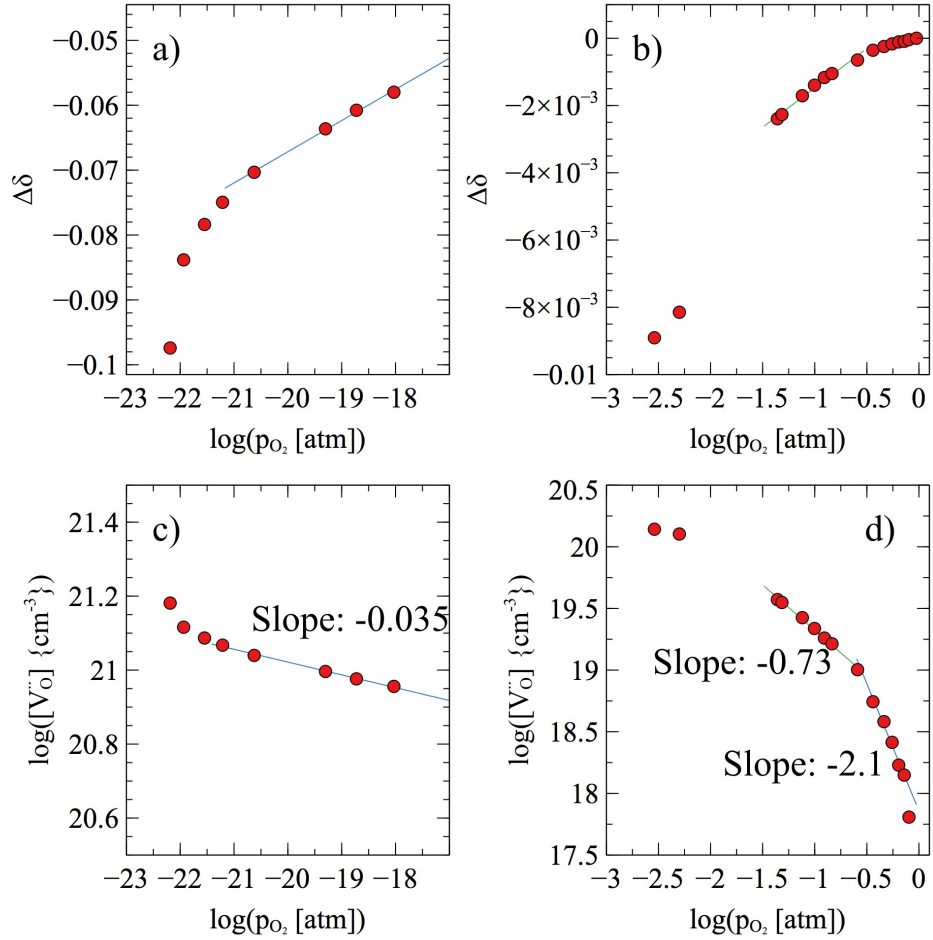


Figure 4.4: Non-stoichiometry (top) and corresponding oxygen vacancy concentration (bottom) of SFCM under oxidizing conditions (right) and reducing conditions (left) at 600 °C.

electrons required to maintain charge balance can be accommodated by the reduction of Fe, Co, or Mo, each with an independent equilibrium constant, whereas SMM only has Mo reduction to accommodate electrons from oxygen vacancy generation. The high slopes of Figure 4.4d show how SFCM can generate more oxygen vacancies at lower  $p_{O_2}$  because of the Fe and Co cations. SFM and SMM show similar amounts of non-stoichiometry at the same  $p_{O_2}$  but at 1000 °C. [76] SFCM shows almost twice the non-stoichiometry at a much lower temperature of 600 °C. SFCM’s ability to create vacancies at higher  $p_{O_2}$  results in a larger accumulated vacancy concentration at low  $p_{O_2}$ .

TGA non-stoichiometry measurements were performed on the same sample at 400 °C, 500 °C, and 600 °C which are temperatures in the low temperature-SOFC range. Figure 4.5 shows the non-stoichiometry measurements for the sample tested at three temperatures in the low  $p_{O_2}$  (a) and high  $p_{O_2}$  (b) regions.

As expected lowering the temperature reduces the non-stoichiometry at a given  $p_{O_2}$  and decreases the  $p_{O_2}$  at which transitions between regimes occur. At 400 °C oxygen vacancy formation decreases considerably compared to 500 °C and 600 °C. This aligns with the results of the TPD (Figure 4.3) where SFCM does not start desorbing oxygen until 350 °C to 400 °C and then only from the surface.

To best understand what is occurring in SFCM a defect equilibrium diagram and model need to be created to relate the changes in conductivity and non-stoichiometry to the concentration of the various defects present in the material. Defect reactions with their corresponding equilibrium equations are given in Equations 4.3–4.6, which use Kröger–Vink notation, where a species is denoted by the site it sits on (subscript)

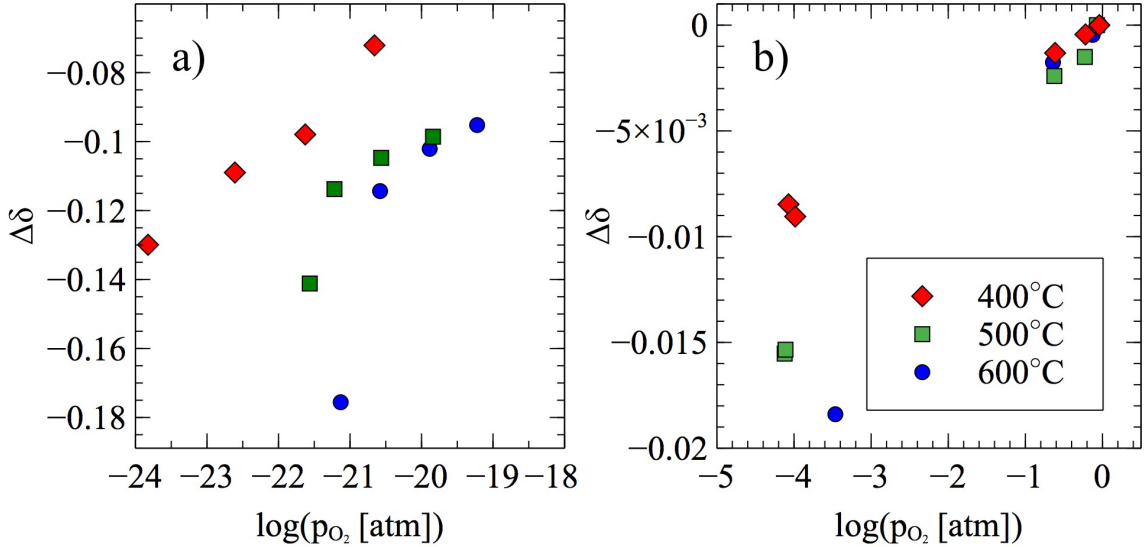
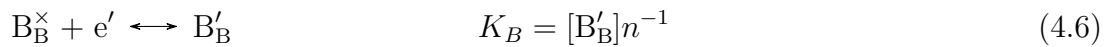
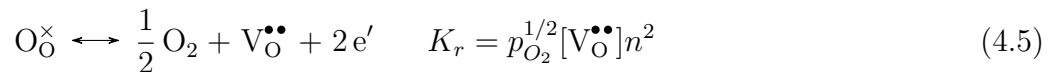


Figure 4.5: Non-stoichiometry of SFCM as  $p_{O_2}$  changes at 400 °C, 500 °C, and 600 °C.

and the relative charge to the site's expected valency (superscript). For example,  $V_O^{\bullet\bullet}$  is a vacancy in an oxygen site with a 2+ charge and  $B'_B$  is a B-site metal in a B-site with a 1- charge. K represents the equilibrium, or mass-action, constant for the reaction. To simplify the set of equations, Equation 4.6 represents the combined reduction of any B-site cation (Fe, Co, or Mo).  $\beta$  is the ratio of A-site vacancies to B-site vacancies from Schottky defects.



The Duncan-Wachsman approach allows for the accurate solution of defect

Table 4.2: Equations for defect equilibrium under reducing conditions

Defect	Equation
n	$K_r^{\frac{1}{2}} p_{O_2}^{-\frac{1}{4}} \left( \frac{3}{4} K_r^{\frac{1}{2}} p_{O_2}^{-\frac{1}{4}} + \left( \frac{1}{2} [B'_B] \right)^{\frac{3}{2}} \right)^{-\frac{1}{3}}$
p	$K_i K_r^{-\frac{1}{2}} p_{O_2}^{\frac{1}{4}} \left( \frac{3}{4} K_r^{\frac{1}{2}} p_{O_2}^{-\frac{1}{4}} + \left( \frac{1}{2} [B'_B] \right)^{\frac{3}{2}} \right)^{\frac{1}{3}}$
[V_O^{••}]	$\left( \frac{3}{4} K_r^{\frac{1}{2}} p_{O_2}^{-\frac{1}{4}} + \left( \frac{1}{2} [B'_B] \right)^{\frac{3}{2}} \right)^{\frac{2}{3}}$
[V_A'']	$\beta K_s^{\frac{1}{\beta+1}} \left( \frac{3}{4} K_r^{\frac{1}{2}} p_{O_2}^{-\frac{1}{4}} + \left( \frac{1}{2} [B'_B] \right)^{\frac{3}{2}} \right)^{-\frac{2}{\beta+1}}$
[V_B''']	$K_s^{\frac{1}{\beta+1}} \left( \frac{3}{4} K_r^{\frac{1}{2}} p_{O_2}^{-\frac{1}{4}} + \left( \frac{1}{2} [B'_B] \right)^{\frac{3}{2}} \right)^{-\frac{2}{\beta+1}}$
[B'_B]	Constant

equations across  $p_{O_2}$  regions using dominant defect triads, compared to the dominant defect pairs of the Brouwer approach which lead to an inaccurate results near transition regions. [77] The Duncan-Wachsman approach is needed in this work to model the defect equilibria because the measured  $p_{O_2}$  range crosses various Brouwer regions, as indicated by the non-linearity of Figure 4.4c. Using this method, Equations 4.3–4.6 can be solved to give models of the defect concentrations across  $p_{O_2}$ . Due to the fact that impurity phases form under oxidizing conditions, only the pure phase, reducing  $p_{O_2}$  were solved for. Table 4.2 gives the resulting equations from the Duncan-Wachsman approach for the defect concentrations at these  $p_{O_2}$ . To allow for the solution of the equations, it was assumed that all B-site metals will have already reduced to their maximum potential, that is  $[B'_B]$  is constant, in the  $p_{O_2}$  range of interest.

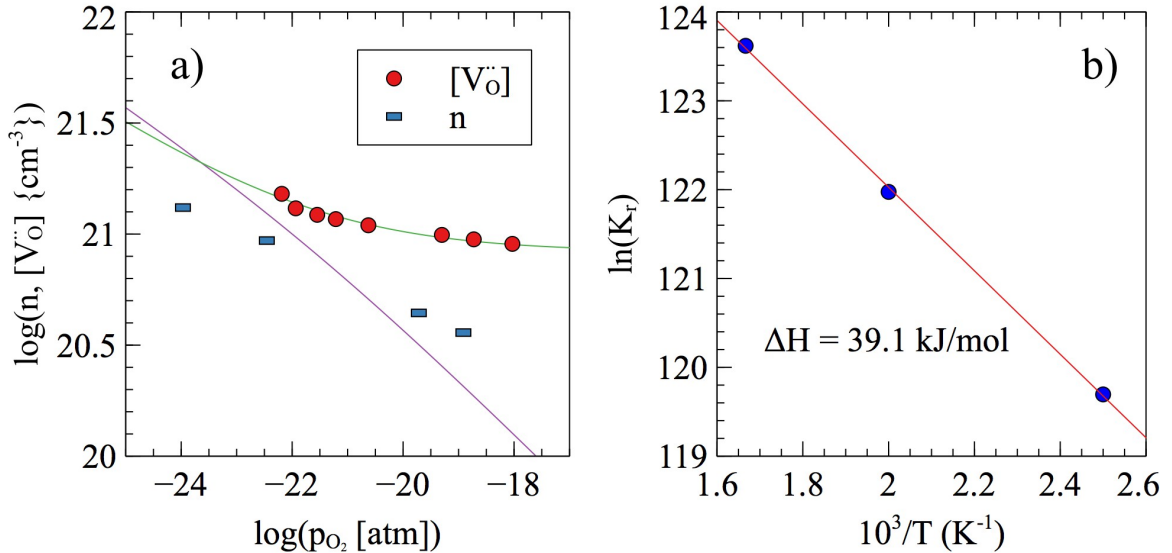


Figure 4.6: Oxygen vacancy and electronic defects in SFCM based on conductivity and TGA non-stoichiometry.

Using the TGA and conductivity data with the equations given in Table 4.2 the reaction equilibrium constants can be fitted to obtain a general defect equilibrium diagram for reducing  $p_{O_2}$  as shown in Figure 4.6a. The electron mobility was calculated from the fitted data at 600 °C to be  $0.0408 \text{ cm}^2 \text{ V}^{-1} \text{ s}^{-1}$ , which is within the range for small polaron defects for SMM. [75] By fitting and plotting the values of  $K_r$  from various temperatures (Figure 4.6b), the enthalpy of formation for oxygen vacancies was found to be  $39.1 \text{ kJ mol}^{-1}$  in SFCM under reducing conditions.

While the fit for the oxygen vacancy concentration in Figure 4.6a fits well, the model predicts a steeper slope for the concentration of electrons. The cause of this is from the assumption that  $[B'_B]$  is a constant, made while solving the defect reaction equations. In reality, while most B-site metals will have reduced, a portion will still be reducing at the low  $p_{O_2}$ , decreasing the overall number of

conduction electrons, and reducing the  $p_{O_2}$  dependence of  $n$ . At low  $p_{O_2}$  both the concentrations of electrons and oxygen vacancies are on the same order of magnitude promoting mixed conduction. SFCM has an enthalpy of formation lower than that of comparable materials. SFM and SMM have much higher enthalpies of  $253\text{ kJ mol}^{-1}$  and  $110\text{ kJ mol}^{-1}$  respectively. [75, 76]  $\text{SrFeO}_{3-\delta}$  has a more comparable, but still greater, enthalpy of  $80\text{ kJ mol}^{-1}$ . [78] This low enthalpy of formation of oxygen vacancies in SFCM allows for a greater range of non-stoichiometry and thus SFCM's high performance.

#### 4.4 Conclusions

SFCM has potential as an electrode material in a number of electrochemical device applications. Specifically, it has a potential to replace nickel-based anodes in SOFCs due to its high conductivity and redox stability, creating an all-ceramic anode. SFCM forms impurity phases when heated at  $600\text{ }^\circ\text{C}$  under oxidizing environments but becomes pure phase with reduction. It also exhibits very small chemical expansion with changing  $p_{O_2}$ , in line with its perovskite structure. SFCM is an improvement over previous double perovskite materials because of high conductivity at temperatures below  $600\text{ }^\circ\text{C}$ . This is in part because SFCM supports the formation of oxygen vacancies at both surface and lattice positions shown by overlapping  $\alpha$  and  $\beta$  oxygen desorption, starting as low at  $350\text{ }^\circ\text{C}$  and continuing up until above  $800\text{ }^\circ\text{C}$ . Oxygen vacancies form more rapidly than other MIEC materials with decreasing  $p_{O_2}$  as combination of B-site cations enables reduction though a large range of

$p_{O_2}$  resulting in a low enthalpy of formation for oxygen vacancies at  $39.1 \text{ kJ mol}^{-1}$ .

Proposed defect equilibrium equations were given for the low  $p_{O_2}$  range, supported by thermogravimetric and conductivity measurements for the complex system. Thermogravimetry at lower temperatures demonstrated SFCM's activity until  $400^\circ\text{C}$  at which the amount of oxygen vacancy formation slows dramatically.

# Chapter 5: Flexural strength and flaw distributions of $\text{SrFe}_{0.2}\text{Co}_{0.4}\text{Mo}_{0.4}\text{O}_3$ based ceramic-supports for solid-oxide fuel cells at operating conditions

## 5.1 Introduction

New materials are regularly being developed for use in solid-oxide fuel cells (SOFCs) to lower operating temperatures and improve reliability and performance.

[7] Most of the development focuses on the catalytic activity and conductivity enhancement in the material. However, an important characteristic of these materials that needs to be studied are the mechanical properties. An SOFC must be able to be adequately compressed to create a gas tight seal between the anode and cathode compartments for it to function well. This means that the cell must withstand the induced stresses from sealing, heating, and reduction by fuels. Redox cycling presents an additional challenge, especially in nickel-based systems, because oxidation and reduction phase changes cause crack growth and failure after a few cycles.

[15, 16, 21, 79–82] A means of mitigating this problem is to use alternative, all ceramic anode system, such as  $\text{La}_{1-x}\text{Sr}_x\text{Cr}_{1-y}\text{Mn}_y\text{O}_3$ ,  $\text{Sr}_{0.94}\text{Ti}_{0.9}\text{Nb}_{0.1}\text{O}_{3-\delta}$ ,  $\text{Ba}_{0.98}\text{La}_{0.02}\text{SnO}_3$ , or  $\text{Sr}_2\text{MgMoO}_6$  (SMMO). [24–30]

One new material of interest is the double perovskite  $\text{SrFe}_{0.2}\text{Co}_{0.4}\text{Mo}_{0.4}\text{O}_3$  (SFCM). [67–69] SFCM is a mixed ionic electronic conductor (MIEC) based off SMMO and other similarly structured anodes. The double perovskite family of materials, similar to SFCM and SMMO, have potential use as SOFC components due to the ability of the stable perovskite structure to generate and conduct oxygen vacancies and the multivalent cations allowing for electronic conduction and catalytic activity. [65, 66, 83] A similar thermal expansion of SFCM to GDC increases the compatibility between the components and reduces the chances of cracking and cell failure. SFCM has a high conductivity of  $\sim 35 \text{ S/cm}$  at  $650^\circ\text{C}$  and is stable to redox cycling making it a promising material.

As an SOFC cell is heated and reduced, there is the possibility for changes to occur in the fracture toughness or flaw distribution of the materials. Heating causes the materials to expand, increasing their interatomic distances, and reduction creates oxygen vacancies weakening bonds. [84, 85] Flaws can grow, combine, or change shape during these processes further affecting the overall strength. Equation 5.1 demonstrates how various factors impact the strength of a sample, where  $\sigma$  is the strength,  $K_{Ic}$  is the fracture toughness,  $Y$  is the shape factor for the flaw which caused failure and  $a$  is the size of the flaw. [86] The fracture toughness and flaw distributions play a direct role in the overall strength of the cell.

$$\sigma = \frac{K_{Ic}}{Y\sqrt{a}} \quad (5.1)$$

Most research focuses on measuring and comparing the Young's moduli of different materials as it changes with environment. [20, 57, 87, 88] While the modulus

can be correlated to the fracture strength of the cell, direct measurement of flexural strength remains the best means to characterize the strength of the cell. This work characterizes the changes which occur in fracture toughness and flaw distributions of SFCM, SFCM-GDC anode support layer (ASL), and SFCM-GDC/GDC half-cells when exposed to oxidizing and reducing conditions up to 600 °C by use of flexural testing and Weibull analysis. Additionally, electrical conductivity, thermogravimetric analysis, and thermal expansion are used to determine the causes for changes in mechanical properties under these conditions.

## 5.2 Experimental

### 5.2.1 Sample Preparation

SFCM powder was synthesized with conventional solid-state methods using stoichiometric amounts of strontium carbonate ( $\text{SrCO}_3$ , Sigma-Aldrich), iron oxide ( $\text{Fe}_2\text{O}_3$ , Sigma-Aldrich), cobalt oxide ( $\text{Co}_2\text{O}_3$ , Inframat Advanced Materials), and molybdenum oxide ( $\text{MoO}_3$ , Alfa-Aesar). The components were ball milled in ethanol for 24 hours, dried at 100 °C, and heated to 1100 °C for four hours.

To create fracture toughness test samples, SFCM powder was ball milled overnight with a mixture of 0.6 wt% polyethylene glycol 600, 1.8 wt% ethylene glycol, and 0.6 wt% glycerol in isopropyl alcohol. It was then dried at 100 °C, ground by mortar and pestle, pressed uniaxially into rectangular bars at 30 MPa, then isostatically pressed at 30 MPa. Sintering followed by heating to 1340 °C for four hours at 3 °C/min with a one hour hold at 400 °C to allow the binders to burn

out. This process achieved dense samples at 97% average theoretical density with no apparent flaws in the bars. Bars were then cut and sanded to final dimensions of 3 mm x 4 mm x 25 mm. The chevron notch was cut using the jig described by Jenkins, Chang and Okura following the ASTM procedure. [37, 38]

Tape casting was used to create test coupons of porous SFCM-GDC ASL and half-cells. Using ethanol as a solvent, SFCM-GDC was ball milled with polyvinyl butyral, benzyl butyl phthalate, 12  $\mu\text{m}$  poly(methyl methacrylate) (16 wt% with respect to SFCM-GDC), and Menhaden fish oil. The tape was cast to a thickness of 110  $\mu\text{m}$  on Mylar then laminated using a hot press to a final thickness of 660  $\mu\text{m}$ . Dense GDC was casted to 30  $\mu\text{m}$  and laminated to the top of the SFCM-GDC to create half-cells. Individual coupons were cut from the green tape, sintered at 1200 °C for four hours, with holds at low temperatures to burn out organic binder and pore former. The final thicknesses were measured to be 400  $\mu\text{m}$  for the SFCM-GDC ASL and  $\sim$ 20  $\mu\text{m}$  thick GDC electrolyte. Test coupons had their edges sanded to remove defects left from cutting, following ASTM standards. [39] Top and bottom surfaces were not sanded to preserve possible defects left from tape casting procedure, which would be representative of industrially manufactured SOFCs.

X-ray diffraction (XRD) was used to check and confirm phase purity of SFCM samples throughout the preparation and testing process. A Bruker D8 Advance with LynxEye was used with a Cu K $\alpha$  source. A step size of 0.02° was used with a dwell of 0.8 s to obtain diffraction patterns.

### 5.2.2 Conductivity

Direct current conductivity was measured using rectangular bars of SFCM and SFCM-GDC (2:1) composite. The samples were connected to a Keithley 2400 source meter by silver paste and wire. Using an in-house built reactor, the sample could be heated and the gas environment could be controlled. An initial measurement was taken after heating and 50 hours of exposure to 10% H<sub>2</sub> in N<sub>2</sub>, then the sample exposed cycled between air and reducing conditions over a period of 14 days.

### 5.2.3 Thermogravimetric Analysis (TGA)

Mass of samples during oxidation and reduction cycling was measured using a Cahn D200 microbalance. The samples were placed in a crucible suspended from a platinum wire attached to the microbalance and enclosed by an alumina tube inside a furnace. Heating control was achieved with a PID loop and temperature measurement done by a K-type thermocouple placed immediately below the sample inside the alumina tube. Gas flow was controlled at a constant 50 sccm by mass flow controllers. 21% O<sub>2</sub> in dry N<sub>2</sub> was used for the oxidizing condition while 3% H<sub>2</sub> in N<sub>2</sub> humidified with 3% H<sub>2</sub>O was used for the reducing conditions.

### 5.2.4 Mechanical Measurements

Measurements of mechanical properties were collected using a Tinius Olsen 10ST Universal Testing Machine equipped with a 250 N load cell. Experiments where any samples would be tested at elevated temperatures or under reducing

environments were conducted using a custom built three point flexural test fixture placed inside a gas-tight chamber and furnace. Otherwise, a fully-articulating four point flexural test fixture was used. Samples tested at ambient conditions were placed on the appropriate testing fixture and loaded until failure. For samples tested at elevated temperatures the sample was heated in the test chamber at  $10\text{ }^{\circ}\text{C min}^{-1}$ , allowed to equilibrate for 20 minutes, then tested. Samples to be reduced were placed in the chamber, heated and exposed to reducing gas for 18 hours before being tested.

#### 5.2.4.1 Flexural Strength

A loading rate of 0.2 mm/min was used for all strength measurements. Strength was calculated from the maximum force measured before failure according to Equation 5.2 or 5.3 depending on if the four point or three point fixture is used respectively, where  $\sigma$  is the strength,  $P$  is the maximum force,  $L$  is the span width of the test fixture,  $b$  is the width of the sample and  $d$  is the thickness of the sample. Equation 5.2 is for a fixture where the top span is 1/2 the width of the bottom span. [39]

$$\sigma = \frac{3PL}{4bd^2} \quad (5.2)$$

$$\sigma = \frac{3PL}{2bd^2} \quad (5.3)$$

#### 5.2.4.2 Chevron Notch Fracture Toughness

The fracture toughness of chevron notched samples were measured using a loading rate of 0.001 mm/min. Fracture toughness was calculated from the maximum force using Equation 5.4 or 5.5 for four point or three point fixtures. [38, 42]  $Y_{min}^*$  is

the shape factor as calculated by Equation 5.6,  $S_o$  and  $S_i$  are the outer and inner spans,  $B$  is the width of the sample,  $W$  is the height of the sample,  $a_0$  is the distance from the tip of the chevron notch to the bottom of the sample, and  $a_1$  is the average distance from the side of the chevron notch to the bottom of the sample. Each sample was measured after failure, but in this study the approximate values were  $S_o = 40mm$ ,  $S_i = 20mm$ ,  $B = 3.0mm$ ,  $W = 4.0mm$ ,  $a_0 = 0.80mm$ ,  $a_1 = 3.8mm$ . Fracture toughness was measured only under air at room temperature and up to 600 °C. Under reduction the fracture toughness bars would spontaneously fracture, preventing measurements under that condition.

$$K_{Ivb} = Y_{min}^* \left[ \frac{P[S_o - S_i]}{BW^{3/2}} \right] 10^{-6} \quad (5.4)$$

$$K_{Ivb} = Y_{min}^* \left[ \frac{P}{BW^{1/2}} \right] 10^{-6} \quad (5.5)$$

$$Y_{min}^* = \frac{0.38742 - 3.0919(a_0/W) + 4.2017(a_1/W) - 2.3127(a_1/W)^2 + 0.6379(a_1/W)^3}{1.0000 - 2.9686(a_0/W) + 3.5056(a_0/W)^2 - 2.1374(a_0/W)^3 + 0.0130(a_1/W)} \quad (5.6)$$

### 5.3 Results and Discussion

#### 5.3.1 Redox Cycling Stability

SFCM has a high initial conductivity of 35 S/cm but decreases after 3 cycles to 19 S/cm and again at 9 cycles, shown in Figure 5.1a. The addition of GDC to create a SFCM-GDC composite decreases the initial conductivity to 15 S/cm. At 4 cycles, SFCM-GDC decreases conductivity and stabilizes to 8 S/cm for 19 cycles. The addition of the GDC improved the redox cycling stability by providing a very

stable, contiguous framework for the SFCM. [14, 35, 85]

Figure 5.1b shows the mass loss of SFCM-GDC as it is reduced in 3% humidified H<sub>2</sub>. For comparison, another popular anode material, nickel oxide GDC, is plotted along with it. The reduction of SFCM-GDC results in a less than 1% reduction of mass from the formation of oxygen vacancies in the SFCM and GDC, and it reaches steady state in under two hours. NiO-GDC on the other hand loses a large amount of mass from the reduction and phase change of NiO to Ni metal taking over 30 hours to reach steady state.

Further cycling of SFCM in the thermogravimetric analyzer (TGA) was performed and results are given in Figure 5.2 with 5.2a showing the mass loss of SFCM with time as it is cycled between air and hydrogen and 5.2b being a summary of the total mass changes that occur with each cycle. With each cycle, less than 1% total mass change is observed. Reduction occurs over a time period of five hours while oxidation happens at a faster rate, approximately one hour. Fitting the reduction and oxidation to exponential functions gives a biexponential with decay rates of 0.438 and 27.89 for reduction and an oxidation rate of 2.90. Previous experiments have shown that SFCM generates an impurity phase of Sr<sub>2</sub>Co<sub>1.2</sub>Mo<sub>0.8</sub>O<sub>6</sub> under ambient and oxidizing conditions. [89] This impurity phase does not contribute to the gain or loss of oxygen as seen in the TGA. Sr<sub>2</sub>Co<sub>1.2</sub>Mo<sub>0.8</sub>O<sub>6</sub> has a cubic structure compared to SFCM's tetragonal structure, leading to additional stress and strain created by its generation impacting the mechanical and electrical properties between oxidizing and reducing environments.

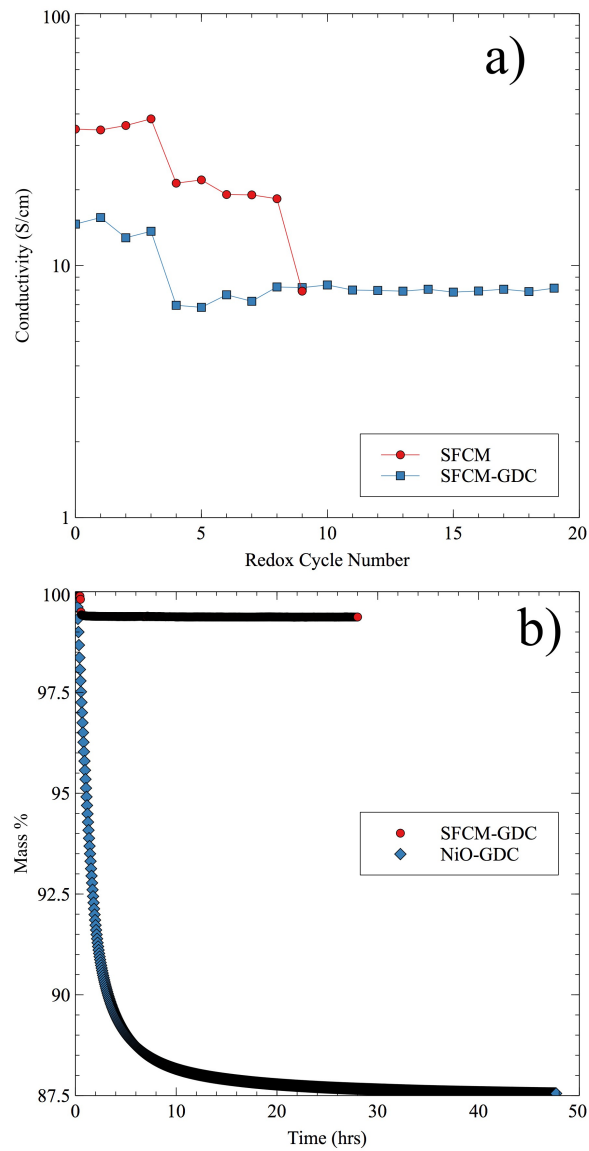


Figure 5.1: a) DC conductivity of SFCM and SFCM-GDC after cycling at 650 °C between 10% H<sub>2</sub> in N<sub>2</sub> and air. b) Mass loss of SFCM-GDC and NiO-GDC during reduction in 3% H<sub>2</sub>/3% H<sub>2</sub>O in N<sub>2</sub> at 650 °C.

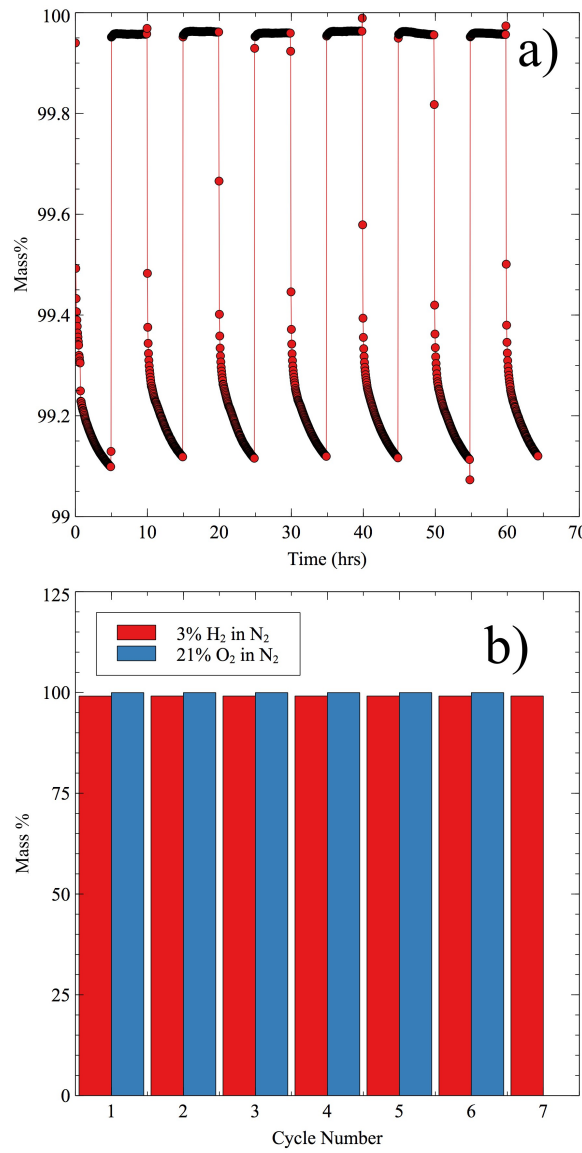


Figure 5.2: Mass changes of SFCM during cycling between 21% O<sub>2</sub> and 3% H<sub>2</sub>/3% H<sub>2</sub>O in N<sub>2</sub> at 600 °C. Each exposure was 5 hours. a) Percent mass change with time as the gas is switched back and forth. b) Summary of maximum and minimum changes with each cycle.

### 5.3.2 Fracture Toughness

Fracture toughness was found to be  $(0.124 \pm 0.023) \text{ MPa}\sqrt{\text{m}}$  at room temperature, increasing with temperature up to  $600^\circ\text{C}$ , as shown in Figure 5.3a. From room temperature to  $500^\circ\text{C}$ , the rate of increase in  $K_{\text{Ic}}$  is low at  $4.3 \times 10^{-5} \text{ MPa}\sqrt{\text{m}}/\text{°C}$ . From  $500^\circ\text{C}$  to  $600^\circ\text{C}$  the fracture toughness increases by 90%. The increase in fracture toughness is a result of the thermal expansion of the material. During process of creating the bar, the sample was cooled from  $1340^\circ\text{C}$  to room temperature. This cooling and associated contraction induces stresses in the bar sample, which combine with the stresses added during testing to fracture the sample. As the sample is heated, the residual stresses are relaxed, increasing the amount of stress which must be applied externally to cause the bar to fracture. Any change in fracture toughness due to the weakening of bonds is masked by this effect. The increase in fracture toughness from  $500^\circ\text{C}$  to  $600^\circ\text{C}$  matches the temperature where the rate of thermal expansion also increases, as shown in Figure 5.3b.

Figure 5.3b also presents the thermal expansion of GDC and a SFCM-GDC composite. At temperatures below  $550^\circ\text{C}$  the expansion of SFCM-GDC matches that of pure SFCM, greater than that of pure GDC. Above  $550^\circ\text{C}$ , the rate of expansion slows in comparison to SFCM and matches the rate of expansion for GDC. Thus, below  $550^\circ\text{C}$ , SFCM-GDC expands the same as SFCM and above  $550^\circ\text{C}$  it expands the same as GDC. We would then expect that SFCM-GDC composites have the same increase in fracture toughness as SFCM up to  $550^\circ\text{C}$  due expansion and relaxation of intrinsic stresses, but not further increase the rate above  $500^\circ\text{C}$ , as SFCM does.

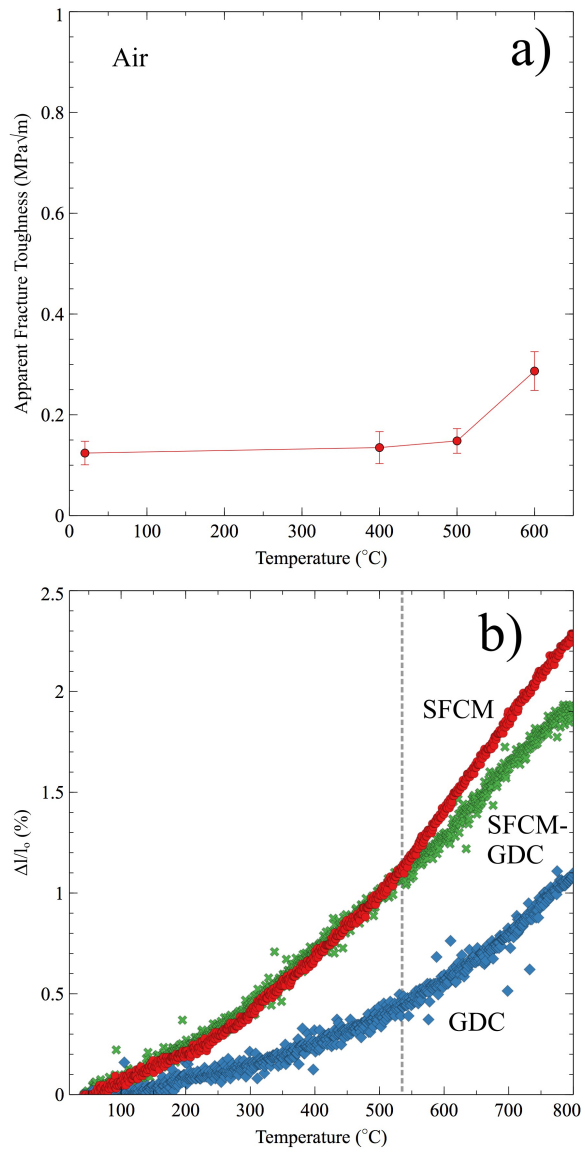


Figure 5.3: a) Fracture toughness of SFCM from 20  $^{\circ}\text{C}$  to 600  $^{\circ}\text{C}$ . b) Thermal expansion of SFCM, GDC, and SFCM-GDC.

### 5.3.3 Half-cell Strength of Anode-Supported SOFCs at Operating Conditions

Figure 5.4 gives box plots of the results of three point flexural testing of SFCM-GDC/GDC half-cells, and Table 5.1 summaries the strengths. The circles on the right of 5.4 represent the results of a Student's t-test, to determine if the means of the different data sets are the same. The more the circles overlap the more similar the data sets are. In this case, there is no overlap between circles at the 95% confidence interval, highlighting that the strengths tested at each condition are unique from each other.

At ambient conditions the strength of the half-cells was measured to be 57.7 MPa. Upon heating, the strength increases to 74.2 MPa. This result correlates with the increase in fracture toughness discussed earlier, which is expected based on Equation 5.1. Another contributing factor to the increase in strength is the effect thermal expansion has on pre-existing cracks and flaws. Any expansion of the material helps push closed a surface crack which would lead to failure, decreasing its size and increasing the stress that would be required to cause that crack to open and propagate.

Upon reduction of the half-cell at 600 °C, the fracture strength decreases, below that of the ambient strength, to 39.9 MPa. During this transition to reducing conditions, the impurity phase reduces back into SFCM, causing a decrease in mechanical properties from the change in lattice parameters. Additionally, bulk mechanical properties have changed as SFCM becomes pure phase, oxygen vacancies

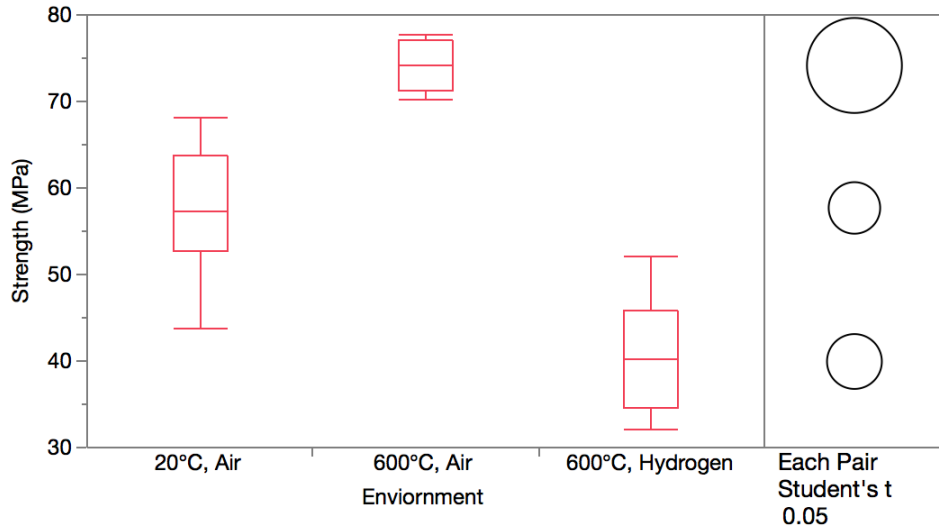


Figure 5.4: Flexural strengths of half-cell coupons made from SFCM-GDC anode with GDC electrolyte tested at 20 °C in air, 600 °C in air, and 600 °C in 5% H<sub>2</sub>.

are generated and B-site transition metals are reduced.

Weibull analysis was performed to compare the distribution of flaws between the ambient tested half-cells and the in-situ reduced half-cells. Figure 5.5 displays the fitting of Weibull distributions to the flexural strength of half-cell coupons tested at ambient conditions and during reduction at 600 °C. Table 5.2 summarizes the fitting parameter for the Weibull modulus with 95% confidence intervals using the maximum-likelihood method. Between the two conditions, there is an appreciable change in the Weibull modulus of the two samples. The Weibull modulus increases decreases from 10.4 at ambient conditions to 7.29 when at reducing conditions. This change in Weibull modulus is the result of the reduction of SFCM impurities changing the bulk properties of the material combined with distribution of flaws becoming

Table 5.1: Summary of strengths for SFCM-GDC/GDC half-cells at different environments

Temperature (°C)	Atmosphere	Number	Mean (MPa)	Std Dev (MPa)
20	Air	17	57.7	6.71
600	Air	5	74.2	2.98
600	5% H <sub>2</sub>	14	39.9	5.89

wider, creating more variability between flaws.

To confirm any changes in flaw distribution, fractography would need to be performed on every sample, identifying the flaw, but this is not possible due to the porous nature of the fracture surface which obscures the fracture origin. Scanning electron microscopy was performed on fracture surfaces and epoxy filled samples from each condition to look for any microstructural changes. Figure 5.6 shows the epoxy filled and polished samples with no discernible difference between samples. No difference is observed because the likely cause of failure, microcracks, would exist along grain boundaries and are obscured by the grain boundaries and pores. [21, 90]

### 5.3.4 Strength of Anode Support Layer After Redox Cycling

To understand how redox cycling as the result of long term use affects the strength of SFCM based SOFCs, SFCM-GDC ASL test coupons were cycled for 10 times between nitrogen and 10% H<sub>2</sub> environments. Figure 5.7 shows the strength

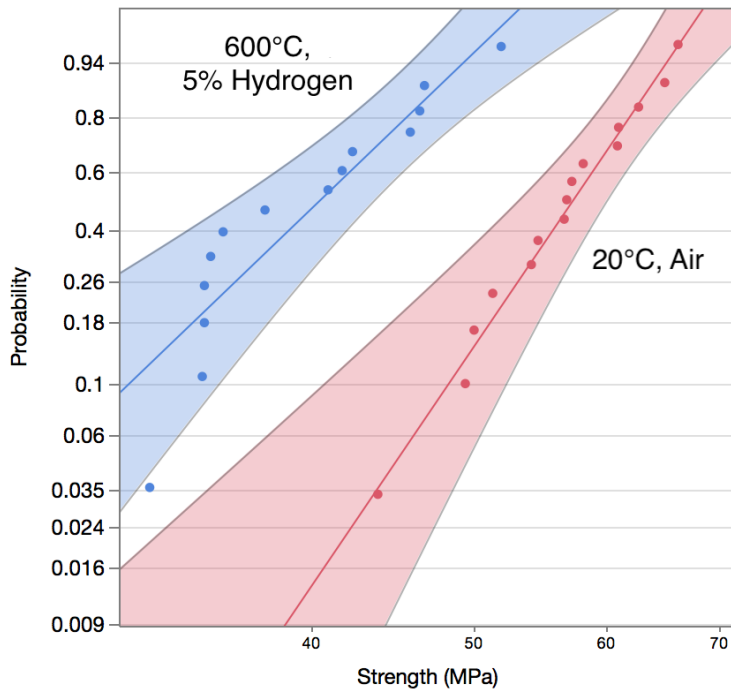


Figure 5.5: Fitted Weibull distributions of SFCM-GDC/GDC half-cells at different environments, plotted linearly with 95% confidence intervals shaded.

Table 5.2: Summary of Weibull fitting parameters (characteristic strength and Weibull modulus) for SFCM-GDC/GDC half-cells at different environments

Temp. (°C)	Environment	Cha.	$\alpha$	$\alpha$	Weibull	$\beta$	$\beta$
		Strength ( $\alpha$ , MPa)	Lower CI	Upper CI	Modulus ( $\beta$ )	Lower CI	Upper CI
20	Air	60.6	57.4	63.6	10.4	6.89	14.7
600	Hydrogen	42.5	39.2	45.8	7.29	4.79	10.3

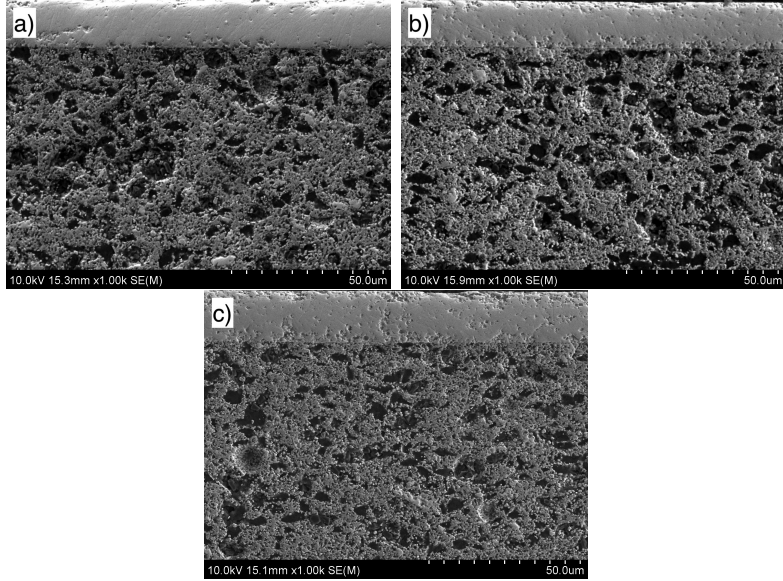


Figure 5.6: Scanning electron microscope images of epoxy filled and polished SFCM-GDC/GDC half-cell cross sections tested at a) 20 °C in air, b) 600 °C in air and c) 600 °C in 5% H<sub>2</sub>.

and modulus from the samples which were not cycled (0 cycles) and those cycled 10 times, tested using a four-point bend at ambient conditions. Table 5.3 summarizes the means and standard deviations of the test results. The overlapping Student's t circles in Figure 5.7b demonstrate that cycling did not significantly change the elastic modulus of the samples, while the strength did significantly decrease. This is the result of changes in microstructural flaws, rather than the change of an intrinsic material property.

The strengths of the cycled and un-cycled cells were fitted to Weibull distributions to observe how flaw distributions changed with redox cycling. Figure 5.8 presents the fitted data and distributions and Table 5.4 summarizes the fit parameters of the Weibull modulus with 95% confidence intervals. The Weibull moduli between

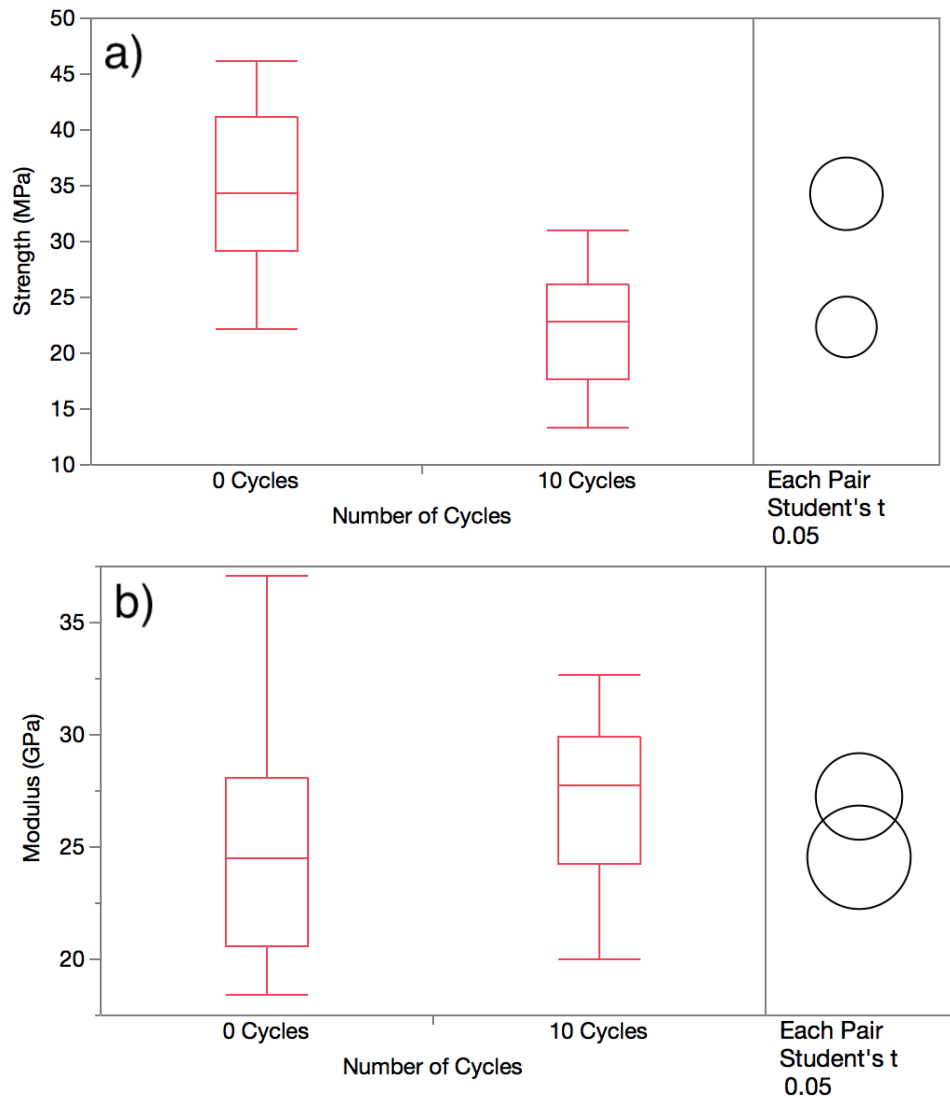


Figure 5.7: Results of four point bend test at ambient conditions of SFCM-GDC ASL with a) strength and b) modulus for samples before any cycling and after 10 redox cycles between 10% H<sub>2</sub> and N<sub>2</sub>.

Table 5.3: Summary of Cycled SFCM-GDC ASL Mechanical Properties

Number of Cycles	Number	Mean	Modulus	Mean	Strength
		Modulus	Std Dev	Strength	Std Dev
		(GPa)	(GPa)	(MPa)	(MPa)
0	14	24.5	5.01	34.3	7.23
10	20	27.3	3.60	22.4	4.94

the two data sets are very similar, indicating that the flaw distribution is the same between them. The decrease in characteristic strength is then due to the growth of flaws with cycling. SEM images in Figure 5.9 are of a sample which had not been cycled (a) and one which had been cycled 10 times (b) after being epoxy filled and polished. The sample which had been cycled 10 times has a greater number of pores at larger sizes compared to the un-cycled sample. This indicates that the finer microstructure of the pores is susceptible to changes during redox cycling due to chemical expansion, but the larger flaws which lead to complete cell failure do not change as the result of redox cycling. [91]

## 5.4 Conclusions

In this work the mechanical properties of SFCM and SFCM-GDC structures are characterized as the environment is changed from ambient to the working conditions of SOFCs and with redox cycling. The electrical conductivity of SFCM-GDC is stable up to 19 cycles due to the reversibility and phase stability of SFCM-GDC

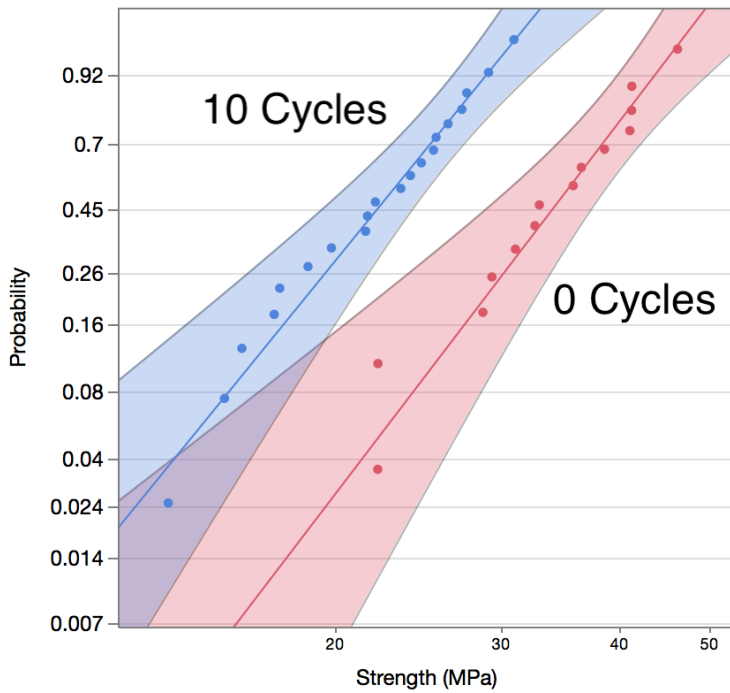


Figure 5.8: Fitted Weibull distributions of SFCM-GDC ASL before any cycling and after 10 redox cycles between 10% H<sub>2</sub> and N<sub>2</sub>, plotted linearly with 95% confidence intervals shaded

Table 5.4: Summary of Weibull Fit Parameters (characteristic strength and Weibull modulus) for Cycled SFCM-GDC ASL

Number of Cycles	Char. Strength ( $\alpha$ , MPa)	$\alpha$		Weibull Modulus ( $\beta$ )		$\beta$	
		CI Lower	CI Upper	CI Lower	CI Upper	CI Lower	CI Upper
0	37.1	33.7	40.8	5.75	4.06	9.85	
10	24.3	22.3	26.5	5.39	4.00	8.28	

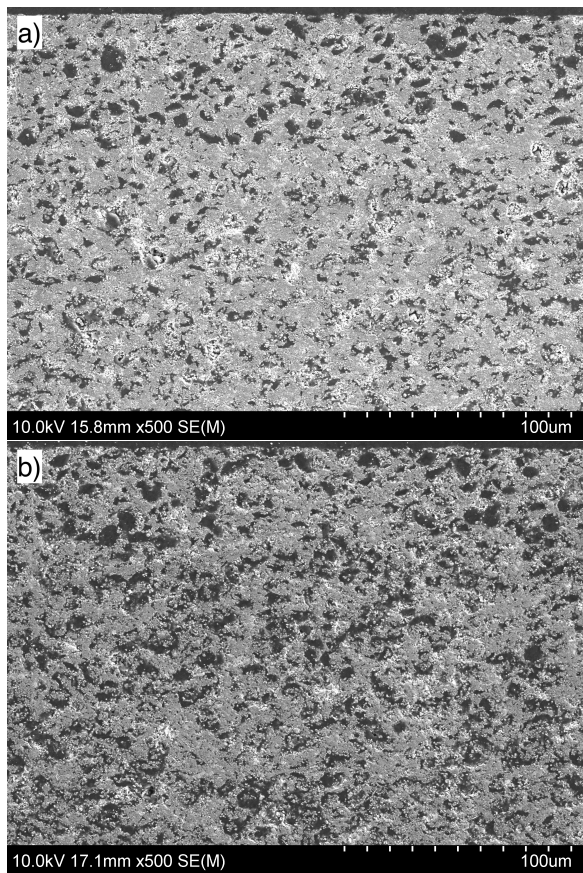


Figure 5.9: Scanning electron microscope images of epoxy filled and polished SFCM-GDC ASL cross sections tested a) before any cycling, b) after 10 cycles between 10% H<sub>2</sub> and N<sub>2</sub>.

in the environment range. The fracture toughness of SFCM was found to be  $(0.124 \pm 0.023) \text{ MPa}\sqrt{\text{m}}$  at room temperature and increases with temperature, due to relaxation of residual stresses. The flexural strength of SFCM-GDC/GDC half-cells increases by 23.9% upon heating from room temperature to 600 °C. This is due to thermal expansion pushing cracks closed during heating, requiring additional stress to propagate surface cracks and the increase in fracture toughness. Once exposed to reducing conditions, the flexural strength decreases by 29.4% of the original strength, as impurities reduce and SFCM and GDC generate oxygen vacancies. Reduction was shown to increase the size and variability of the distribution of flaws which lead to failure. Redox cycling led to the uniform increase in critical flaw size and changed the fine microstructural porosity, decreasing strength from 34.3 MPa to 22.4 MPa.

These findings show that SFCM, when combined with GDC, make a suitable anode material for SOFCs. SFCM-GDC is a stable material system, both in terms of conductivity and mechanically, with redox cycling. Reduction does increase the likelihood of failure by decreasing characteristic strength and the distribution of flaws, but repeated cycling only decreases characteristic strength and does not change the Weibull modulus.

## Chapter 6: Conclusions

This piece will talk about SOFCs. This is mostly because I work on SOFCs.  
This is to show Mimi git. [92]

## Appendix A: Statistics

### A.1 Student's t-test

### A.2 Weibull Statistics

## Appendix B: TGA Manual

### B.1 Theory of Operation

Thermogravimetry works on the principle of measuring small changes in mass as the environment changes. Changes in environment can come from

### B.2 Mass Measurement

The TGA uses a Cahn D200 microbalance for the mass sensing capability.

### B.3 Gas Delivery

MKS Controllers are used.

### B.4 pO<sub>2</sub> Measurement

Home built YSZ sensor.

### B.5 Controls

Lab view on the computer.

## B.6 Interfacing with other devices

Can be plumbed up to mass spec.

## Appendix C: Code

### C.1 Arduino PID Relay Furnace Controller with Serial Connectivity

The purpose of this Arduino sketch is to power a heating furnace (controlled by a relay), with PID controls. In addition serial communications are added to monitor, log, and interact with the controller.

#### C.1.1 Hardware and other libraries

This was built to be used on a Arduino Uno R3, but should be easily run on a variety of different boards. For temperature sensing, an [Adafruit MAX31856](#) is used with the [library](#) from them. Also used is the PID controller [library by br3ttb](#). All I have really done is put the two together with the ability to communicate over serial.

#### C.1.2 Variables

Here are a list of variables for things you may want to change based on your setup.

- RelayPin: The physical pin your relay is connected to.
- Adafruit\_MAX31856(CS, DI, DO, CLK): Pins for your MAX31856

- WindowSize: Length of on/off cycle, needed to account for AC power
- printdelay: Delay time in milliseconds for printout on serial
- MaxOP: Maximum operating power, used to extend life of elements
- myPID(&Input, &Output, &workingSet,P,I,D, DIRECT): PID need to be adjusted for your setup. If inverse behavior is experienced (e.g. heats when it should cool) switch DIRECT.
- workingSet and Setpoint: Initial setpoint for power on
- ramrate: Sets a ramp rate for the working setpoint. Measured in milliseconds for 1C change.

### C.1.3 Serial communications

Baud rate is set to 9600. Output is tab delimited of Setpoint, Working Setpoint, Thermocouple Temperature, and Output Power. To change set point, send a new number over serial and press return. You may have to adjust your serial monitor to send \n as end of line.

```

1 #include <Adafruit_MAX31856.h> //loads library for thermocouple reader
2 #include <PID_v1.h> //loads PID library
3 #include <RunningAverage.h> //loads class for Running Average
   ↵ calculations
4 #define RelayPin 2 //set pin number which is connected to power relay
   ↵ for device
5

```

```

6 const byte numChars = 32;

7 char receivedChars[numChars]; // an array to store the received data

8

9 boolean newData = false; //trigger to determine if data needs to be
    ↵ read

10

11 Adafruit_MAX31856 max = Adafruit_MAX31856(4, 5, 6, 7); // Software SPI,
    ↵ Pin number for: CS, DI, DO, CLK

12

13 //Define Variables

14 double workingSet, Setpoint, Input, Output;

15 int WindowSize = 1000; //Length of cycle for power on/off

16 unsigned long prevprintMillis = 0;

17 const long printdelay = 5000; //delay amount before printing via serial

18 unsigned long windowStartTime;

19 unsigned long prevRampTimer = 0;

20 unsigned long MaxOP = .95; // Max Operating Power

21

22 RunningAverage myRA(10); //Set up running average with # of
    ↵ measurements

23

24 PID myPID(&Input, &Output, &workingSet, 250, 50, 8, DIRECT); //Specify the
    ↵ links and initial tuning parameters

25

26 void setup() {
27     pinMode(RelayPin, OUTPUT); //define RelayPin as an output
28

```

```

29 //staring serial communications
30 Serial.begin(9600);
31 Serial.println("PID Controller Output");
32 Serial.println("Setpoint\t Working SP\t TC Temp\t Output");//tab
   ↪ delimited for logging
33
34 //setup for thermocouple reader
35 max.begin();
36 max.setThermocoupleType(MAX31856_TCTYPE_K);//change type if needed
37
38 windowStartTime = millis(); //start timer for duty cycle window
39
40 myRA.clear(); // explicitly start clean
41
42 //initialize the variables we're linked to
43 workingSet = 20;
44 Setpoint = 20;
45
46 myPID.SetOutputLimits(0, MaxOP * WindowSize); //tell the PID to range
   ↪ between 0 and the full window size
47 myPID.SetMode(AUTOMATIC); //turn the PID on
48
49 }
50
51 //fuction to recieve data via serial and process when endmarker is
   ↪ received
52 void recvWithEndMarker() {

```

```

53 static byte ndx = 0;
54
55 char endMarker = '\n'; //define line endmarker for client
56
57 // if (Serial.available() > 0) {
58
59     while (Serial.available() > 0 && newData == false) {
60
61         rc = Serial.read();
62
63         if (rc != endMarker) {
64
65             receivedChars[ndx] = rc;
66
67             ndx++;
68
69             if (ndx >= numChars) {
70
71                 ndx = numChars - 1;
72
73             }
74
75
76             else {
77
78                 receivedChars[ndx] = '\0'; // terminate the string
79
80                 ndx = 0;
81
82                 newData = true;
83
84             }
85
86         }
87
88     }
89
90
91     //Function to repeat new setpoint for confirmation
92
93     void showNewData() {
94
95         if (newData == true) {
96
97             String recievedString = String(receivedChars);

```

```

80 Serial.print("Setpoint changed to ... ");
81 Serial.println(recievedString.toFloat());
82 Setpoint = recievedString.toFloat();
83 newData = false;
84 }
85 }
86
87 void loop() {
88 recvWithEndMarker(); //check for new setpoint
89 showNewData(); //sets new setpoint and displays it
90
91 // Input = max.readThermocoupleTemperature(); //read thermocouple
92
93 myRA.addValue(max.readThermocoupleTemperature());
94
95 Input = myRA.getAverage();
96
97 myPID.Compute(); //calculate PID output
98
99 //print delay for serial output so not to flood logs
100 unsigned long printMillis = millis();
101 if (printMillis - prevprintMillis >= printdelay) {
102     prevprintMillis = printMillis;
103     Serial.print(Setpoint); Serial.print("\t"); Serial.print(workingSet);
104     → Serial.print("\t"); Serial.print(max.readThermocoupleTemperature
105     → ()); Serial.print("\t"); Serial.println(Output/WindowSize*100);
106 }

```

```

105
106 //turn the output pin on/off based on pid output
107 if( millis() - windowStartTime >=WindowSize)
108 { //time to shift the Relay Window
109     windowStartTime += WindowSize;
110 }
111 if( Output < millis() - windowStartTime) digitalWrite(RelayPin,LOW); //  

    ↳ HIGH and LOW set to default off
112 else digitalWrite(RelayPin,HIGH);
113
114 //sets ramp rate functionality
115 unsigned long ramptimer = millis();
116 unsigned long ramprate = 6000;//milliseconds for 1C change
117 if( workingSet != Setpoint)
118 {
119     if( ramptimer - prevRampTimer >= ramprate && workingSet < Setpoint)
120     {
121         workingSet++;
122         prevRampTimer = ramptimer;
123     }
124     if( ramptimer - prevRampTimer >= ramprate && workingSet > Setpoint)
125     {
126         workingSet--;
127         prevRampTimer = ramptimer;
128     }
129 }
130 }
```

## Bibliography

- [1] U.S. Energy Information Administration. World energy demand and economic outlook. Technical Report May 2016, U.S. Energy Information Administration, 2016.
- [2] Stephen G Osborn, Avner Vengosh, Nathaniel R Warner, and Robert B Jackson. Methane contamination of drinking water accompanying gas-well drilling and hydraulic fracturing. *Proceedings of the National Academy of Sciences of the United States of America*, 108(20):8172–6, 2011.
- [3] Avner Vengosh, Robert B Jackson, Nathaniel Warner, Thomas H Darrah, and Andrew Kondash. A Critical Review of the Risks to Water Resources from Shale Gas Development and Hydraulic Fracturing in the United States. *Environmental Science & Technology*, 16(4):6838, 2014.
- [4] Susan Solomon, Gian-Kasper Plattner, Reto Knutti, and Pierre Friedlingstein. Irreversible climate change due to carbon dioxide emissions. *Proceedings of the National Academy of Sciences of the United States of America*, 106(6):1704–9, 2009.
- [5] J Hansen, D Johnson, A Lacis, S Lebedeff, P Lee, D Rind, and G Russell. Climate impact of increasing atmospheric carbon dioxide. *Science*, 213(4511):957–966, 1981.
- [6] U.S. Environmental Protection Agency. Inventory of U.S. Greenhouse Gas Emissions and Sinks: 1990 - 2015. Technical report, U.S. Environmental Protection Agency, 2017.
- [7] E. D. Wachsman and K. T. Lee. Lowering the Temperature of Solid Oxide Fuel Cells. *Science*, 334(6058):935–939, 2011.
- [8] Robert H. Lasseter and Paolo Paigi. Microgrid: A conceptual solution. In *IEEE Power Electronics Specialists Conference*, volume 6, pages 4285–4290, 2004.
- [9] Seungdoo Park, John M. Vohs, and Raymond J. Gorte. Direct oxidation of hydrocarbons in a solid-oxide fuel cell. *Nature*, 404(6775):265–267, 2000.

- [10] Nguyen Q. Minh. Solid oxide fuel cell technology - Features and applications. *Solid State Ionics*, 174(1-4):271–277, 2004.
- [11] Wikimedia Commons. Solid Oxide Fuel Cell Diagram.
- [12] James Larminie and Andrew Dicks. *Fuel Cell Systems Explained*, volume 93. 2001.
- [13] I. Pilatowsky, R.J. Romero, C.A. Isaza, S.A. Gamboa, P.J. Sebastian, and W. Rivera. Thermodynamics of Fuel Cells. *Cogeneration Fuel Cell- Sorption Air Conditioning Systems*, pages 25–36, 2011.
- [14] Mogens Mogensen, Nigel M. Sammes, and Geoff A. Tompsett. Physical, chemical and electrochemical properties of pure and doped ceria. *Solid State Ionics*, 129(1):63–94, 2000.
- [15] Mikko Pihlatie, Andreas Kaiser, and Mogens Mogensen. Mechanical properties of NiO/Ni-YSZ composites depending on temperature, porosity and redox cycling. *Journal of the European Ceramic Society*, 29(9):1657–1664, 2009.
- [16] J. Laurencin, G. Delette, O. Sicardy, S. Rosini, and F. Lefebvre-Joud. Impact of 'redox' cycles on performances of solid oxide fuel cells: Case of the electrolyte supported cells. *Journal of Power Sources*, 195(9):2747–2753, 2010.
- [17] Jiang Liu, Brian D Madsen, Zhiqiang Ji, and Scott A Barnett. A Fuel-Flexible Ceramic-Based Anode for Solid Oxide Fuel Cells. *Electrochemical and Solid-State Letters*, 5(May 2012):122–124, 2002.
- [18] Sossina M. Haile. Fuel cell materials and components. *Acta Materialia*, 51(19):5981–6000, 2003.
- [19] Harumi Yokokawa, Hengyong Tu, Boris Iwanschitz, and Andreas Mai. Fundamental mechanisms limiting solid oxide fuel cell durability. *Journal of Power Sources*, 182(2):400–412, 2008.
- [20] F. Gutierrez-Mora, J. M. Ralph, and J. L. Routbort. High-temperature mechanical properties of anode-supported bilayers. *Solid State Ionics*, 149(3-4):177–184, 2002.
- [21] Ji Haeng Yu, Gun Woo Park, Shiwoo Lee, and Sang Kuk Woo. Microstructural effects on the electrical and mechanical properties of Ni-YSZ cermet for SOFC anode. *Journal of Power Sources*, 163(2):926–932, 2007.
- [22] William D. Callister and David G. Rethwisch. Influence of Porosity. *Materials Science and Engineering: An Introduction*, pages 373–381, 2014.
- [23] Michel Barsoum. Processing and Surface Flaws. In *Fundamentals of Ceramics*, volume 2174, pages 374–381. 2003.

- [24] John B. Goodenough and Yun Hui Huang. Alternative anode materials for solid oxide fuel cells. *Journal of Power Sources*, 173(1):1–10, 2007.
- [25] Shaowu Zha, Philip Tsang, Zhe Cheng, and Meilin Liu. Electrical properties and sulfur tolerance of La<sub>0.75</sub>Sr<sub>0.25</sub>Cr<sub>1-x</sub>Mn<sub>x</sub>O<sub>3</sub> under anodic conditions. *Journal of Solid State Chemistry*, 178(6):1844–1850, 2005.
- [26] S. Primdahl, J. R. Hansen, L. Grahl-Madsen, and P. H. Larsen. Sr-Doped LaCrO<sub>3</sub> Anode for Solid Oxide Fuel Cells. *Journal of The Electrochemical Society*, 148(1):A74, 2001.
- [27] A. Mohammed Hussain, Jens V.T. Høgh, Wei Zhang, Peter Blennow, Nikolaos Bonanos, and Bernard A. Boukamp. Effective improvement of interface modified strontium titanate based solid oxide fuel cell anodes by infiltration with nano-sized palladium and gadolinium-doped cerium oxide. *Electrochimica Acta*, 113:635–643, 2013.
- [28] A. Mohammed Hussain, Jens V.T. Høgh, Torben Jacobsen, and Nikolaos Bonanos. Nickel-ceria infiltrated Nb-doped SrTiO<sub>3</sub>for low temperature SOFC anodes and analysis on gas diffusion impedance. *International Journal of Hydrogen Energy*, 37(5):4309–4318, 2012.
- [29] A. Mohammed Hussain, Ke-Ji Pan, Ian A. Robinson, Thomas Hays, and Eric D. Wachsman. Stannate-Based Ceramic Oxide as Anode Materials for Oxide-Ion Conducting Low-Temperature Solid Oxide Fuel Cells. *Journal of The Electrochemical Society*, 163(10):F1198–F1205, 2016.
- [30] Yun-Hui Huang, Ronald I Dass, Zheng-Liang Xing, and John B Goodenough. Double Perovskites as Anode Materials for Solid-Oxide Fuel Cells. *Science*, 2(April):254–258, 2006.
- [31] S.H Chan, K.a Khor, and Z.T Xia. A complete polarization model of a solid oxide fuel cell and its sensitivity to the change of cell component thickness. *Journal of Power Sources*, 93(1-2):130–140, 2001.
- [32] Felix Fleischhauer, Andreas Tiefenauer, Thomas Graule, Robert Danzer, Andreas Mai, and Jakob Kuebler. Failure analysis of electrolyte-supported solid oxide fuel cells. *Journal of Power Sources*, 258:382–390, 2014.
- [33] J. Laurencin, G. Delette, F. Lefebvre-Joud, and M. Dupeux. A numerical tool to estimate SOFC mechanical degradation: Case of the planar cell configuration. *Journal of the European Ceramic Society*, 28(9):1857–1869, 2008.
- [34] S.R. Bishop, D. Marrocchelli, C. Chatzichristodoulou, N.H. Perry, M.B. Mogensen, H.L. Tuller, and E.D. Wachsman. Chemical Expansion: Implications for Electrochemical Energy Storage and Conversion Devices. *Annual Review of Materials Research*, 44(1):205–239, 2014.

- [35] Keith L. Duncan, Yanli Wang, Sean R. Bishop, Fereshteh Ebrahimi, and Eric D. Wachsman. Role of point defects in the physical properties of fluorite oxides. *Journal of the American Ceramic Society*, 89(10):3162–3166, 2006.
- [36] Yanli Wang, Keith Duncan, Eric D. Wachsman, and Fereshteh Ebrahimi. The effect of oxygen vacancy concentration on the elastic modulus of fluorite-structured oxides. *Solid State Ionics*, 178(1-2):53–58, 2007.
- [37] M. Jenkins, T. Chang, and A. Okura. A Simple Maching Jig for Chevron-notched Specimens. *Experimental Techniques*, 12(8):20–22, 1988.
- [38] ASTM Standard C1421. Standard Test Methods for Determination of Fracture Toughness of Advanced Ceramics at Ambient Temperature. *ASTM International*, pages 1–33, 2016.
- [39] ASTM Standard C1221. Standard Test Method for Flexural Strength of Advanced Ceramics at Elevated Temperatures. *ASTM International*, 11(Reapproved 2008):1–16, 2013.
- [40] Brian H Toby and Robert B. Von Dreele. GSAS-II: The genesis of a modern open-source all purpose crystallography software package. *Journal of Applied Crystallography*, 46(2):544–549, 2013.
- [41] Koichi Momma and Fujio Izumi. VESTA 3 for three-dimensional visualization of crystal, volumetric and morphology data. *Journal of Applied Crystallography*, 44(6):1272–1276, 2011.
- [42] Shang Xian Wu. Fracture toughness determination of bearing steel using chevron-notch three point bend specimen. *Engineering Fracture Mechanics*, 19(2):221–232, 1984.
- [43] Jeongpill Ki and Daejong Kim. Computational model to predict thermal dynamics of planar solid oxide fuel cell stack during start-up process. *Journal of Power Sources*, 195(10):3186–3200, 2010.
- [44] J. J. Roa, M. A. Laguna-Bercero, A. Larrea, V. M. Orera, and M. Segarra. Mechanical properties of highly textured porous Ni-YSZ and Co-YSZ cermets produced from directionally solidified eutectics. *Ceramics International*, 37(8):3123–3131, 2011.
- [45] Arata Nakajo, Jakob Kuebler, Antonin Faes, Ulrich F. Vogt, Hans Jürgen Schindler, Lieh Kwang Chiang, Stefano Modena, Jan Van Herle, and Thomas Hocker. Compilation of mechanical properties for the structural analysis of solid oxide fuel cell stacks. Constitutive materials of anode-supported cells. *Ceramics International*, 38(5):3907–3927, 2012.
- [46] Zhen Yan Deng, Jihong She, Yoshiaki Inagaki, Jian Feng Yang, Tatsuki Ohji, and Yoshihisa Tanaka. Reinforcement by crack-tip blunting in porous ceramics. *Journal of the European Ceramic Society*, 24(7):2055–2059, 2004.

- [47] Milan Ambrozic and Tomaz Kosmac. Optimization of the bend strength of flat-layered alumina-zirconia composites. *Journal of the American Ceramic Society*, 90(5):1545–1550, 2007.
- [48] Akio Yonezu and Xi Chen. Micro-scale damage characterization in porous ceramics by an acoustic emission technique. *Ceramics International*, 40(7 PART A):9859–9866, 2014.
- [49] S. Meille, M. Lombardi, J. Chevalier, and L. Montanaro. Mechanical properties of porous ceramics in compression: On the transition between elastic, brittle, and cellular behavior. *Journal of the European Ceramic Society*, 32(15):3959–3967, 2012.
- [50] Pulin Nie, Heping Lv, Tao Zhou, Xun Cai, and Paul K. Chu. Interfacial adhesion measurement of a ceramic coating on metal substrate. *Journal of Coatings Technology Research*, 7(3):391–398, 2010.
- [51] C Olagnon. Determination of the fracture mechanical parameters of porous ceramics from microstructure parameters measured by quantitative image analysis. *Journal of Materials Science*, 4(1):4081–4088, 1999.
- [52] B. F. Sorensen and A. Horsewell. Crack Growth along Interfaces in Porous Ceramic Layers. *Journal of the American Ceramic Society*, 84(9):2051–59, 2001.
- [53] S. M. Barinov, V. F. Ponomarev, and V. Ya. Shevchenko. Effect of Hot Isostatic Pressing on the Mechanical Properties of Aluminum Oxide Ceramics. *Refractories and Industrial Ceramics*, 38(1-2):9–12, 1997.
- [54] K Yasuda, K Uemura, and T Shiota. Sintering and mechanical properties of gadolinium-doped ceria ceramics. *Journal of Physics: Conference Series*, 339(1):012006, 2012.
- [55] Roy W. Rice. *Porosity of Ceramics: Properties and Applications*. Marcel Dekker. Inc., New York, 1998.
- [56] Rodger W. Davidge and Anthony G. Evans. The Strength of Ceramics. *Materials Science and Engineering*, (6):281–298, 1970.
- [57] Sophie Giraud and Jérôme Canel. Young's modulus of some SOFCs materials as a function of temperature. *Journal of the European Ceramic Society*, 28(1):77–83, 2008.
- [58] Barry Carter and Grant Norton. *Ceramic Materials Science and Engineering*. 2007.
- [59] Oldřich Ševeček, Michal Kotoul, Dominique Leguillon, Eric Martin, and Raul Bermejo. Assessment of crack-related problems in layered ceramics using the finite fracture mechanics and coupled stress-energy criterion. *Procedia Structural Integrity*, 2:2014–2021, 2016.

- [60] James T Richardson, Robert Scates, and Martyn V Twigg. X-ray diffraction study of nickel oxide reduction by hydrogen. *Applied Catalysis A: General*, 246:137–150, 2003.
- [61] O Yamamoto. Perovskite-type oxides as oxygen electrodes for high temperature oxide fuel cells. *Solid State Ionics*, 22(2-3):241–246, 1987.
- [62] Harlan U. Anderson. Review of p-type doped perovskite materials for SOFC and other applications. *Solid State Ionics*, 52(1-3):33–41, 1992.
- [63] Tatsumi Ishihara. *Perovskite Oxide for Solid Oxide Fuel Cells*. Springer, 2009.
- [64] Y.-H. Huang, G Liang, M Croft, M Lehtimäki, M Karppinen, and J B Goodenough. Double-perovskite anode materials  $\text{Sr}_2\text{MMo}_6$  ( $\text{M} = \text{Co}, \text{Ni}$ ) for solid oxide fuel cells. *Chemistry of Materials*, 21(11):2319–2326, 2009.
- [65] Yun-Hui Huang, Ronald I. Dass, Jonathan C. Denyszyn, and John B. Goodenough. Synthesis and Characterization of  $\text{Sr}_{2}\text{MgMoO}_{6-\delta}$ . *Journal of The Electrochemical Society*, 153(7):A1266, 2006.
- [66] Carlos Bernuy-Lopez, Mathieu Allix, Craig A. Bridges, John B. Claridge, and Matthew J. Rosseinsky.  $\text{Sr}_2\text{MgMoO}_6-\delta$ : Structure, phase stability, and cation site order control of reduction. *Chemistry of Materials*, 19(5):1035–1043, 2007.
- [67] Ke-Ji Pan, A. Mohammed Hussain, and Eric D. Wachsman. High Performance Low-Temperature Solid Oxide Fuel Cells with  $\text{SrFe}_{0.2}\text{Co}_{0.4}\text{Mo}_{0.4}\text{O}_{3-\delta}$  based Ceramic Anodes.
- [68] A. Mohammed Hussain, Yi-Lin Huang, Ke-Ji Pan, Ian Robinson, and Eric D. Wachsman. A Redox-Robust Ceramic Anode for Low-Temperature SOFC.
- [69] A. Mohammed Hussain, Ian Robinson, Yi-Lin Huang, Ke-Ji Pan, and Eric D. Wachsman. Stable Molybdate-Based Ceramic Anodes for Low-Temperature Solid Oxide Fuel Cells.
- [70] Clemens Ritter, Javier Blasco, Jose-Maria De Teresa, David Serrate, Luis Morellon, Joaquin Garcia, and Manuel Ricardo Ibarra. Structural and magnetic details of 3d-element doped  $\text{Sr}_2\text{Fe}_{0.75}\text{T}_{0.25}\text{MoO}_6$ . *Solid State Sciences*, 6(5):419–431, 2004.
- [71] D. S. Tsvetkov, I. L. Ivanov, D. A. Malyshkin, A. S. Steparuk, and A. Yu. Zuev. The defect structure and chemical lattice strain of the double perovskites  $\text{Sr}_2\text{BMo}_6-\delta$  ( $\text{B} = \text{Mg}, \text{Fe}$ ). *Dalton Transactions*, 45(32):12906–12913, 2016.
- [72] B. Levasseur and S. Kaliaguine. Effects of iron and cerium in  $\text{La}_{1-y}\text{Ce}_{y}\text{Co}_{1-x}\text{Fe}_x\text{O}_3$  perovskites as catalysts for VOC oxidation. *Applied Catalysis B: Environmental*, 88(3-4):305–314, 2009.

- [73] Qiang Liu, Daniel E. Bugaris, Guoliang Xiao, Maxwell Chmara, Shuguo Ma, Hans Conrad Zur Loyer, Michael D. Amiridis, and Fanglin Chen. Sr<sub>2</sub>Fe1.5Mo0.5O<sub>6</sub>-delta as a regenerative anode for solid oxide fuel cells. *Journal of Power Sources*, 196(22):9148–9153, 2011.
- [74] S. Vasala, M. Lehtimäki, Y. H. Huang, H. Yamauchi, J. B. Goodenough, and M. Karppinen. Degree of order and redox balance in B-site ordered double-perovskite oxides, Sr<sub>2</sub>MMoO<sub>6</sub>-δ(M=Mg, Mn, Fe, Co, Ni, Zn). *Journal of Solid State Chemistry*, 183(5):1007–1012, 2010.
- [75] D. Marrero-López, J. Peña-Martínez, J. C. Ruiz-Morales, M. Gabás, P. Núñez, M. A G Aranda, and J. R. Ramos-Barrado. Redox behaviour, chemical compatibility and electrochemical performance of Sr<sub>2</sub>MgMoO<sub>6</sub> - δ as SOFC anode. *Solid State Ionics*, 180(40):1672–1682, 2010.
- [76] R Kircheisen and J. Töpfer. Nonstoichiometry, point defects and magnetic properties in Sr<sub>2</sub>FeMoO 6-δ double perovskites. *Journal of Solid State Chemistry*, 185:76–81, 2012.
- [77] Keith L. Duncan and Eric D. Wachsman. General model for the functional dependence of defect concentration on oxygen potential in mixed conducting oxides. *Ionics*, 13(3):127–140, 2007.
- [78] A. Holt, T. Norby, and R. Glenne. Defects And Transport In SrFe(1-x)CO<sub>x</sub>O<sub>3.5</sub>. *Ionics*, 5(5-6):434–443, 1999.
- [79] M. Radovic and E. Lara-Curzio. Mechanical properties of tape cast nickel-based anode materials for solid oxide fuel cells before and after reduction in hydrogen. *Acta Materialia*, 52(20):5747–5756, 2004.
- [80] Miladin Radovic and Edgar Lara-curzio. Elastic Properties of Nickel-Based Anodes for Solid Oxide Fuel Cells as a Function of the Fraction of Reduced NiO. *J. Am. Ceram. Soc.*, 87(12):2242–2247, 2004.
- [81] J. Laurencin, G. Delette, B. Morel, F. Lefebvre-Joud, and M. Dupeux. Solid Oxide Fuel Cells damage mechanisms due to Ni-YSZ re-oxidation: Case of the Anode Supported Cell. *Journal of Power Sources*, 192(2):344–352, 2009.
- [82] D. Sarantaris and A. Atkinson. Redox cycling of Ni-based solid oxide fuel cell anodes: A review. *Fuel Cells*, 7(3):246–258, 2007.
- [83] Qin Zhang, Tao Wei, and Yun-hui Huang. Electrochemical performance of double-perovskite Ba 2 MMoO 6 ( M = Fe , Co , Mn , Ni ) anode materials for solid oxide fuel cells. *Journal of Power Sources*, 198:59–65, 2012.
- [84] F. Boroomand, E. Wessel, H. Bausinger, and K. Hilpert. Correlation between defect chemistry and expansion during reduction of doped LaCrO<sub>3</sub> interconnects for SOFCs. *Solid State Ionics*, 129(1):251–258, 2000.

- [85] S R Bishop, K L Duncan, and E D Wachsman. Surface and bulk oxygen non-stoichiometry and bulk chemical expansion in gadolinium-doped cerium oxide. *Acta Materialia*, 57(12):3596–3605, 2009.
- [86] David J. Green. *An Introduction to the Mechanical Properties of Ceramics*. Cambridge University Press, 1998.
- [87] Takuto Kushi, Kazuhisa Sato, Atsushi Unemoto, Shinichi Hashimoto, Koji Amezawa, and Tatsuya Kawada. Elastic modulus and internal friction of SOFC electrolytes at high temperatures under controlled atmospheres. *Journal of Power Sources*, 196(19):7989–7993, 2011.
- [88] Koji Amezawa, Takuto Kushi, Kazuhisa Sato, Atsushi Unemoto, Shin Ichi Hashimoto, and Tatsuya Kawada. Elastic moduli of Ce<sub>0.9</sub>Gd<sub>0.1</sub>O<sub>2-??</sub> at high temperatures under controlled atmospheres. *Solid State Ionics*, 198(1):32–38, 2011.
- [89] Patrick Stanley, A Mohammed Hussain, Yi-lin Huang, J Evans Gritton, Jonathan A O Neill, and Eric D Wachsman. Defect chemistry and oxygen non-stoichiometry for solid-oxide fuel cells. pages 1–19.
- [90] Robert Danzer, Tanja Lube, Peter Supancic, and Rajiv Damani. Fracture of ceramics. *Advanced Engineering Materials*, 10(4):275–298, 2008.
- [91] David Waldbillig, Anthony Wood, and Douglas G. Ivey. Thermal analysis of the cyclic reduction and oxidation behaviour of SOFC anodes. *Solid State Ionics*, 176(9-10):847–859, 2005.
- [92] Y. Wang, M. E. Walter, K. Sabolsky, and M. M. Seabaugh. Effects of powder sizes and reduction parameters on the strength of Ni-YSZ anodes. *Solid State Ionics*, 177(17-18):1517–1527, 2006.